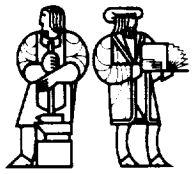

Plasma Fusion Center
Massachusetts Institute of Technology
Cambridge, Massachusetts 02139
Telephone: 617/253-8100

TO: Ms. Gloria R. Blanchard
Grants Officer, Space Sciences Directorate
Procurement Office, NASA/GSFC

FROM: Prof. Min-Chang Lee
(617)-253-5956

DATE: February 1, 1993

SUBJ.: Progress Report on the Sponsored Research in
"Radio Stimualation and Diagnostics of Space Plasmas"
(under the NASA Grant No. NAG 5-1055)

Please find enclosed three copies of our progress report on the sponsored research in "Radio Stimulation and Diagnostics of Space Plasmas" under the NASA grant number NAG 5-1055. The main research accomplished is the investigation of small scale topside ionospheric plasma structures which are associated with obliquely propagating plasma modes. These small scale plasma modes are basically ion acoustic modes having large radar cross sections. They were first observed at Millstone Hill, Massachusetts with the 440 MHz incoherent scatter radar. They were later confirmed in our experiments at Tromso, Norway. The details of this research can be found in K.M. Groves' Ph.D. dissertation accomplished recently at MIT under my supervision.

A copy of this progress report has been sent separately to Dr. Robert F. Benson, Contract Monitor of this NASA grant/contract. Thank you very much for your kind attention.

MCL/al
c.c. Dr. R.F. Benson

Progress Report on the Sponsored Research in "Radio Stimulation and Diagnostics of Space Plasmas" (under the NASA Grant No. NAG 5-1055)

1. Introduction:

We have investigated the small-scale topside ionospheric plasma structures first observed at Millstone Hill, Massachusetts with the 440 MHz incoherent scatter radar [Foster et al., 1988; Groves et al., 1992]. These small-scale obliquely propagating plasma modes occurring in the vicinity of the mid-latitude ionospheric trough, have large radar cross-sections and narrow spectral widths. They have, until recently, been dismissed solely as hard target contamination of the incoherent scatter radar.

The geophysical conditions associated with the ionospheric trough, such as the field-aligned current activity and steep plasma density gradients, suggest that these recently discovered small-scale topside ionospheric plasmas may also appear in the auroral and polar ionosphere. In fact, this speculation has been corroborated by the preliminary experiments and data analyses at Tromso, Norway and Sondrestromfjord, Greenland which were carried out by Prof. Min-Chang Lee's previous graduate student, Dr. Keith M. Groves for his thesis research. The primary research results are highlighted and commented in Section 2. Described in Section 3 are the experiments conducted at Arecibo, Puerto Rico in the past summer for simulating the geophysical conditions of generating these topside ionospheric plasma structures. Recommendation for the future research is finally given. Attached as the appendix of this report are several chapters of Dr. Keith M. Groves's Ph.D. Dissertation, which present the detailed results of research in the concerned topside ionospheric clutter.

2. Highlights of Research Results:

(1) Causes of the Enhanced Radar Backscatter (ERB) Phenomenon

Multiple-diagnostic experiments have established association of enhanced radar backscatter (ERB) with intense magnetic field-aligned currents in the ionosphere. The source mechanism is believed to be the intense Langmuir waves [electron plasma oscillations] excited by the large suprathermal electron population associated with field-aligned currents and auroral arcs. Earlier current-driven theories require current densities much greater than have been measured on satellites. A new mechanism has been investigated which can enhance radar backscatter in conjunction with the current driven processes, thereby reducing the threshold amplitudes of the current densities they require.

The scenario of the proposed mechanism is as follows: energetic electrons associated with the intense current filaments in the ionosphere excite a suprathermal spectrum of Langmuir waves as they stream through the background plasma. Subsequently the Langmuir waves can become non- linearly coupled via the ponderomotive force to induce low frequency density perturbations driving ion acoustic waves (IAW) in the ionospheric plasmas.

This mechanism predicts important observed effects such as the simultaneous enhancement of upshifted and downshifted spectral peaks, increasing levels of enhancement for increasing wavelengths, and the enhancement of ion acoustic wave backscatter modes at large aspect angles from the geomagnetic field. Up to two orders of magnitude of radar cross section enhancement are predicted from this mechanism for radar frequencies corresponding to the 440 Mhz Millstone Hill incoherent scatter radar. The theory also predicts enhancement of wave modes with large aspect angles relative to the magnetic field, increasing enhancements for longer wavelengths, and enhancement in both upward and downward directions along the field line.

(2) Occurrence of the ERB Phenomenon

The ERB phenomenon has been observed in the trough region and in the auroral region where intense ionospheric current activity can occur. Since the source mechanism

is believed to be triggered by geomagnetic field-aligned currents in the topside ionosphere, the enhanced radar backscatter effect could occur wherever these currents could occur in combination with required plasma densities and temperatures. This is known to occur in the ionospheric trough and auroral regions when charged particle precipitation from the solar wind originates field-aligned currents during higher geomagnetic activity. The sharp electron density gradients in the trough region can become source regions generating the IAW plasma modes. Once the IAW waves are produced, they propagate obliquely across the Earth's magnetic field, hence they can be detected by radars at any aspect angle with respect to the field, (as opposed to only in the field-aligned direction). The effect may also occur at higher altitudes over the mid-latitudes, [although with probably smaller backscatter levels] and in the equatorial region when the right conditions are present.

(3) Altitudes of the ERB Phenomenon

ERB has been seen at Millstone Hill (mid-latitude) in the topside ionosphere ranging from 300 to 1000 km altitude, while at Tromso, Norway and Greenland (high-latitude) ERB was seen at lower altitudes. This can be explained, under the proposed new source mechanism, from several facts: A. At mid-latitudes, field-aligned currents only pass through higher altitudes, (whereas, at higher latitudes the field lines associated with these currents are near vertical and the currents reach lower altitudes). B. Ion acoustic waves associated with large radar cross sections can appear in a large range of altitudes, when field-aligned currents and the right temperatures and densities are present.

(4) Strength of the ERB Returns

20 dB backscatter enhancements were seen at the Millstone and similar observations were noted at EISCAT. According to the proposed mechanism, the radar cross section of the induced ion acoustic modes is a function of the radar frequency, and of the scale length and intensity of the source Langmuir wave. Up to two orders of magnitude of backscatter radar cross section enhancement are predicted from this mechanism for radar frequencies

corresponding to the 440 Mhz Millstone Hill incoherent scatter radar. Up to 3 orders of magnitude enhancement are possible corresponding to a radar frequency of 224 MHz under the same ionospheric conditions.

(5) Range of Altitudes of the ERB Returns

Range extent is a function of location, look direction, and field alignment. At low latitudes the field-aligned currents are many thousands of km away, (at high altitude corresponding to the magnetic field shell that intersects the auroral zone), and if observable at all an IAW source region would have minimal range extent. At mid-latitudes observation of an IAW source region associated with field-aligned currents (looking north at lower elevation) is within 45^o of field-aligned, yielding narrow range extents of the order of a few hundred meters. At higher latitudes observation of IAW source regions is within 14^o of field-aligned (near vertical) and range extents of 600-1000 km are possible.

(6) Occurrence Frequency of the ERB Phenomenon

Extended range ERB events may occur infrequently at mid-latitudes. The estimate is 10-15 days/year based on Kp at time of the one event recorded at Millstone Hill. By contrast, the extended range ERB events are extraordinary at auroral latitudes. The EISCAT events have been seen in the presence of sharp fluctuations in the local magnetic field (500 nT N-S), the auroral particle precipitation evidenced by airglow, the elevated electron temperatures (T_e up to 8000^o K), and the electron-to-ion temperature ratios greater than two, though not extremely high (typically, $2 < T_e/T_i < 3$). However, some EISCAT cases were more closely correlated with elevated ion temperatures, strong perpendicular electric fields and little, if any, auroral precipitation. The ERB occurrence caused by the precipitating particles would be determined by the occurrence of the precipitation-induced field- aligned currents. The EISCAT radar (Tromso, Norway) has observed ERB when the magnetic index, $Kp > 5$, a level of disturbance occurring about 5 % of the time during solar maximum.

(7) Doppler Effect of the ERB Phenomenon

Apparent velocities, typically 1-2 km/sec ion acoustic speed at 300 km have been seen. The frequency shift of the anomalous spectra increases smoothly with altitude, corresponding to the increase in the ion acoustic speed with height. The VHF event showed frequency shift to change from upshifted to downshifted over 1 minute; another event had consistent downshift for approximately 4 minutes. In the UHF measurements the asymmetry seems to fluctuate more rapidly in both time and space between downshifted and upshifted frequencies [see appendix].

These observations show that although ERB resulting from IAW from a Langmuir wave source region remains relatively stationary while it persists, it exhibits a significant doppler frequency as if it were actually moving. The doppler frequency of ERB is determined by $2kC_s$, where k = $2\pi/\lambda_{radar}$, (λ_{radar} = radar signal wavelength), and C_s = ion acoustic speed, (typically 1 - 2 km/sec in the ionospheric F- region [250-450 km altitude]). The doppler frequency shift of the observed ERB increases smoothly with altitude, corresponding to the increase in the ion acoustic speed with altitude. The background plasma convects at a velocity (ExB - cross product of electric and magnetic field vectors) which can be clearly distinguished from the doppler velocity of the ERB from the ion acoustic waves.

(8) Persistency of the ERB

The Millstone's extended range echo was observed to disappear 6 minutes later when the radar next scanned the same region. Large fluxes of low-energy electrons (field-aligned currents) are seen to persist for tens of minutes. Extended range events at EISCAT were seen to persist for about 30 sec. Nevertheless, some EISCAT events have lasted up to 50 seconds, continuously; shorter sporadic bursts distributed over a period of a few tens of minutes are seen more frequently. It is interesting to note that the VHF events persist much longer than the UHF observations. One event lasted up to 4 minutes, another

occurred sporadically for more than 1 hour. The VHF-observed ERB events are expected to persist much longer than the UHF events due to the fact that the shorter-scale ion acoustic waves observed by UHF have faster damping rates and require larger currents for their generation. The field-aligned current can persist for a few minutes to tens of minutes (1 hour). A current filament could make an ERB return appear to dance about, but is not likely to give the impression of a smoothly moving target.

(9) Distinction Between ERB Phenomenon and Space Object Signatures

At zenith a space object's doppler velocity is nearly zero, and is much less than the topside clutter's apparent velocity. The ERB phenomenon can be statistically separated from the probable occurrence of returns form space objects/debris over 48 hours. The ERB phenomenon can have radar returns greatly extended in range because the driving source, viz., the field-aligned electric current extend in range along the magnetic field direction. The frequency shift of the anomalous spectra of the ERB phenomenon increases smoothly with altitude, corresponding to the increase in the ion acoustic speed with height.

Our proposed theory [Groves et al., 1992] predicts that the ERB will exhibit a wavelength dependance on its radar cross section, [see (4) above], which would allow a multiple-frequency measurement to distinguish ERB from space objects. Also: (A). ERB will exhibit a doppler velocity as in (7), above, but 1) the ERB will remain essentially stationary, 2) the doppler velocity depends on radar frequency, and 3) the ERB doppler velocity can be large near zenith where a space object's doppler velocity is nearly zero. (B). ERB returns will be associated with the locations of intense geomagnetic field-aligned currents, which occur along the shell of the Earth's geomagnetic field that penetrates the ionosphere over the auroral and ionospheric trough regions (in the high latitudes), and may be observed at any aspect angle with respect to the field. Space object returns may be seen at any altitude or direction. The ERB occurrence will be highest in the

topside ionosphere above the auroral zone and trough regions between 300 and 1000 km altitude. (C). The ERB occurrence may be expected during higher magnetic activity such as $K_p > 5$, which occurs about 5 % of the time during solar maximum. (D). The ERB may exhibit greatly elongated range extent (600-1000 km), when observed from a high latitude station in a direction that is within 14_o of geomagnetic field-aligned.

3. Simulation Experiments and Future Research:

As mentioned before, experiments were conducted at Arecibo, Puerto Rico for simulating the geophysical conditions of generating the concerned topside ionospheric clutter. The experimental setup is delineated in Figure 1. Briefly speaking, we believe that particle precipitation can be a source mechanism producing these small scale plasma structures. The controlled study of ionospheric plasma structures induced by particle precipitation can be performed with the radio facilities at Arecibo as elucidated below.

Arecibo, Puerto Rico is located near the footprint of the magnetic flux tube at L = 1.47. Man-made particle precipitation from the radiation belts can be triggered by a guided VLF wave injected from a nearby Naval transmitter. The waveguides are created by the Arecibo heating facility which transmits high-power HF waves vertically into the ionosphere. The scenario of the VLF-triggered particle precipitation is as follows. The HF heater is operated in CW mode for ten minutes or so to create large-scale waveguides, guiding the transmitted VLF wave to propagate into the magnetosphere in the form of whistler waves. According to Prof. Lee's graduate student, Karen Koh's theoretical analyses, the injected VLF wave at the frequency of 28.5 kHz can effectively interact with energetic particles in the radiation belts at L = 1.47 and lead to particle precipitation.

Shown in Figure 2 is the suspected event of VLF wave-triggered particle precipitation at Arecibo. Intense radar echoes were recorded from the lower ionosphere at altitudes around 90 km or so. Displayed in Figure 3 are the radar measurements of Langmuir waves (plasma lines) and ion acoustic waves (ion lines) in the HF heated ionospheric region.

Particle precipitation may also be indicated from the asymmetry of ion lines and the frequency-upshifted plasma lines due to the nonlinear scattering of Langmuir waves off the precipitating particle-induced lower hybrid waves. Another graduate student, Yildiz Dalkir is currently undertaking further analyses of these ionospheric plasma processes for his graduate thesis research.

We note that another potential source of structuring the topside ionospheric plasmas are the intense whistler waves which are produced concomitantly when the precipitating particles are reflected in the ionosphere from the mirror geomagnetic field at high latitudes. These whistler waves may also be generated by lightning storms. The possible generation of ion acoustic waves by whistler waves should be investigated.

4. References:

Foster, J.C., C. del Pozo, K. Groves, and J.-P. St. Maurice, Radar observations of the onset of current driven instabilities in the topside ionosphere, *Geophys. Res. Lett., 15*, 160-163, 1988.

Groves, K.M., M.C. Lee, and J.C. Foster, in "Physics of Space Plasmas" (1991), SPI Conference Proceedings and Reprint Series, No. 11, T. Chang, G.B. Crew, and J.R. Jasperse, eds. (Scientific Publications, Cambridge, MA), 377-392, 1992.

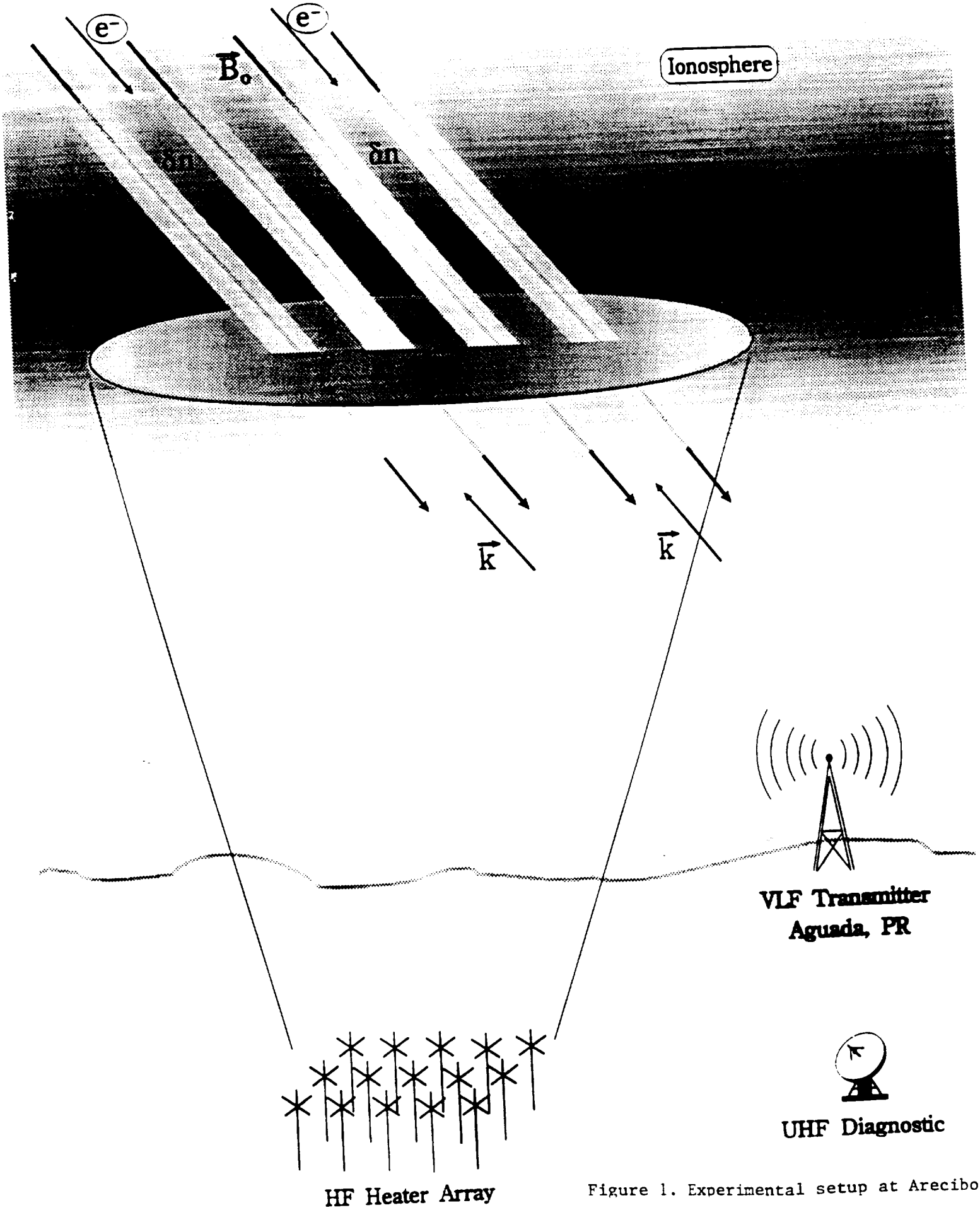

Figure 1. Experimental setup at Arecibo

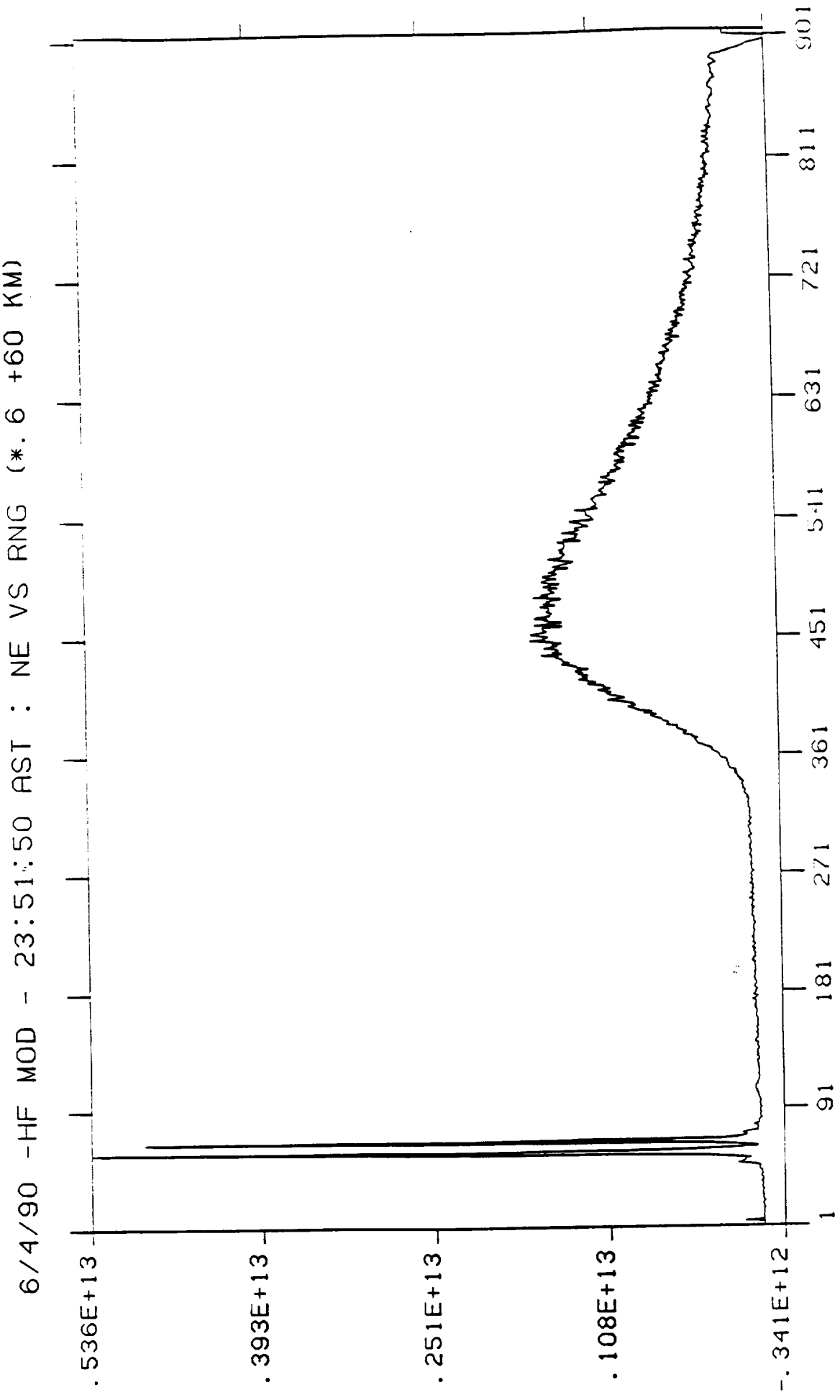

Figure 2. A 430 MHz radar power profile of the ionosphere recorded at the Arecibo Observatory during experiments on June 4, 1990 (Lee et al., 199).

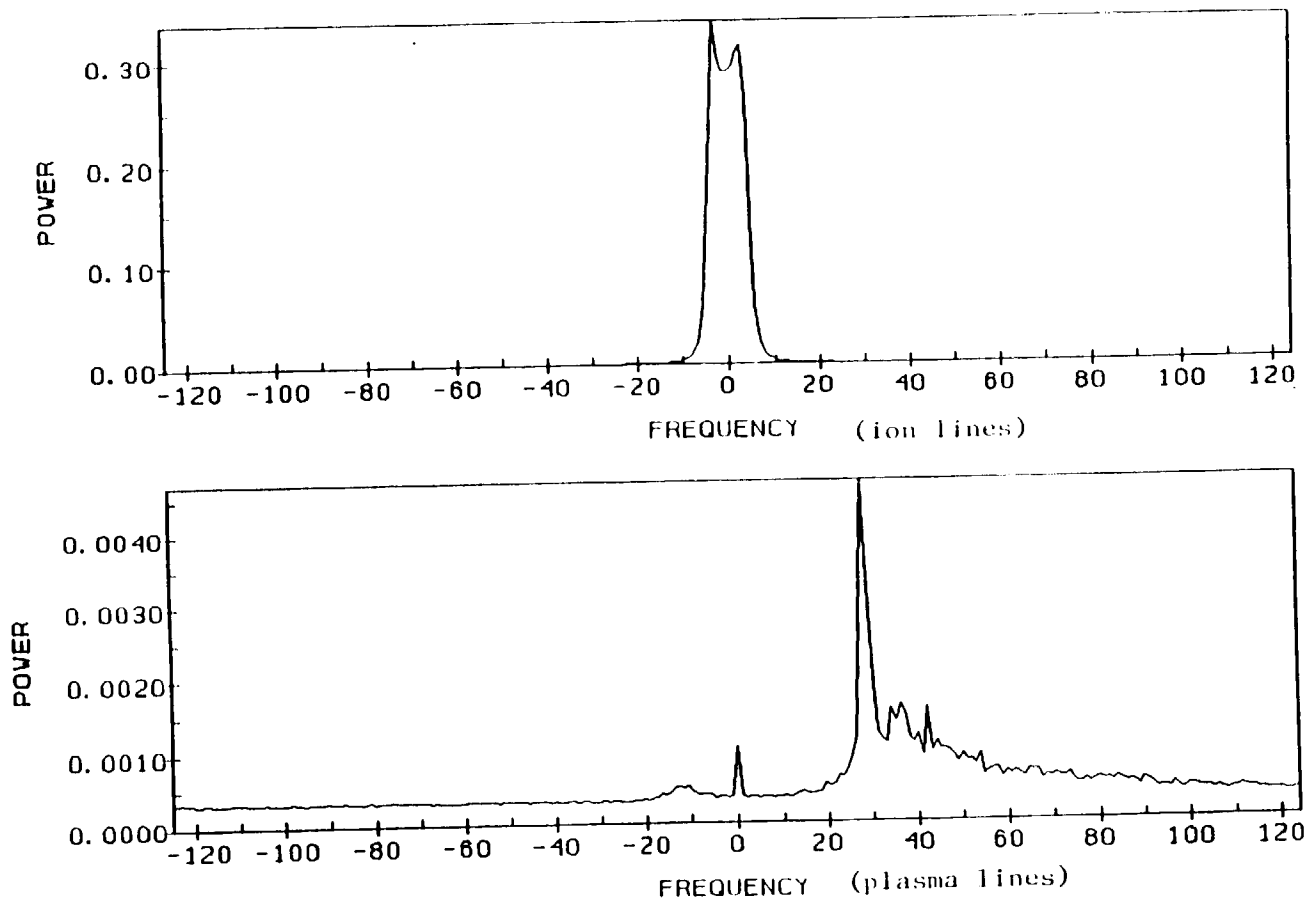

TI=2115181 DA=160791 AZ= 393.0 ZA= 3.5

Figure 3. Radar measurements of plasma lines and ion lines in the heated ionospheric region.

Appendix

Chapter 5

Observations of Enhanced Radar Backscatter (ERB) from Millstone Hill

Intense ($\simeq$ 20 dB) enhancements of the incoherent radar backscatter spectrum from the topside ionosphere have been observed with the Millstone Hill UHF radar. Enhancements occurring at the local ion acoustic frequency causing large asymmetries in the measured ion line may be produced by current-driven instabilities [*Foster et al.*, 1988] (henceforth, FOS88). These enhancements pose a practical problem for space surveillance systems because their cross section and spectral width are characteristic of satellites.

Conversely, their hard target signature complicates the study of naturally occurring ERB events; it is nearly impossible to distinguish them from satellites based on a single measurement. Statistical comparisons of observed coherent echo distributions with predictions from a satellite catalog have been used to broadly identify periods of ERB activity. A series of experiments using multiple diagnostics, including satellite instruments, for simultaneous observations have established the association of ERB

with large fluxes of soft suprathermal electrons carrying field-aligned currents. Zenith data are also presented which show the asymmetric growth of ion acoustic waves directly above Millstone Hill. Zenith measurements filter out satellite contamination because the geometry constrains the Doppler shift from orbiting bodies to velocities significantly less than the ion sound speed in the F region.

Details of these results are presented in this chapter. First, however, a brief description of the normal incoherent scatter spectrum is reviewed, followed by a description of the characteristics of the ERB spectra.

5.1 Incoherent (Thomson) Scatter Process

The radar technique for studying the earth's upper atmosphere typically employs a (HF, VHF or UHF) radar to transmit a powerful pulse of electromagnetic radiation into the atmosphere. Following transmission, the radar is used to receive the radiation scattered by the atmosphere back to the antenna. If the details of the scattering process are understood, meaningful information about the medium can be extracted through the appropriate processing of the weak received signal. For the partially ionized upper atmosphere above about 60 km altitude, the electromagnetic waves are scattered by electrons in a process known as *incoherent* or *Thomson* scatter, named after J. J. Thomson who first showed that individual electrons can scatter electromagnetic radiation [1906].

5.1.1 Relationship Between Density Fluctuations and Scattering Properties

The frequency spectrum of the high frequency radiation scattered by the ionosphere is directly related to the power spectrum of the electron density fluctuations in the

plasma. Mathematically the cross section of the plasma as a function of radar carrier offset frequency, ω, may be expressed as

$$\sigma_\omega = \sigma_e V \langle |n(\mathbf{k}, \omega)|^2 \rangle \tag{5.1}$$

Here, $\sigma_e \approx 10^{-28} m^2$ is the scattering cross section of a single electron, V is the scattering volume, $\langle\ \rangle$ indicate a time average; k and ω are the difference of the incident and scattered wave vectors and frequencies, respectively, *viz.* $\mathbf{k} = \mathbf{k}_i - \mathbf{k}_s$ and $\omega = \omega_i - \omega_s$. For the usual backscatter radar geometry, $\mathbf{k} = 2\mathbf{k}_i$; thus, the incident radar wavelength, $2\pi/|\mathbf{k}_i|$, determines the scale size of density fluctuations sampled. Here, $n(\mathbf{k}, \omega)$ is the space–time Fourier transform of the usual number density in the plasma, $n(\mathbf{r}, t)$, defined by

$$n(\mathbf{k}, \omega) = \frac{1}{VT} \int_V d\mathbf{r} \int_{-T/2}^{T/2} dt\ n(\mathbf{r}, t) \exp[i\mathbf{k} \cdot \mathbf{r} - i\omega t] \tag{5.2}$$

T in this equation represents a time greater than the correlation time of the plasma medium. The total cross section of the plasma can be obtained by integrating (5.1) over ω,

$$\sigma_{tot} = \int_{-\infty}^{\infty} \sigma_\omega\ d\omega \tag{5.3}$$

Spectrum of Density Fluctuations

The key to determining the characteristics of the received scattered wave, then, lies in calculating the power spectrum of density fluctuations in the space plasma.

When only the random thermal motions of the scattering particles are considered, the spectrum exhibits a broad peak centered on the carrier frequency and a characteristic width of the electron thermal velocity, $\Delta\omega \approx k v_{te}$ [*Fejer*, 1960]. The total cross section as determined by (5.3) is found to be simply $N\sigma_e$, where N represents the total number of electrons in the scattering volume. This result has a straightforward physical interpretation as follows.

The electrons are assumed to undergo random thermal motions, implying that each electron will scatter signals of random phase relative to the other electrons. At the radar receiver the signal powers rather than the signal voltages will add, and the resulting cross section will be equal to the sum of the individual contributions of each electron, $N\sigma_e$. The random phase of the scattered signals suggests the use of the name *incoherent scatter* to describe this process.

However, as more detailed calculations show, the presence of ions in the plasma does introduce a degree of coherence between the electrons' motions (*e.g.*, *Hagfors*, 1961; *Salpeter*, 1960, 1961; *Dougherty and Farley*, 1960; and others). The influence of the ions is found to be important when the incident radar wavelength is much larger than the so-called *Debye length* in the plasma, given by

$$\lambda_D = \left(\frac{\epsilon_o K T_e}{ne^2}\right)^{1/2} = \left(\frac{v_{te}}{\omega_p}\right) \tag{5.4}$$

where ϵ_o is the permittivity of free space, K is Boltzmann's constant, and T_e, n, e, v_{te}, and ω_p are the electron temperature, density, charge, thermal velocity and plasma frequency, respectively.

The Debye length is measure of the distance over which the plasma can shield out electric fields: in the ionospheric F region, $\lambda_d \approx .003$ meters. For distances greater than this length the plasma dynamics are characterized by collective processes rather than the random thermal interactions of individual electrons. The resulting scattering can best be thought of as arising from density fluctuations associated with electrostatic oscillations in the plasma[1]. The idealized power spectrum of density fluctuations under these conditions is shown in Figure 5-1.

[1]The term *incoherent* is not strictly accurate in this case and an alternative name, *Thomson scatter*, has also been applied to this phenomenon.

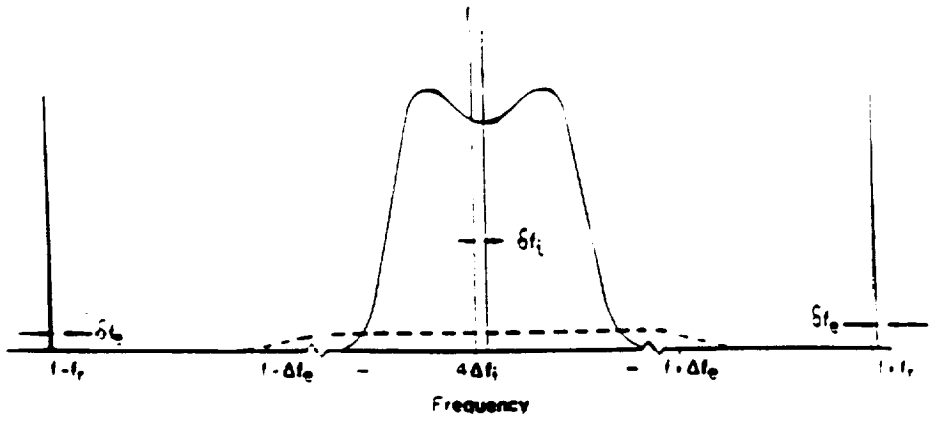

Idealized Incoherent Scatter Spectrum

Figure 5-1: Incoherent scatter power spectrum when $\lambda \gg \lambda_d$. [after *Rishbeth*, 1989]

5.1.2 The Incoherent Scatter Radar Spectrum

The power spectrum in Figure 5-1 consists of two components. The double–humped central spectrum results from density fluctuations associated with ion waves and is correspondingly known as the *ion line*. The sharp peaks flanking the ion line are caused by high frequency electron density fluctuations called plasma waves; this component is therefore known as the *plasma line*.

The Ion Line

The ion waves that give rise to the ion line in the incoherent scatter spectrum are longitudinal oscillations with a phase velocity given by the "sound" speed in the plasma. The dispersion relation for these ion acoustic waves is given here.

$$\frac{\omega}{k} = \left(\frac{KT_e + KT_i}{M_i}\right)^{1/2} \equiv C_s \tag{5.5}$$

where M_i is the ion mass and C_s is defined as the ion sound speed in the plasma, typically 1–2 km/sec in the ionospheric F region. While these waves are ion oscillations,

the electrons follow the motion because of their electrostatic attraction to the massive ions. The two peaks in the ion line power spectrum may be thought of as reflections from ion acoustic waves travelling towards (upshifted peak) and away (downshifted peak) from the radar. The peaks are broadened due to ion thermal motions. Analysis of the shape and magnitude of the spectrum yields several important ionospheric parameters [see, *e.g.*, *Evans*, 1969].

The spectral width corresponds to the ion acoustic phase velocity, which from Equation (5.5) depends primarily on the electron temperature and the mass of the dominant ion species. The offset, δf_i, of the entire spectrum relative to the radar center frequency yields the line-of-sight bulk plasma drift. The electron–ion temperature ratio determines the sharpness of the spectrum's peaks. The area under the ion line curve is directly related to the electron density. These parameters are usually derived through a numerical model which adjusts their values to achieve a best fit to the observed power spectrum.

The Plasma Line

The plasma line component of the incoherent scatter spectrum is usually much weaker than the ion line and more difficult to measure. The sharp peaks result from electron oscillations near the plasma frequency. The dispersion relation for these waves in a magnetized plasma is given by,

$$\omega^2 = \omega_p^2 + \frac{3}{2}k^2 v_{te}^2 + \Omega_e^2 \sin^2\theta \tag{5.6}$$

where Ω_e is the electron cyclotron frequency and θ is the angle between the wave and the geomagnetic field. Usually the dominant term in (5.6), the electron plasma frequency, $\omega_p \propto n^{1/2}$, provides a very accurate indicator of the electron density. The intensity of the plasma line is dependent on the electron temperature. The difference in the relative offset frequency between the upshifted and downshifted lines allows a

determination of the bulk electron drift velocity. This velocity can be compared with the bulk velocity estimated from the ion line measurement to calculate the relative drift between the electrons and ions (*i.e.*, current).

In summary, we have presented the characteristics of the normal incoherent scatter power spectrum. The spectral features of the recently observed enhanced radar backscatter, examined in the next section, exhibit significant departures from the normal spectrum.

5.2 Characteristics of Enhanced Radar Backscatter (ERB)

Intense coherent radar returns from the topside of the ionospheric F region have been a regular feature of the Millstone Hill UHF incoherent scatter radar data for many years. Because these returns are characterized by the large radar cross sections and narrow spectral widths which can result from satellite penetration of the 1° radar beam, they have, until recently, been dismissed solely as hard target contamination of the incoherent scatter data. Foster et. al [1987] noted an anomalously high occurrence of intense radar echoes in the vicinity of the mid-latitude ionospheric trough. The unique geophysical conditions associated with the trough, such as field-aligned current activity and steep plasma density gradients, suggest that some of the coherent returns may be caused by enhanced ionospheric plasma density fluctuations, rather than orbiting objects intersecting the radar beam [FOS88].

The generation of such spectra may be attributed to current-driven ionospheric plasma processes [FOS88]. The processes described by Kindel and Kennel [1971] and Rosenbluth and Rostoker [1962], for example, predict the amplification of ion acoustic waves in the presence of intense currents and explain several features of the

observed enhancements, as discussed in Chapter 7. Here we present evidence derived from several sources for the observation of stimulated ion acoustic wave growth with the Millstone Hill UHF radar. These include statistical analyses of large data sets, multi-diagnostic measurements, and the observation of ERB in zenith experiments.

5.2.1 Satellite Contamination and Statistical Analyses of ERB

The task of separating satellite returns from true ionospheric coherent echoes is difficult because the integrated spectral features of both are essentially identical. This is illustrated in Figure 5-2, where the power spectra of the normal incoherent scatter ion line, an intense return from an enhanced ion line, and spherical satellite number 9636 are plotted on the same frequency scale for comparison; each plot is self-normalized. Even on a pulse-to-pulse basis satellite returns may vary by as much as 20 dB due to reflecting surface irregularities and rotation effects [*S. Sridharan*, private communication, 1988]; the size of this variation is comparable to the magnitude of the largest geophysical ERB events. Thus, the similarity between geophysical ERB spectra and satellite spectra makes unambiguous classification of individual ERB events difficult. Several approaches to the resolution of this problem have been employed: the most successful involves the statistical reduction of large data sets, as described below.

The Satellite Catalog

A large number of satellites pass through the Millstone I.S. Radar field of view during any particular experiment; their spectral signatures constitute the primary source of coherent echo contamination in the topside ionosphere. At Millstone Hill we are fortunate to have access to a complete catalog of the known orbiting space objects. An altitude distribution of orbiting objects generated from this catalog is shown in

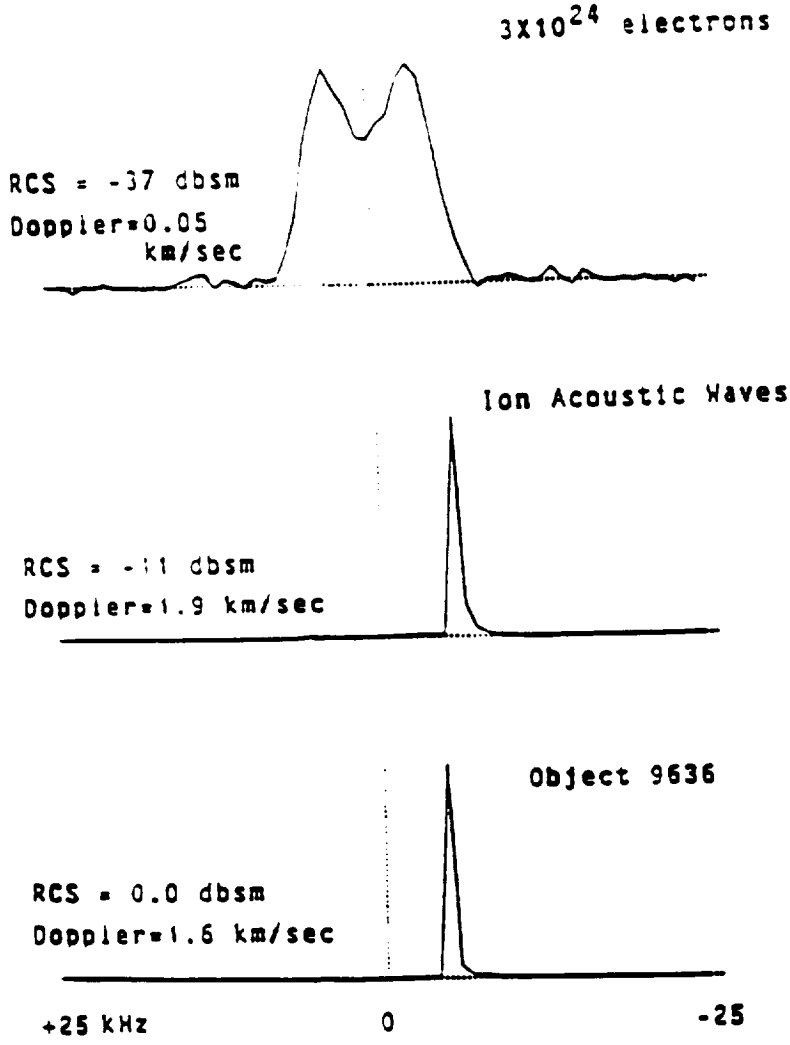

Figure 5-2: UHF Power spectrum of a) Normal incoherent scatter ion line; b) Enhanced ion line; and c) Spherical satellite #9636. The amplitude on each plot is self-normalized.

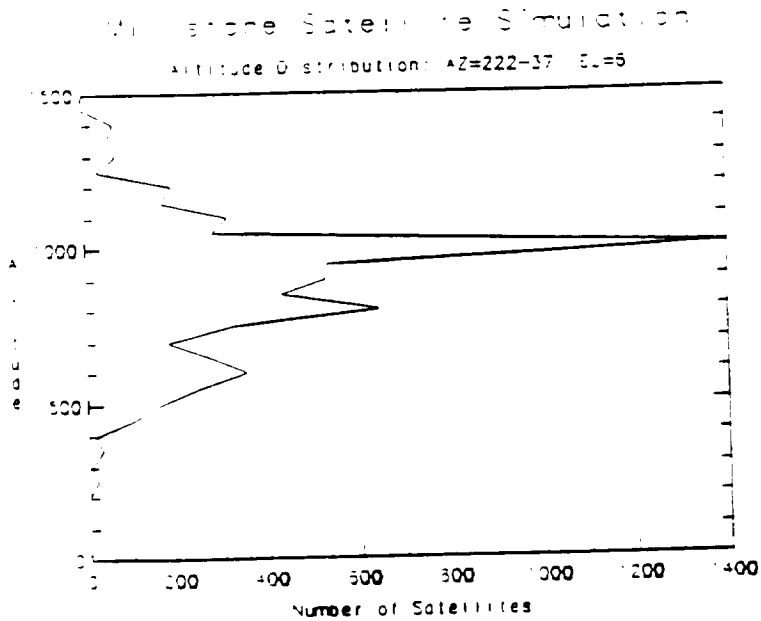

Figure 5-3: Altitude distribution of satellites in the Millstone Hill radar field-of-view for a 6° elevation angle.

Figure 5-3.

The majority of the satellite population exists at altitudes above about 500 km; layers of debris can be identified near 600 km and 800 km, with a well defined maximum near 1000 km. The distribution underscores the problem of removing hard target contamination: The Millstone Radar cannot diagnose the active auroral regions north of 60° latitude at altitudes less than 500 km. Thus we are forced to sample the active region of interest at altitudes where the greatest number of contaminants are located. A number of techniques utilizing the satellite catalog have been employed to distinguish satellite echoes from those of geophysical origin.

Specific Events One way to employ the catalog is to simply check specific records of the radar data containing coherent peaks suspected to be geophysical ERB returns. The time and location of a peak's occurrence can be checked against the catalog to determine if a satellite with the appropriate Doppler velocity was present. In applying this method one must be careful to properly define the uncertainty in the space-time window which must be specified for the coherent echo's location.

A single Millstone data record is typically constructed of power measurements which are integrated for 15–30 seconds, during which time the radar may scan up to five degrees in azimuth. Spatial range smearing due to the radar pulse length adds up to 150 km uncertainty in range. Additional error is introduced by the finite radar beamwidth; the large radar cross section of many satellites requires one to define the "effective beamwidth" as including the sidelobe pattern well beyond the common definition of the half-power width. For the Millstone Hill steerable UHF antenna, this means expanding the traditionally defined 1° beamwidth to some 2°–3°. The largest uncertainties in the azimuth, range, and time of the space-time window specified for a given echo are then, respectively, $\pm$ 5°, 150 km, and 30 seconds, enough time for a satellite to travel some 250 kilometers.

In reality, of course, the radar beam occupies only a small fraction of the total window at a given moment in time; to insure a fair check, however, the entire window must be specified for the satellite catalog to check a particular data record. The result is that the catalog often predicts the penetration of the relatively large space window by several hard targets within the 30 second record interval, even when no evidence of a corresponding coherent peak is seen in the data.

If the catalog predicts that no suitable satellites were present, one can at least be confident that the assumption of the peak's ionospheric origin has not been ruled out. While this use of the satellite catalog is perhaps the most obvious, the technique cannot provide definitive proof that a given radar echo was generated by the ionosphere because the satellite catalog is not 100% reliable.

The catalog is not completely reliable for several reasons. The large number of objects cataloged (over 7000 presently) makes it very difficult to provide frequent element set updates on all objects. The low altitude orbits occupied by the satellites penetrating the Millstone Hill radar beam degrade fairly rapidly, so that catalog

projections of the locations of some objects may be significantly inaccurate. Furthermore, there are numerous classified satellites not included in the catalog used for these studies. Finally, there is a population of uncataloged small orbiting debris.

Statistical Studies The uncertainties involved in applying the satellite catalog to check specific events limit the usefulness of that technique, as noted above. The factors that render the catalog fallible for selected records, however, become unimportant if one applies the catalog in a temporally statistical manner. A calculation of the distribution of low altitude targets ($\tau_{orbit} < 110$ minutes) passing through a defined space window over a period of 24 hours or so, will not depend significantly on the accuracy of a particular satellite's ephemeris data. Assuming they represent a small percentage of the total satellite population and exhibit a similar altitude distribution, classified objects no longer constitute a serious source of error, either. The contamination due to the uncataloged debris must be examined in more detail.

Only about five percent of the over 7000 space objects cataloged are active or working satellites. About 50% of the known objects orbiting the earth consist of fragments resulting from the breakup of artificial satellites. The primary causes of satellite breakups are propulsion related malfunctions and intentional detonation, although collisions are suspected for unexplained breakups as well [*Johnson*, 1985]. It is believed that the uncataloged population of fragments from these breakups may be up to 2.5 times greater than the total cataloged population [*Kessler*, 1985].

Statistical studies, however, will not be modified significantly by the presence of the orbiting debris for two reasons. The first is that the uncataloged population consists of fragments smaller than about 10 centimeters diameter. Objects of this size in the topside of the ionosphere are too small to cause greatly enhanced coherent echoes, particularly for radar wavelengths much greater than the fragment diameter. The second reason is that the distribution of fragments generated by a breakup re-

mains centered in height at the original orbit altitude. Thus the shape of the altitude distribution changes very little: only the number of objects varies.

Doppler Shift Discrimination The catalog has been employed to calculate the passage of satellites through an azimuth window which is left "open" for a sufficient period of time to allow several orbital revolutions, typically 24 hours. In Figure 5-4a a histogram of the number of cataloged objects is plotted as a function of their line-of-sight velocity to the Millstone radar for a low elevation azimuth scan between 342°–27° over a 24 hour period. The spikes located at about ±6 km/sec are due to the large population of satellites in so-called "polar" orbits, high inclination orbits between 800–1000 kilometers altitude. The radar measures a large line-of-sight velocity as it scans to the north and detects these objects as they pass over the polar cap. The velocity measured by the radar is actually determined from the Doppler shift of the scattered signal received by the antenna. For the backscatter geometry employed here, the shift in kHz is given by $\Delta f = 2v/\lambda$, where v is the satellite velocity in km/sec and λ the radar wavelength in meters. A simple conversion for the 68 cm wavelength used by Millstone Hill is $\Delta f \simeq 3v$.

Figure 5-4b shows the distribution of coherent peaks observed at Millstone Hill for an experiment run 13–15 January, 1988 scanning through the same azimuths as the simulation 5-4a. A comparison of the two nearly identical distributions suggests that many, if not all, of the peaks observed during this experiment were caused by satellites penetrating the scanning radar beam. Magnetic conditions during 48 of the 72 hours of data analyzed were very disturbed; Kp values of 7 or higher were registered for a 9 hour period, and remained at or above 6 for 15 consecutive hours during the middle period of the experiment.

The consideration of magnetic activity is important because of its correlation with field-aligned currents. The Kp indices referred to here are global classifiers of the am-

plitudes of magnetic variations derived every three hours based on observations from a number of stations located over a wide range of latitudes. The quasi-logarithmic scale varies from 0 to 9 in 27 increments: the scale is skewed towards the low end of these values in that magnetic fluctuations corresponding to 3 or less occur 90% of the time, whereas fluctuations of Kp=6 or greater represent less than 1% of the total distribution [*Mayaud*, 1980]. Given the sustained periods of very high activity occurring during the experiment of JAN88, we might expect a correspondingly high intensity of field-aligned currents, producing significant numbers of ERB events. Reasons for the apparent lack of observed ERB in this experiment will be discussed shortly.

A second experimental simulation and corresponding observations are presented in Figure 5-5. As in Figure 5-4, the signature of the polar orbiters at ± 6 km/sec is evident in both 5-5a and b. However, in Figure 5-5 an even larger number of peaks were observed between ± 1–2 km/sec, the ion sound speed regime in topside ionospheric plasmas. This remarkable feature has not been observed in velocity distributions constructed from other Millstone Hill radar experiments. Clearly the satellite catalog does not predict the large population of peaks observed at these Doppler velocities. If this data set represents a statistical average, we can feel confident that a portion of the observed ion acoustic peaks were generated by ionospheric processes.

The satellite simulations shown in Figures 5-4a and 5-5a were generated by continuously monitoring all azimuths within a defined window simultaneously, in so-called *open window* simulations. Because the simulated coverage area is large, 12 hours ($t \geq 6\tau_{orbit}$) is a sufficient time to run the open window simulation. Simulating longer periods of time does not affect the shape of the calculated distribution of detected hard targets: it only increases the number of "hits" in the radar beam.

In an actual experiment, of course, the beam scans through the window and monitors only a small fraction of the total azimuth extent at any moment in time. The

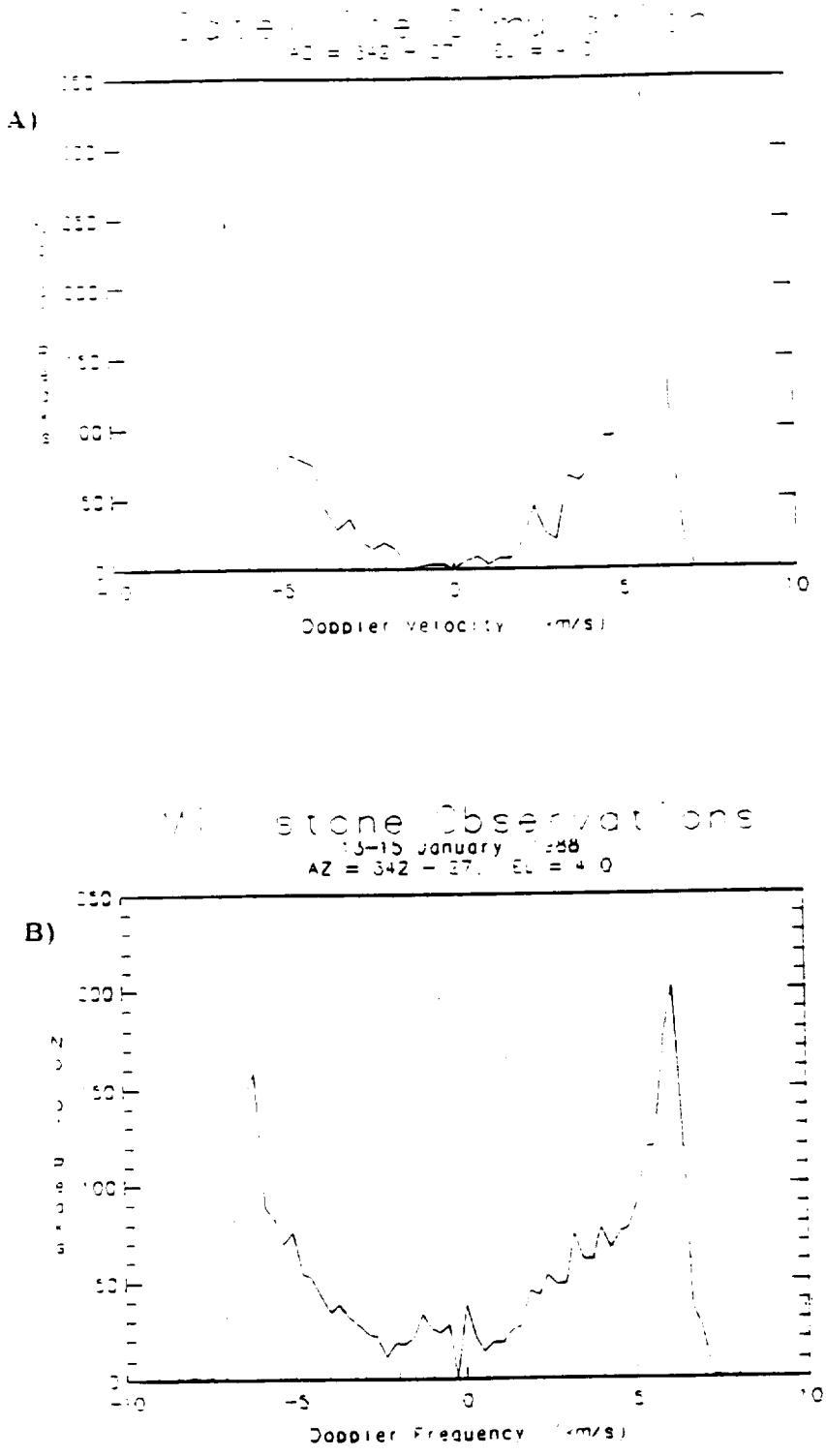

Figure 5-4: Distribution of Doppler velocities for a) satellites penetrating the radar beam between 342°–27° AZ, 4° EL, and b) Actual observations from 13–15 Jan. 1988 for the same pointing angles.

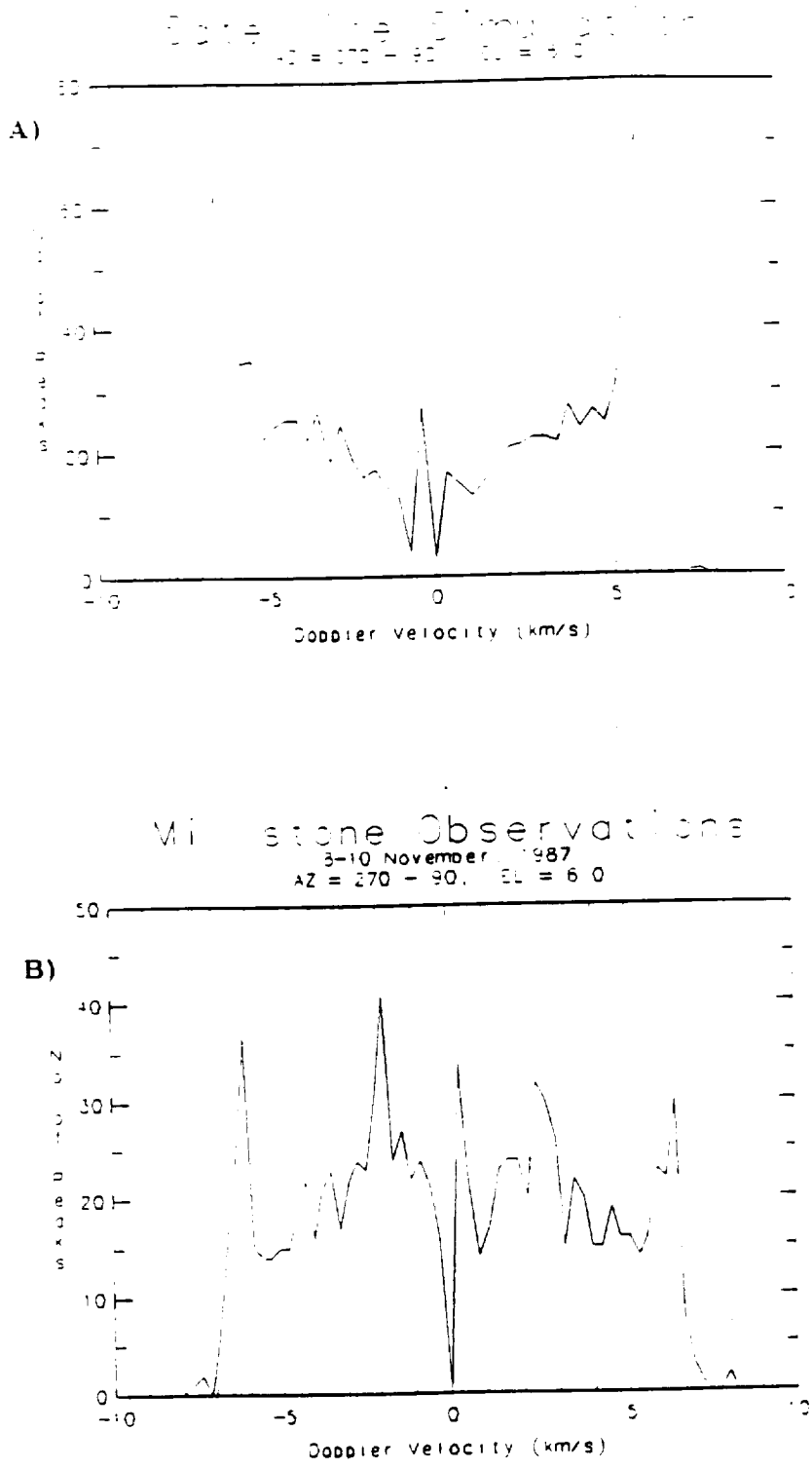

Figure 5-5: Distribution of Doppler velocities for a) satellites penetrating the radar beam between 270°–90° AZ, 6° EL, and b) Actual observations from 8–10 November 1987 for the same pointing angles. The large number of peaks observed at ion acoustic velocities is not predicted.

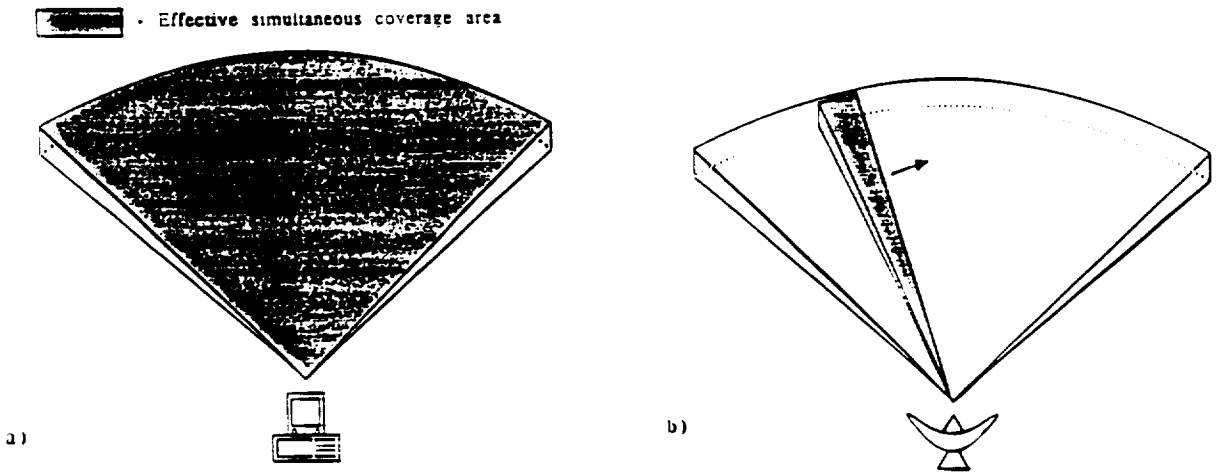

Figure 5-6: Graphical illustration of procedures used for a) satellite simulations where the entire space window is continuously monitored, and b) actual data acquisition via scanning radar beam in experiment.

difference between the simulations shown thus far and actual experiments is illustrated graphically in Figure 5-6. Hence, the number of satellites actually detected in a 12 hour observational period is much smaller than the number "seen" by the catalog for the same 12 hours, and a comparison of the corresponding observed distribution may not be statistically valid.

The minimum time required for a valid statistical comparison of observed and simulated coherent peak velocity distributions was determined by simulating a computer radar beam scanning through a dynamic satellite field. In the simulations, the table of satellites passing through the azimuth window were sorted according to time, and a radar scan was initiated at a given time and starting position to sample the satellite data base. The simulated scan consisted of a $2° \times 2°$ wide beam which was swept 10°/min in azimuth, the same azimuth scan rate used in most experiments at Millstone Hill. This process was repeated several times using different initialization

parameters for periods of 12, 24, and 48 hours.

It took 4–5 times more scanning hours to acquire as many targets as the corresponding open window simulation. The 12 hour simulations produced distributions which were usually similar to the open window distribution, but in some cases relatively large disparities were evident. The 24 hour simulations improved results. None of the 24 hour distributions, for example, predicted more peaks at ion acoustic velocities than at polar orbiter velocities, as was observed in the NOV87 experiment. Nevertheless, deviations from the open window distribution were large enough to discourage quantitative comparison. After 48 hours, however, the scan simulations matched the shape of the open window results nicely, regardless of starting time or position within the satellite data base: increasing the time further simply produced more events without noticeable distortion of the distribution.

The data sets used to produce the observed distributions presented in Figures 5-4b and 5-5b contain at least 60 continuous hours of radar observations, and should therefore satisfy the statistics of the satellite catalog simulations. Comparing the simulations with the observed distributions we conclude that a number of the coherent peaks observed at ion acoustic velocities between 1–2 km/sec in the NOV87 experiment result from geophysically induced ERB. The levels of global magnetic activity during the period varied from quiet to unsettled to moderately disturbed ($0 < Kp \leq 5^-$). Extrapolating the number of ERB events occurring during this moderate activity to the extremely disturbed periods of the JAN88 experiment, we would expect to find much stronger evidence for geophysical ERB in the January velocity distribution. The lack of such evidence can be explained by considering the results of a statistical analysis of a third experiment.

Altitude Discrimination Coherent echo distributions were constructed from approximately 80 hours of data acquired during an experiment on 6–10 March 89, which

was known to contain magnetically disturbed periods. The velocity distribution of the enhanced echoes observed during the experiment, however, very nearly matched the corresponding distribution generated by the satellite catalog. The observed altitude distribution of the enhanced returns, shown in Figure 5-7, also looks quite similar to the simulated satellite distribution shown in Figure 5-3, except at the lowest altitudes, where a surprisingly large number of peaks are observed in range gate 10, corresponding to 330 km altitude.

The number of orbiting objects at altitudes of about 300 km or less represents less than .5% of the total satellite population. In the observed distribution, however, such events account for nearly 1.5%. For this experiment that translates into precisely 18 events, a small number which is perhaps not statistically robust, despite 80+ hours of observations. The significance of the low altitude anomaly increases when one recognizes that the number of events near 300 km is comparable to, or greater than the number of peaks detected at altitudes of 500 and 540 kilometers, respectively. An examination of the spectral characteristics of each low altitude enhancement provided further evidence of a geophysical source for some of the enhancements.

Satellites at low altitudes must travel faster than orbiting objects at higher altitudes; a satellite simulation for the 6–10 March azimuth scans shows that about 85% of the time, the line-of-sight Doppler velocity detected by the radar from these objects exceeds 4 km/sec, and is often higher than 7 km/sec. In the March experiment, however, 5 of the 18 low altitude enhanced peaks exhibited Doppler velocities at the local ion acoustic speed, usually between 1 and 2 km/sec in the F region. This is almost double the expected percentage of ion acoustic enhancements, and seems unlikely to be a random occurrence caused by hard targets. The occurrence of these events with regard to magnetic activity and other geophysical considerations is also indicative of ion acoustic enhancements through natural processes.

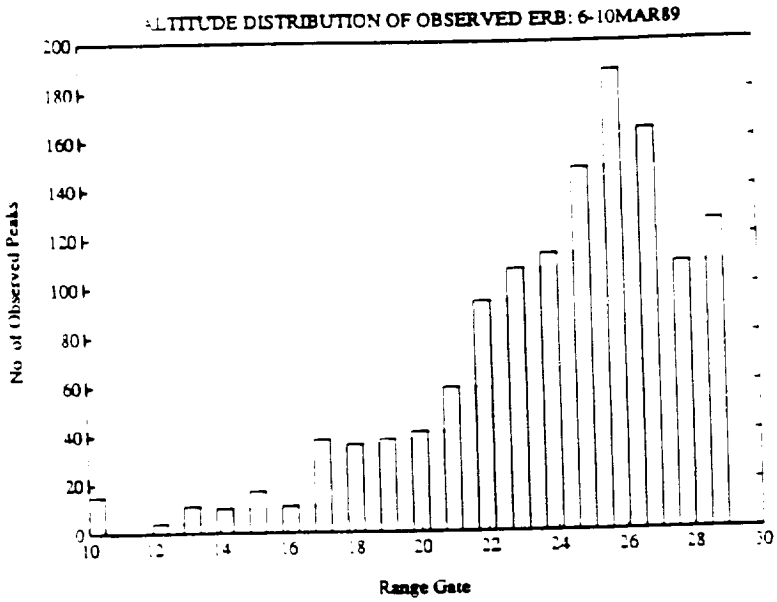

Figure 5-7: The altitude distribution of observed coherent echoes from the Millstone 6–10 March 1989 experiment. Altitude is scaled by range gates, which are separated by 40–50 kilometers. Some gate numbers followed by their corresponding altitude are: 10/330, 15/500, 20/700, and 25/975.

This March experiment time period was very interesting magnetically, being more disturbed than the 8–10 NOV87 period, but significantly less disturbed than the monster storm levels recorded during 13–15 JAN88. The hourly AE index is plotted for the duration of the experiment in Figure 5-8. The AE index provides a useful measure of auroral magnetic activity. The figure shows that March 6–7 were moderately disturbed before activity decreased steadily through the latter part of the 7th and March 8. At 18:00 UT on the 8th a major storm commenced; disturbance levels decreased soon after the major impulse, but remained active throughout most of March 9 when another surge of activity occurred, lasting just til 24:00 UT.

The height of the maximum density in the F region, $hmF2$, is closely related to the magnetic activity (see Figure 5-9). Under quiet conditions, $hmF2$ exhibits a regular diurnal variation, descending during daylight hours as photoionization builds up the plasma density at lower altitudes, and ascending again after dusk when recombination processes neutralize the low altitude plasma more rapidly. A typical variation

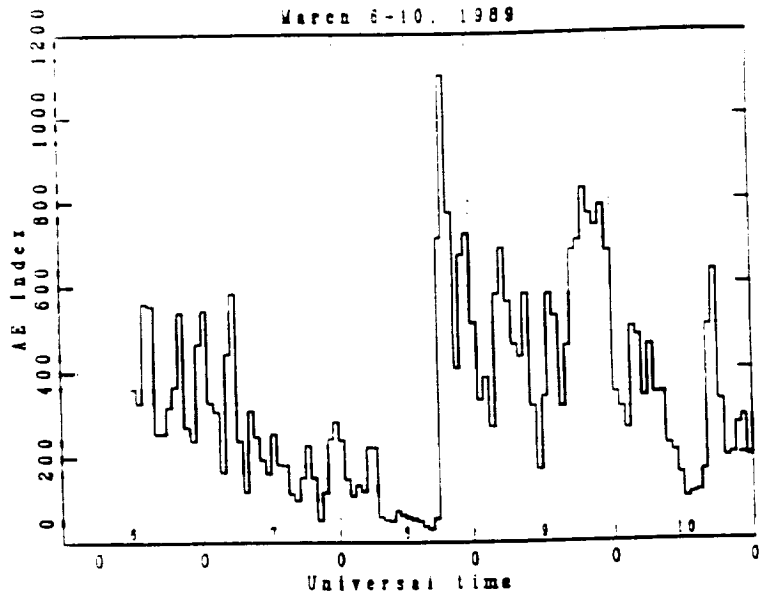

Figure 5-8: Values of magnetic index AE during the magnetic disturbances of 6–10 March, 1989. Note the sudden storm commencement at 18:00 UT on March 8 [after *Buonsanto et al.*, 1990].

of this nature is evident during the period of decreasing magnetic activity spanning March 7–8. Under magnetically disturbed conditions $hmF2$ serves as an excellent indicator of the passage of the mid-latitude electron density trough and the equatorward expansion of the auroral oval [*Buonsanto, et al.*, 1990]. In the trough itself, the $hmF2$ value increases sharply, as occurs in the early morning hours of March 7, March 9, and March 10.

The low altitude ion acoustic enhancements occurred at 7MAR-1:44 UT, 9MAR-3:34 UT, 9MAR-11:52 UT and 10MAR-3:00 UT. Their positions are indicated on Figure 5-10, which is a plot showing the variation of the peak ionospheric density, *NMF2*, as a function of time and latitude. All the enhanced peaks occur either in the ionospheric trough or on the trough's equatorward edge in a region of strong density gradients associated with field-aligned Birkeland currents [*Ungstrup, et al.*, 1986]. Except for the event at 11:52 UT on March 9, all the events occur just prior to the arrival of the trough over Millstone Hill. The event at 11:52 UT is actually occurring under similar geophysical conditions, except that it is located on the edge

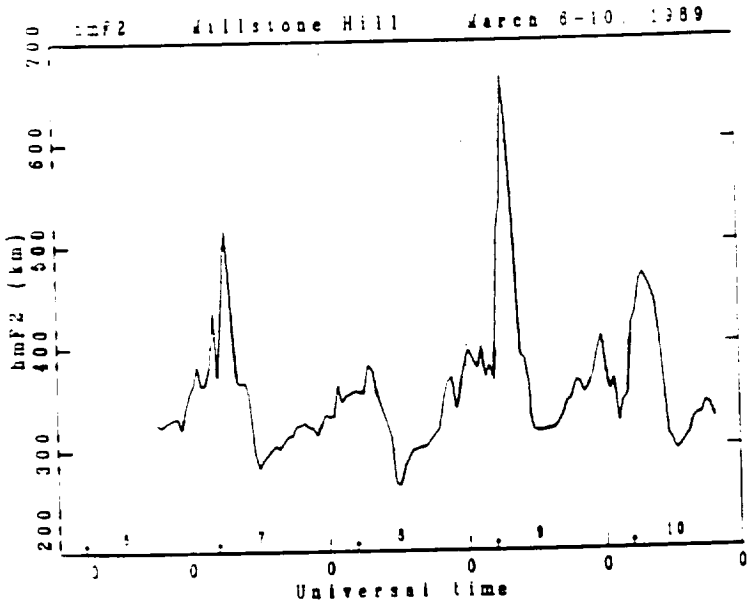

Figure 5-9: The height of maximum electron density in the ionosphere for the 6–10 March period. The sharp increases in altitude correspond to the approach of the mid-latitude trough [after *Buonsanto et al.*, 1990].

of a receding, rather than approaching, density depletion.

The approach of the trough signals the expansion of the auroral oval and the penetration of large electric fields to lower latitudes. These fields are responsible for the very large westward $\mathbf{E} \times \mathbf{B}$ plasma drifts observed in the early morning on March 9. The enhanced low altitude ion line detected at 3:34 UT on March 9 is shown in Figure 5-11: the large shifts evident in the normal IS spectra at higher altitudes correspond to westward drifts of up to 1.3 km/sec. All-sky images revealed that prominent red aurora were present north of the Millstone Hill radar at this time, in the same location where the ERB occurred; later in the morning a stable red auroral (SAR) arc persisted to the north for about two hours [*M. Buonsanto*, private communication, 1991]. These geophysical signatures verify the presence of auroral features at latitudes as low as 44° on March 9. Similar features, though not as intense, were present during the early morning hours of March 7 and 10 as well. By contrast, the post-dusk period on March 7/8 did not display a well-defined trough or auroral characteristics. The density depletion evident after midnight on this day

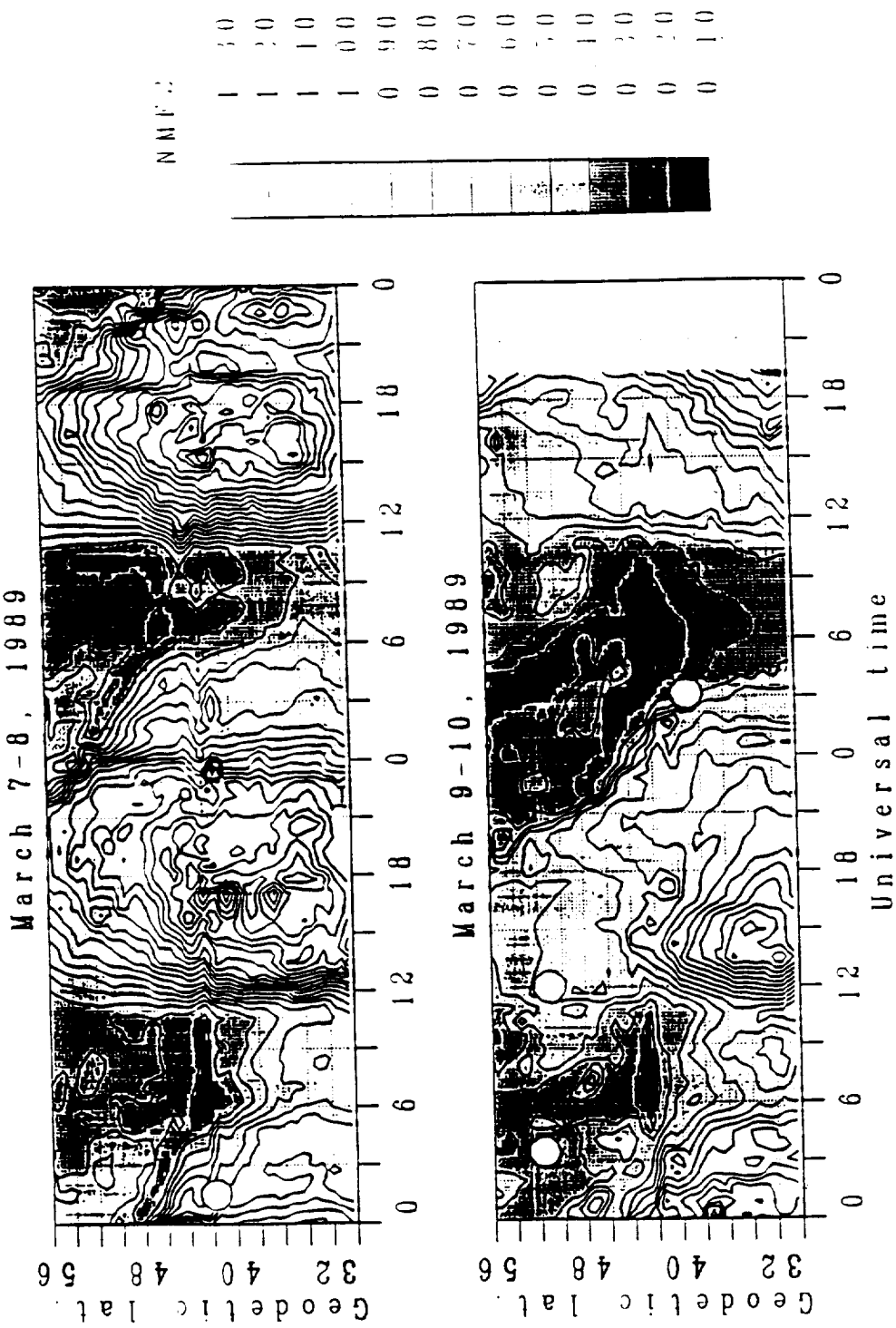

Figure 5-10: Variation of peak electron density with latitude. Low altitude ERB events are indicated with white dots. Low density regions are shaded black [after *Buonsanto et al.*, 1990].

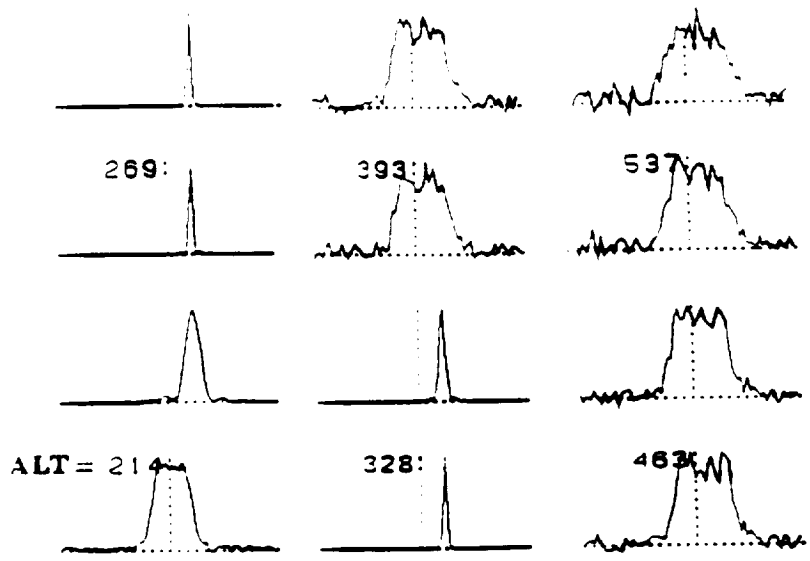

Figure 5-11: Ion line enhancement observed with the Millstone Hill UHF radar at 03:34 UT on 9 March 89. At higher altitudes the shifted spectra give evidence of large westward $\mathbf{E} \times \mathbf{B}$ drifts.

is associated only with the normal diurnal decrease occurring after sunset. No low altitude ion acoustic ERB events were recorded during this time period.

We have established the presence of active auroral features during the periods when low altitude ERB events were observed in the 6–10 March experiment. These events are attributed to the enhancements of ion acoustic waves in the presence of naturally occurring intense field-aligned currents. Normally the Millstone Hill Radar can diagnose these remote high latitude active regions only at altitudes above 500 km, where the large satellite population makes unambiguous identification of ERB events difficult. During the magnetic disturbances of March 6/7, March 8/9 and March 10, the equatorward expansion of the auroral oval carried it to within a few degrees of Millstone's latitude. This made it possible for low elevation-angle azimuth scans to sample the active region at much closer ranges, and correspondingly lower altitudes, than normal. The low altitude ERB events were then relatively easy to separate from hard targets because so few satellites occupy these very low altitude orbits. The variability of the ionosphere played an important role in interpreting the results of

the distribution studies for this experiment.

The level of variability in the 13–15 JAN88 experiment was about an order of magnitude greater than that experienced during 6–10 MAR89. By extending the auroral dynamics arguments used to explain the results of the MAR89 experiment, we can arrive at a rational explanation for the total lack of statistical evidence of geophysical ERB during the JAN88 experiment. In MAR89, ionospheric variations were characterized by brief periods of intense magnetic activity resulting in the equatorward expansion of the the auroral oval to latitudes slightly north of Millstone Hill. The periods of intense activity were then followed by somewhat longer periods of decreased activity, providing a relaxation period for the ionosphere to nearly return to its normal structure.

After the first day of the 13–15 JAN88 experiment, however, periods of extreme activity were sustained for many hours. The auroral region, containing the intense current activity critical for ERB excitation, actually passed to the south of Millstone Hill and did not recover to its usual latitudes during the duration of the experiment. The radar scan cycle employed, a 4° elevation-angle, limited azimuth scan to the north, was not advantageous to the detection of ERB under these circumstances. Zenith measurements or even scans to the south of Millstone are appropriate for such studies under very disturbed conditions. In conclusion, ERB events were not detected in the JAN88 experiment because the auroral zone passed to the south of Millstone Hill due to extreme levels of magnetic activity, while the radar continued to scan at low elevation angles to the far north.

Finally, a large data set acquired on 6–10 October 86 was analyzed by the same statistical technique. The observed velocity distribution closely resembled the satellite distribution, similar to the comparison shown in Figure 5-4. Furthermore, an analysis of the altitude distributions yielded no evidence of anomalous ERB events. The global

Kp index indicated that the period was one of the most quiet imaginable, with 60 of the 87 observing hours having Kp of 1^+ or less and a maximum Kp of 3^- occurring for one 3-hour period. Under these conditions, intense current activity is not expected at any latitude within Millstone Hill's field-of-view. Consistent with that interpretation, we conclude that the lack of evidence of ERB events in the statistical analyses for this experiment indicates simply that no appreciable ERB events occurred during this time period because of the very low levels of magnetic activity.

5.2.2 MICAD Experiments

Beginning in April 1989, a series of multi-diagnostic experiments, known as MICAD, involving the MIllstone Hill UHF radar, a subset of the CANOPUS system of instruments (BARS radar, magnetometer array, meridian photometers) and the DE-1 satellite was conducted to provide additional information about ion acoustic radar backscatter enhancements due to ionospheric processes. In these experiments, as illustrated in Figure 5-12, the Millstone Hill radar was used to track the geomagnetic field line above the DE-1 satellite as it flew through perigee within the radar's field of view; CANOPUS instruments were utilized as diagnostics of the background ionosphere. Ultimately, the goal was to simultaneously detect the signature of large, field-aligned ionospheric currents with remote sensors (radars, etc.) and in situ instruments aboard DE-1.

Beginning in April 1989, a total of seven MICAD overflight experiments were conducted on 4/9, 5/2, 5/22, 6/5, 6/19, 8/8, and 8/29. During the MICAD experiment on 22 May 1989, the Millstone Radar detected a 7 dB enhanced backscatter return at the ion acoustic frequency at 23:57:46 UT; the power enhancement at 1000 km is shown in Figure 5-13. The power plot shows a distinct F region trough at the latitude of the ERB event. In the scan shown in the figure the radar moved

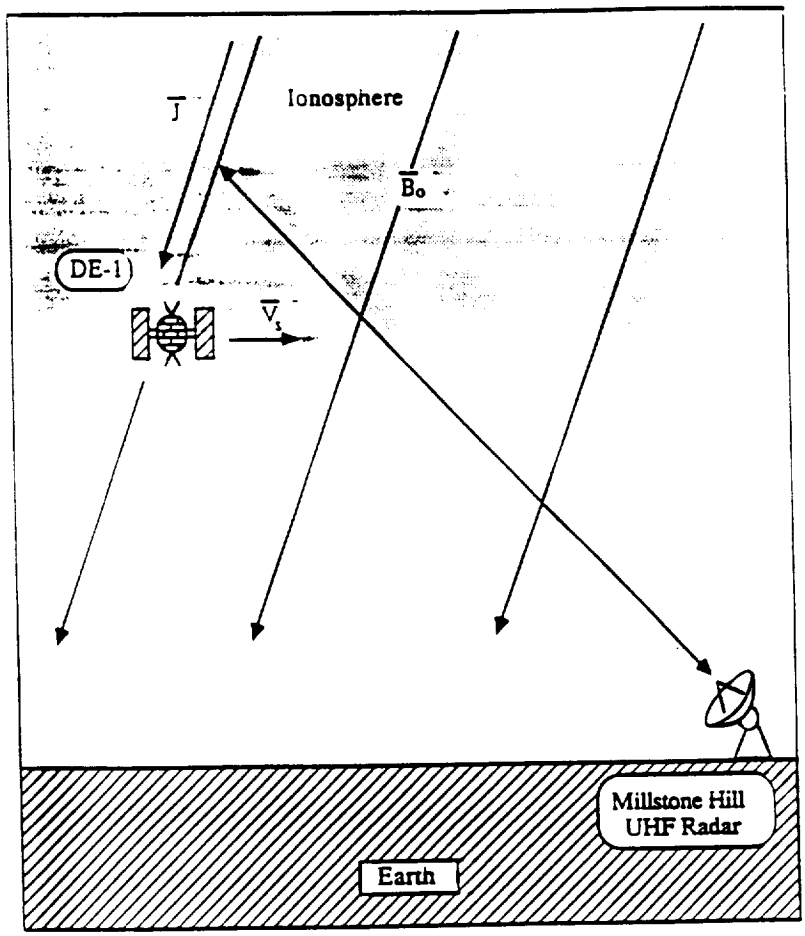

Figure 5-12: Conceptual design of MICAD experiments. Remote diagnostics and in situ instruments were to obtain simultaneous measurements on the same magnetic field line.

from AZ=289° at 23:54:52 UT to AZ=343° at 23:59:08 UT. The enhancement occurred at an azimuth of 332°. The DE-1 satellite passed through the same region 30 seconds later and recorded an in situ magnetometer fluctuation corresponding to a field-aligned current density ≥ 50 μamps/m^2 [*J. Slavin*, private communicaton, 1989]. The magnetometer trace and the enhanced UHF radar spectra are shown in Figure 5-14. The decrease in the magnitude of DBPHI evident just after 23:57:00 UT in the figure indicates the satellite's entry into the Region II field-aligned current system. The boundary between the Region I currents and the Region II currents is reached at about 23:58:10 UT, when the $\sim$ 50 μamps/m^2 current spike was detected. The onboard magnetometer continued to exhibit large fluctuations until about 23:59:00 UT; two of the additional fluctuations at 23:58:20 UT and 23:58:40 UT correspond to current densities in excess of 25 μamps/m^2. Because the radar was actually tracking about 30 seconds ahead of the satellite's position, the measurements cannot be classified as truly simultaneous. However, this experiment gives firm evidence of intense field-aligned currents associated with the occurrence of ERB near the ionospheric trough as was suggested by FOS88.

An examination of data from two consecutive passes of the DMSP-F8 satellite (the first 42 minutes prior to, and the second 56 minutes after the DE-1 overflight in the same longitude band) reveal that the region producing the enhanced radar backscatter was characterized by localized intense, soft ($E \leq 1$ keV) electron precipitation features. Comparison of the measured electron and ion fluxes show that current densities in excess of 60 μamps/m^2 were detected on the first pass [*W. Denig*, private communication, 1989]. Data from this pass formed the basis for deriving the suprathermal contribution to the electron distribution function utilized in numerical calculations in Chapter 7 (see Figure 7-7).

Particle flux spectrograms from a northern polar pass of the NOAA-10 satellite

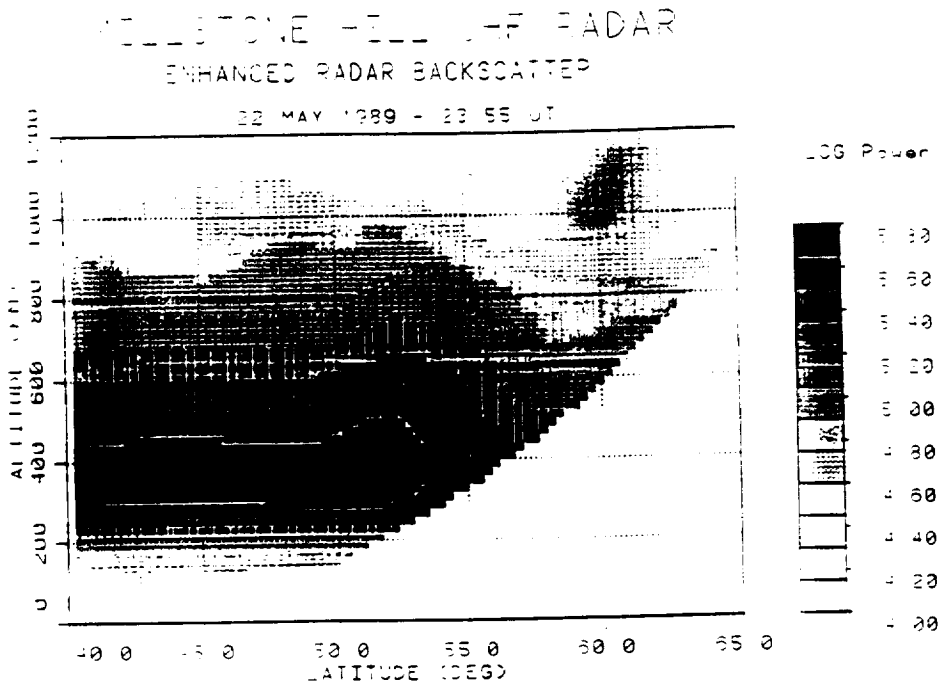

Figure 5-13: Power enhancement observed during May 22 MICAD experiment. The 7 dB enhancement is located at 1000 km altitude on the edge of the ionospheric trough. A two msec radar pulse was used in the scan.

exhibit a sharp local maximum in the low energy electron flux at the same latitude and only 8 minutes prior to the DE-1 satellite and Millstone Hill radar observations. A map illustrating the geographic and temporal relationship of the various measurements is shown in Figure 5-15. These in situ data establish the presence of discrete low energy particle precipitation events carrying large current densities in the region of enhanced UHF radar backscatter.

It should be noted that limited particle flux information is available from the DE-1 satellite. The electron flux instrument onboard is no longer functional. The energy spectrum of ions was monitored, but no signature was evident in association with the large magnetometer variations [*W. K. Peterson*, private communication, 1989]. This is consistent with the DMSP data, where the energy flux of the electron population increases dramatically while the ion flux remains essentially unchanged. Both measurements indicate that the currents are being carried by suprathermal

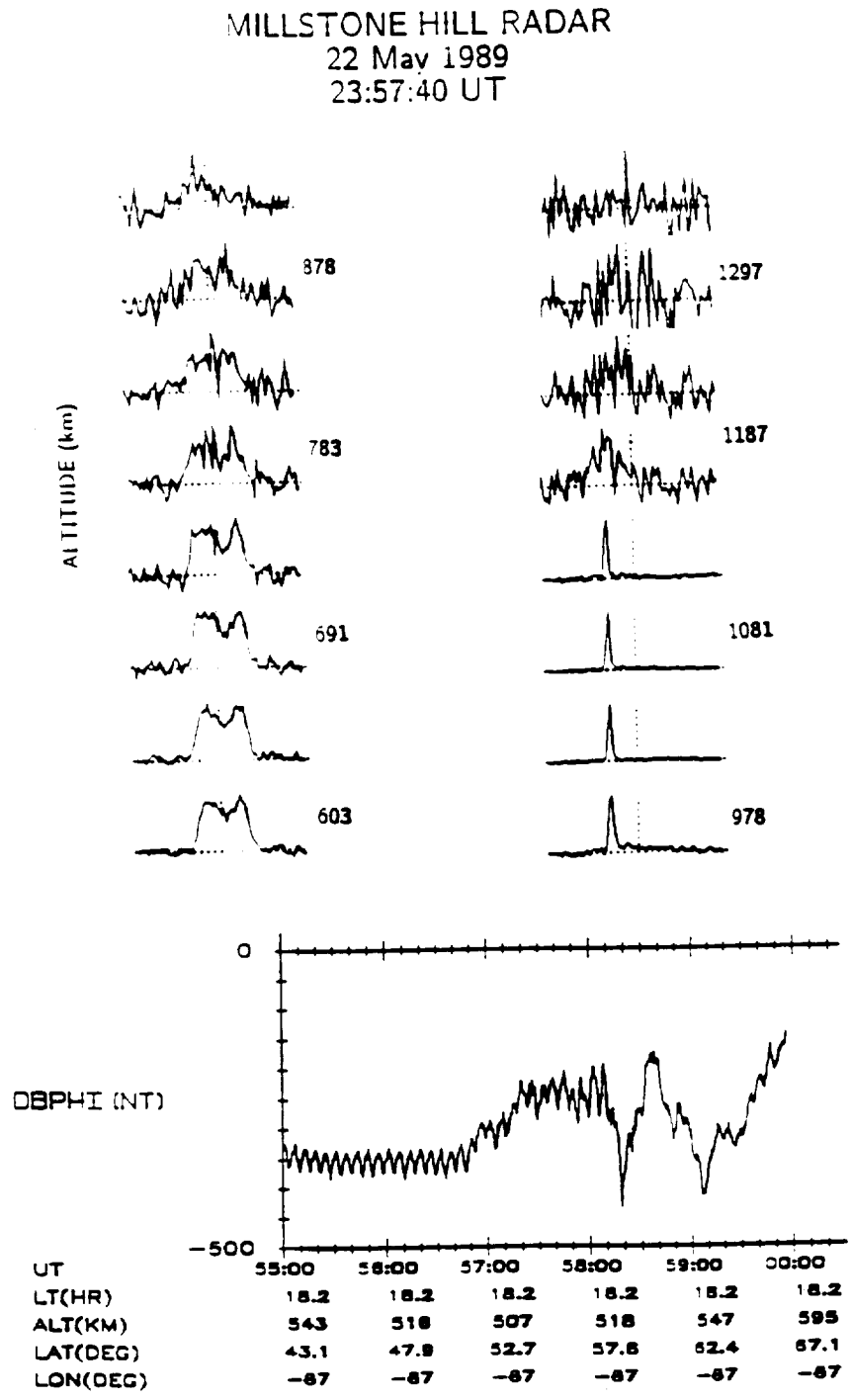

Figure 5-14: Power spectra of ion acoustic ERB observed with the Millstone Hill UHF radar and the corresponding magnetometer trace of the DE-1 satellite. Magnetic fluctuations (DBPHI) are in units of nanotesla.

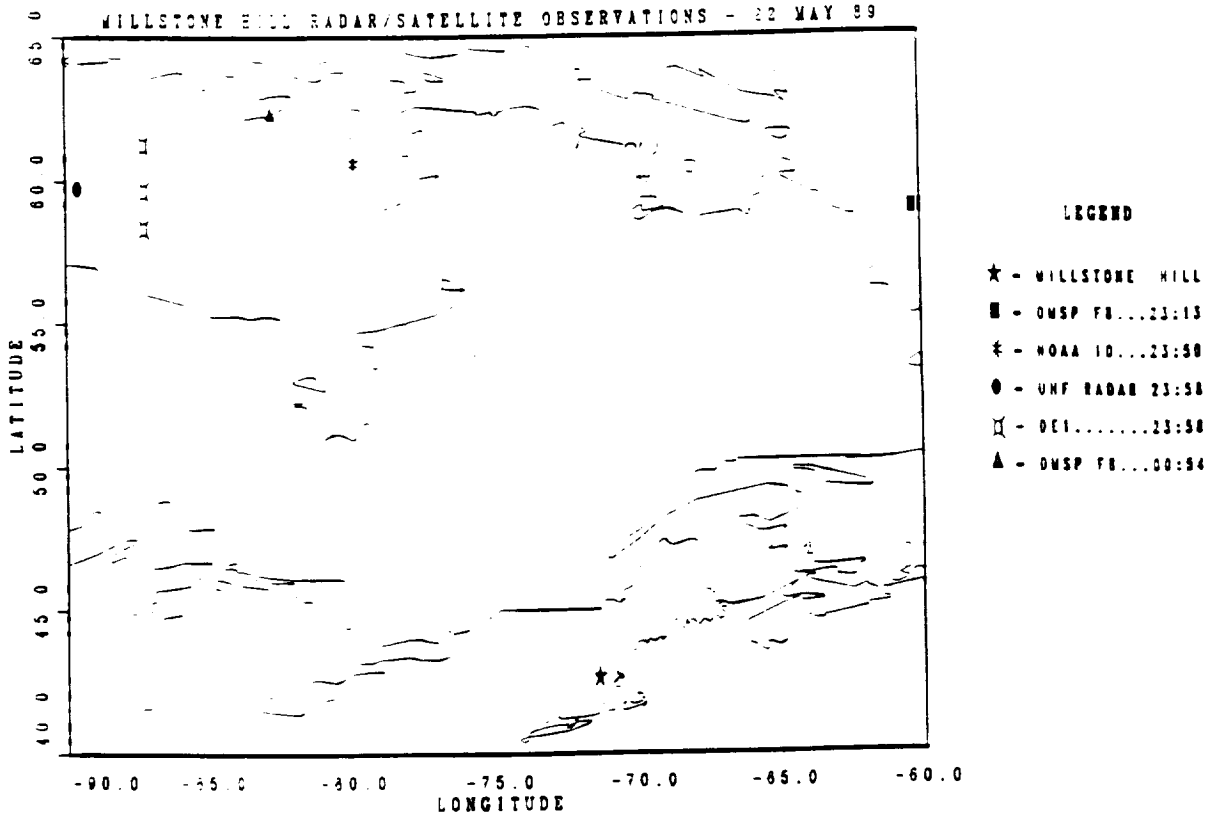

Figure 5-15: Map showing geographic relationship of multiple satellite measurements of intense field-aligned current activity, UHF ion acoustic ERB, and the Millstone Hill radar.

electrons rather than ions.

Measurements from the CANOPUS diagnostic group of instruments were of limited application in this particular MICAD experiment. The observations were outside the field-of-view of the BARS radar system, and the local time was too early to acquire all sky camera images of visible airglow or photometer data. The meridional magnetometer chain (MARIA) approximately 320 km west of the UHF ERB observation was operating, and the magnetometer traces from the nearest stations are shown in Figure 5-16. The ground stations show a reasonable level of activity (Kp=4) prior to the Millstone/DE-1 observations, but conditions are relatively quiet during the actual overflight (about 2 hours after start time). Global magnetic activity usually serves as an indicator of intense field-aligned currents, but it does not constitute a prerequisite for their occurrence. Johnstone and Winningham [1982] reported several

satellite observations of suprathermal electron bursts carrying field-aligned currents in the auroral zone during very quiet magnetic conditions.

The satellite catalog was consulted for the presence of hard targets in the scattering volume during the 30-second integration period in which the ion acoustic ERB event was recorded. A generous scattering volume was assumed, using the actual elevation and azimuth angles of the radar $\pm 2°$, to minimize the uncertainties due to errors in the catalog predicts. Three candidates were found. Of these three, two were expected to produce large line-of-sight Doppler shifts of about 6 km/sec. The other possible candidate's Doppler velocity was in the opposite direction of the observed phase velocity of the enhanced ion acoustic peak. Clearly, none of the predicted hard targets could have caused the asymmetric UHF power spectrum observed in this MICAD experiment.

5.2.3 Observation of ERB in Zenith Experiments

As has been established, the contamination due to satellites in the investigation of ERB is a serious problem in general. However, hard target signatures can be filtered out effectively by pointing the radar directly overhead. In the zenith position the beam is nearly transverse to the direction of motion of satellites penetrating the scattering volume, and their associated Doppler shifts are thus restricted to nearly zero magnitude. Satellite catalog simulations based on a $2° \times 2°$ wide beam show that the maximum observable line-of-sight velocity possible in such experiments does not exceed 250 m/sec. Zenith observations of spectral peaks with greater Doppler shifts (*e.g.*, F-region ion acoustic speed: C_s ~1-2 km/sec) can then be attributed to geophysical sources.

Figure 5-17 shows an observation of ion acoustic wave growth acquired with the Millstone Hill 67-meter fixed position zenith antenna. The Doppler shift of the peak

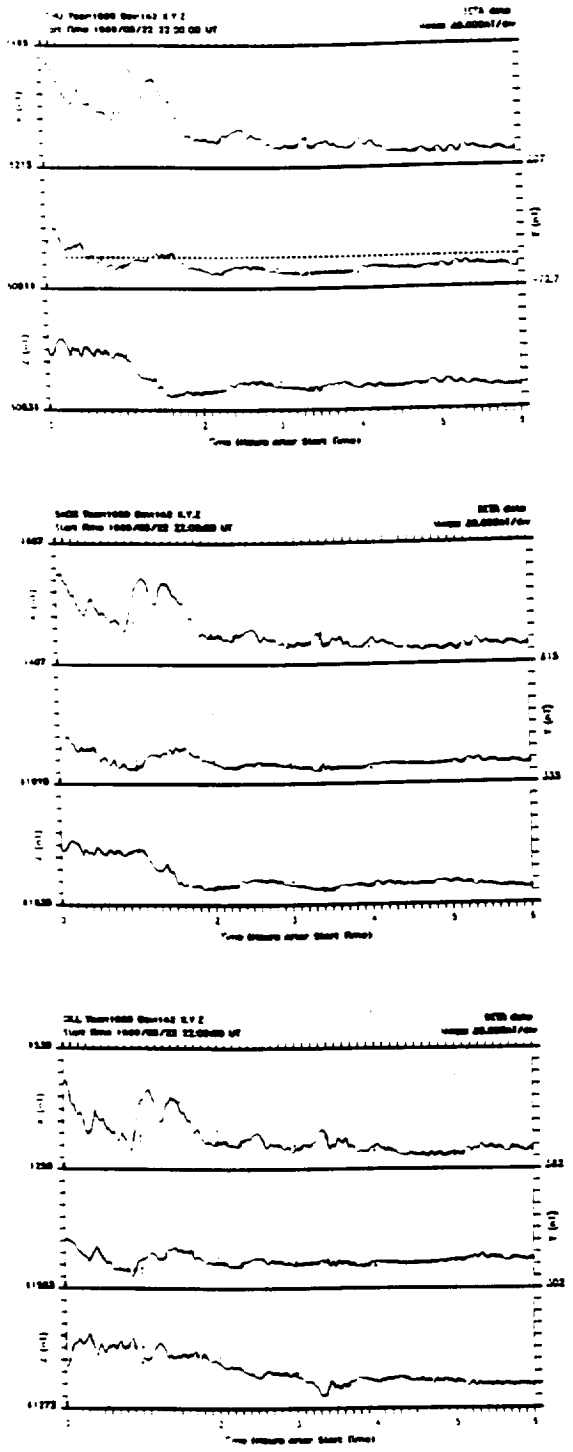

Figure 5-16: Magnetic variations recorded by the CANOPUS chain of magnetometers during the May 22, 1989 MICAD experiment. The DE-1 and Millstone Hill observations of ERB were recorded at 23:58 UT, during the relatively quiet period nearly two hours after the start time on the plots.

corresponds to a 1 km/sec velocity, about four times greater than the maximum observable shift from actual satellites. In addition, the enhanced return is distributed in altitude to a greater extent than is possible for an orbiting object given the 150 km pulse smearing along the radar beam. This zenith observation, reported by FOS88, was taken as proof that a portion of the Millstone ERB returns cannot be caused by orbiting objects.

The scan cycle for the radar in this experiment consisted of 4 consecutive zenith measurements followed by a complete elevation scan, 2 more zenith records, and a 180° low elevation-angle azimuth scan. Only six minutes out of every hour are spent in the zenith position, and only half that time is used to diagnose the high altitude region above 700 km. Unfortunately, the spectra shown in Figure 5-17 represent the last zenith measurement preceding the beginning of an elevation scan lasting six minutes. When the radar returned to the zenith position, the echoes were gone.

Observations like this at Millstone Hill are rare for two reasons. As was noted previously, the enhancements are thought to be associated with intense field-aligned currents. While such events are not extraordinary at auroral latitudes, they occur at mid-latitudes very infrequently, approximately 10–15 days a year based on the Kp magnetic index during the event shown here [*Mayaud*, 1980]. On those days when the general levels of disturbance are sufficient, the phenomenon directly over the radar may last for only minutes or seconds and be missed entirely [*Rietveld et al.*,1991], as was nearly the case in this experiment.

Typically only a small amount of Millstone's total data acquisition time is used for zenith observations. Few dedicated zenith experiments have been conducted at Millstone Hill in the past: two separate 24-hour experiments run recently yielded no significant results. The zenith data obtained in most previous experiments consists of a few local measurements made once or twice per hour in between azimuth and/or

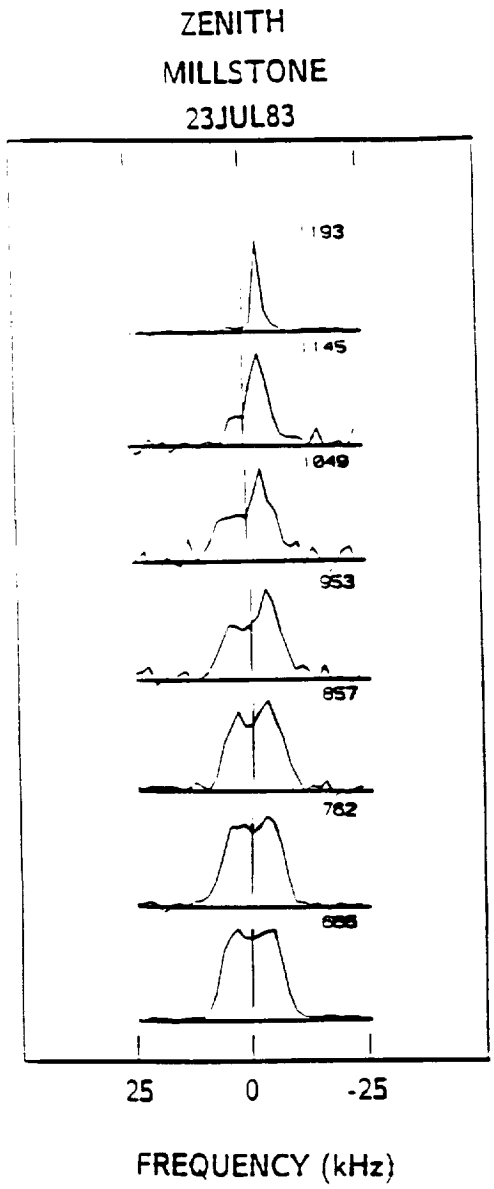

Figure 5-17: Millstone Hill zenith observation of ion acoustic ERB. The frequency offset corresponds to a velocity of 1 km/sec. [after FOS88].

elevation scans. Considering the low occurrence frequency of the geophysical event and the sparse number of zenith observations, the probability of detecting ion acoustic enhancements directly above Millstone Hill is small: zenith experiments conducted solely for that purpose may not provide an effective approach for investigating ERB at mid-latitudes.

5.3 Summary

An attempt has been made to provide conclusive evidence of geophysically-produced enhanced ion acoustic radar backscatter observed at Millstone Hill.

Because of the spectral similarities of satellites and enhanced ion acoustic waves, it is difficult to distinguish individual measurements unambiguously. Satellite simulations have been employed to make statistical comparisons with large data sets. Results from four types of experiments have been presented. Under extremely disturbed and extremely quiet conditions no ERB events were detected by the statistical analysis. In the quiet case there are most likely no occurrences of ERB. In the very disturbed case, however, pointing the radar to the north proved ineffective because of the auroral region's passage to the south of Millstone. ERB events were found at low altitudes during a lesser storm period when the auroral oval expanded to within a few degrees north of Millstone. These events have been attributed to the current-driven enhancements of ion acoustic waves in the temporarily nearby auroral zone. Finally, a moderately disturbed period was examined. The velocity distribution exhibited many more peaks at ion acoustic frequencies than predicted by the satellite catalog. These peaks are believed to represent geophysical ERB events occurring at relatively high latitudes in the usual auroral zone.

Through a series of multiple diagnostic experiments, we have established the association of enhanced backscatter events with intense field-aligned currents. In one case,

a nearly simultaneous measurement of UHF ERB and a field-aligned current carried by suprathermal electrons were obtained. Data from other satellites confirmed that the region contained large fluxes of low energy electrons, and that such conditions persisted for tens of minutes. These soft precipitating electrons are believed to play an important role in the generation of ion acoustic ERB.

Finally, the utility of zenith-pointing experiments was exploited to filter out hard target contamination while acquiring ion acoustic ERB. A single event has been identified with a Doppler shift of 1 km/sec, the local ion sound speed in the plasma. Satellites passing through the beam exhibit Doppler shifts of less than 250 m/sec. These measurements are rare at mid-latitudes because intense field-aligned currents occur there very infrequently (perhaps briefly on 10–15 days/year during solar maximum), and the radar is not usually pointed in the zenith direction while acquiring data. Results from two 24-hour zenith experiments yielded no evidence of ion acoustic ERB.

Chapter 6

ERB Observations from Other Radar Sites

The existence of geophysically induced enhanced coherent radar backscatter from the topside ionosphere was first reported by FOS88 based on a study of "hard target" like returns observed with the Millstone Hill UHF Radar as described in Chapter 5. The enhancements are believed to be associated with intense field-aligned currents in the high latitude ionosphere. This high-latitude region is normally accessible to the Millstone Hill radar beam at very large aspect angles relative to the geomagnetic field, effectively limiting the range extent over which the field-aligned echoes may be observed and leading to ambiguities (with actual hard targets) in the data interpretation for individual coherent echo events. The locations of the EISCAT and Sondreström radars (see Table 4.1) suggest that more favorable ERB observing conditions may exist at those sites. Presented here is a brief overview of significant observations and experiments involving these radars which confirm and extend the known characteristics of ERB first recognized at Millstone Hill.

6.1 Observations at EISCAT

The EISCAT (European Incoherent SCATter) Scientific Association operates a tri-static UHF radar system consisting of a 933 MHz 2.5 MW radar located at Tromsø, Norway (69.7°N lat. 19.2°E.long) and two remote receivers at Kiruna, Sweden (67.8°, 20.4°) and Sodankylä, Finland (67.4°, 26.6°). The three sites utilize identical parabolic antennas 32 meters in diameter to simultaneously determine full three-dimensional vector velocities at selected heights in the ionosphere. In addition to the UHF radar, a 224 MHz radar using a 40 × 120 m parabolic cylinder antenna is located at Tromsø, providing multi-wavelength measurement capability locally.

6.1.1 Initial Statistical Approach

The investigation of ERB at EISCAT was first undertaken by Schlegel and Moorcroft [1989] who applied a statistical approach, similar to that used at Millstone Hill, to 73 hours of data acquired with the radar pointed up the local magnetic field line (AZ=182°, EL=77.5°). EISCAT regularly runs so called *Common Programs* for data acquisition which employ this radar look angle for geophysical reasons; such data constitute a majority of the available data base. Attempting to discriminate geophysical events from hard targets, Schlegel and Moorcroft's analysis identified and correlated 209 enhanced events with various combinations of occurrence time, altitude, velocity, intensity, and spectral characteristics. Achieving ambiguous results, they concluded that the ERB observed at EISCAT was probably due to a combination of satellites and system effects not clearly understood.

The satellite explanation was supported in part by a comparison of the distribution of observed peak velocities with the distribution predicted for hard targets by a satellite catalog. While this comparison was employed successfully with the Millstone Hill data, it fails to discriminate ERB events in this case because the field-aligned

pointing direction at EISCAT produces radar line-of-sight Doppler velocities from the large population of polar orbiting satellites in the range of typical ion acoustic velocities between 1–2 km/sec (see Figure 6-1).

However, a marked difference in the respective height distributions of satellites and the observed peaks was discovered. Shown in Figure 6-2 is the unexpectedly large population of observed low altitude events. Aware that reports of Millstone Hill ERB were restricted to the topside ionosphere above 400 km [FOS88] and lacking additional evidence of geophysical processes, Schlegel and Moorcroft were unable to resolve the disparity in the altitude distributions, leaving the question open for further interpretation. Recently, data reported by Rietveld et al. [1991] (henceforth RD91) unambiguously verified the detection of geophysically induced ERB with the EISCAT radar system.

6.1.2 Range Extended UHF Echoes

Like their counterparts observed at Millstone Hill, the geophysical ERB echoes detected at EISCAT were also characterized by large cross section enhancements (up to 20 dB) and narrow spectral widths similar to those caused by hard targets. These grossly asymmetric spectra cannot be fitted to derive ionospheric parameters by the standard incoherent scatter analysis programs. When the radar is pointed up the magnetic field line both satellite and geophysical ERB echoes appear at the same frequency shift in the power spectra. While this feature renders the field-aligned pointing direction ineffective for a statistical discrimination approach, it actually provides unambiguous geophysical ERB identification when events are considered individually for the following reason.

Enhanced echoes of geophysical origin were believed to be associated with intense electron drifts or currents [FOS88]. The most intense currents are also field-aligned

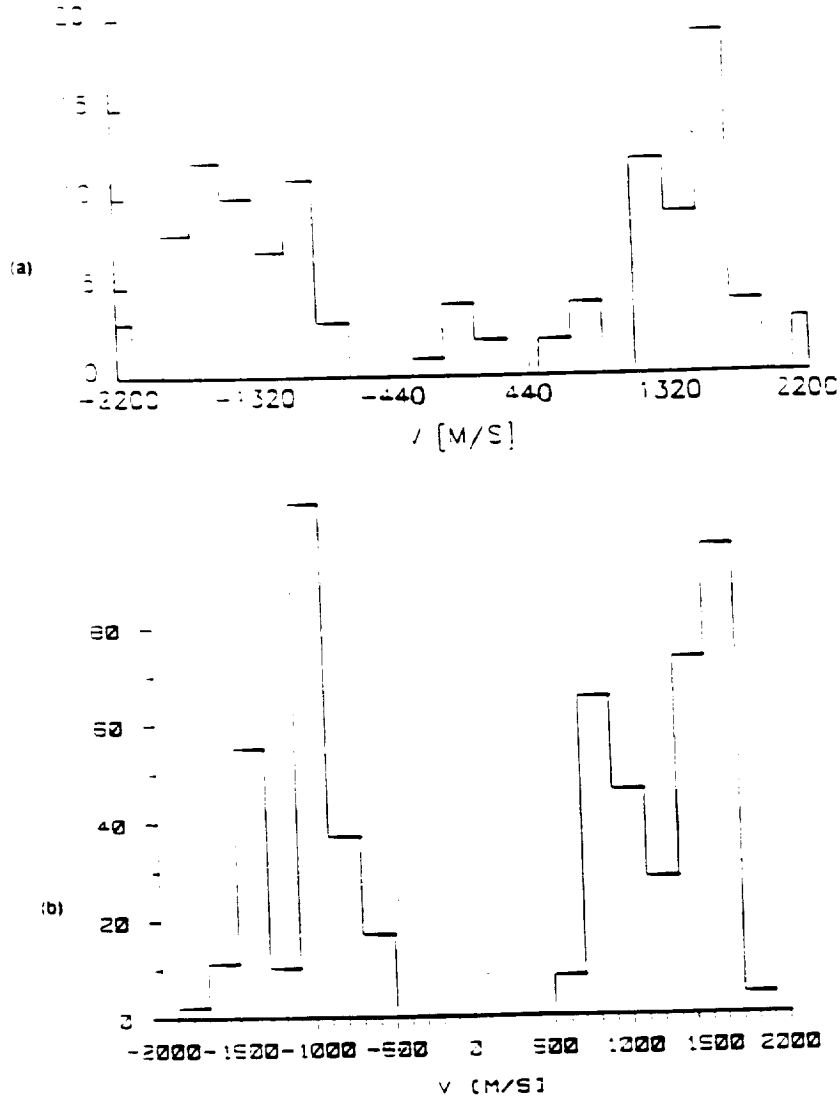

Figure 6-1: Histograms of velocity distribution of a) observed peaks, and b) satellite population. At this look angle geophysical enhancements and polar orbiting satellites share the same velocity range. [after *Schlegel and Moorcroft*, 1989].

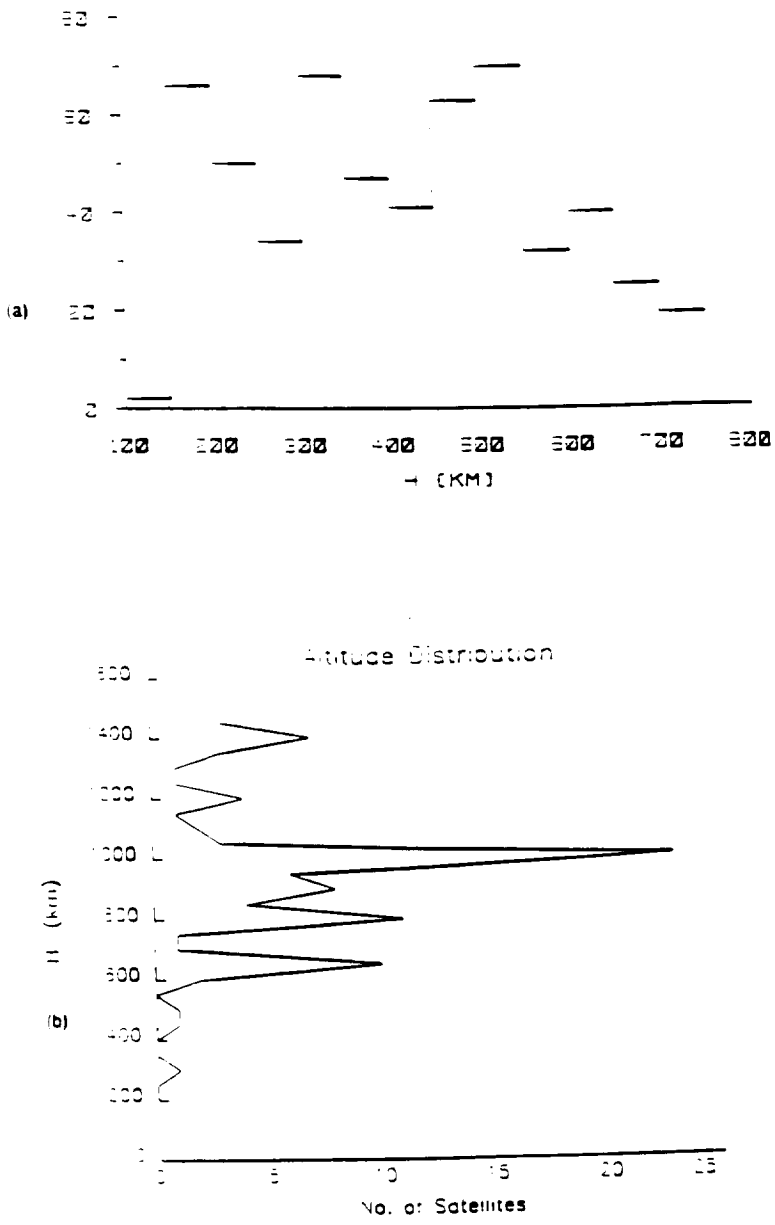

Figure 6-2: Histograms of altitude distribution of a) all observed coherent peaks, and b) satellite population. Note large number of observed peaks below 300 km. [after *Schlegel and Moorcroft*, 1989].

and extend for many kilometers along the magnetic field direction. Enhanced echoes driven by these currents are therefore stimulated over the same extent along the field lines and can be observed with a radar pointed parallel to the same line. (The altitude extent of the Millstone Hill zenith observations is attributed to this effect; see Figure 5-17). Range extended echoes were discovered by RD91 when investigating the details of a cluster of spectra which caused correlator errors due to overflows in the A/D converters of the radar receiver. Two experiments were analyzed (Feb. 14, 1990; Oct. 25, 1989), in which 24 ten–second integration periods were found to contain enhanced echoes. The following summary of those observations is adapted from RD91 and private communication with M. Rietveld, 1991.

A sample of the data is shown in Figure 6-3, where five consecutive 10-sec integration periods are shown which illustrate the transition from normal incoherent spectra to enhanced spectra and back again. The enhanced echoes are extended over a wide range of altitudes; a satellite penetrating the radar beam would appear in at most three range gates in the sampling technique used here. The frequency shift of the anomalous spectra also increases smoothly with altitude, corresponding to the increase in the ion acoustic speed with height, further evidence of the echoes' geophysical origins.

The spectra in Figure 6-3 vary dramatically during the 30 seconds in which the anomalous echoes appear. The spectra are enhanced at altitudes as low as 130 km and as high as 600 km by as much as 17 dB during the 04:49:50–04:50:00 period. The enhancements can be very asymmetric in either the upshifted or downshifted peak, or relatively symmetric with both ion acoustic peaks amplified by nearly the same amount. A transition in the sign of the frequency shift of the asymmetric peak enhancements can occur within a single 10 second integration period over several tens of kilometers. The statistics of which type of enhancement (asymmetric upshift,

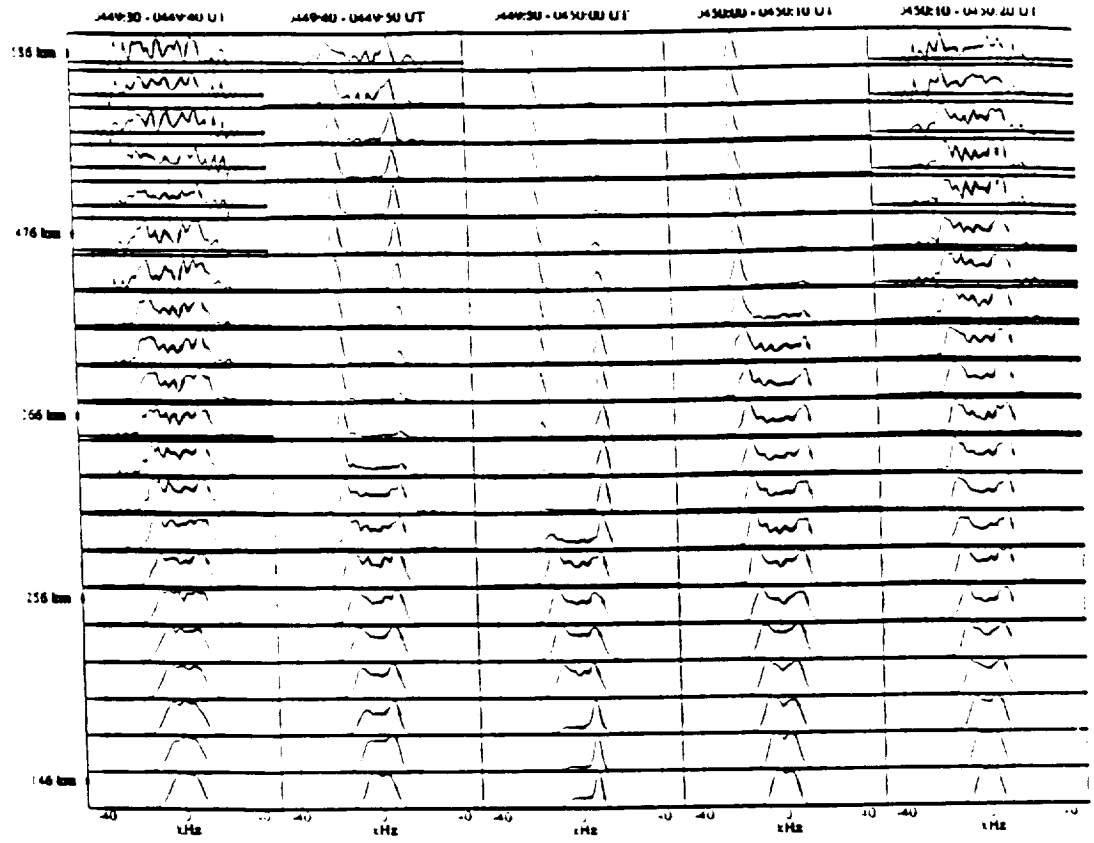

Figure 6-3: Five consecutive 10-sec integration periods observed with the EISCAT UHF radar. Within the 50-sec time period the ion lines change from normal to enhanced and back again [after RD91].

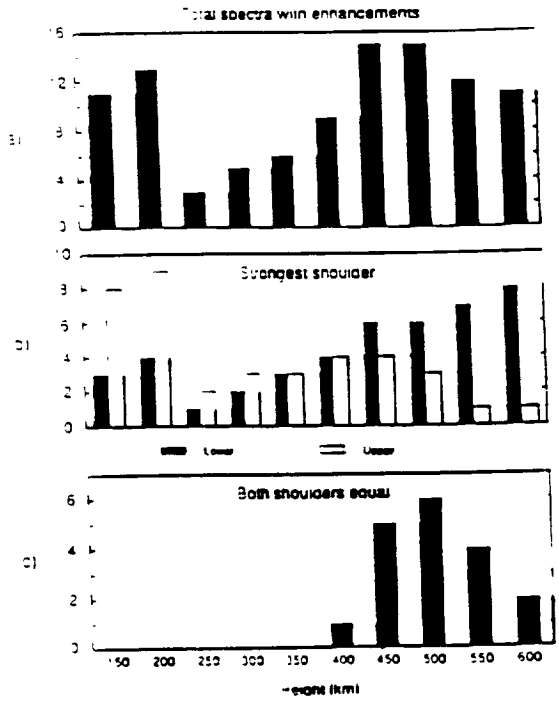

Figure 6-4: Histograms showing the height distribution of enhanced ion acoustic spectra categorized by a) total enhanced spectra: b) upshifted or downshifted peak enhancement: and c) both peaks enhanced symmetrically [after RD91].

asymmetric downshift, or symmetric) was observed in the two experiments under discussion are presented in histograms in Figure 6-4.

The figure indicates that there appear to be two main altitude regimes favoring the spectral enhancements, with a minimum rate of occurrence at around 250 km. In the higher altitude regime, the enhancements are primarily asymmetrically downshifted or symmetric; at lower altitudes upshifted asymmetric spectra are more common. The enhancements are found to be largest in the topside ionosphere above 250 km, and have lasted as long as 50 seconds continuously; shorter sporadic bursts distributed over a period of a few tens of minutes are seen more frequently. As more anomalous echoes from other experiments have been found, it appears that the low altitude enhancements are rare. Additionally, several ERB events have been observed when the radar was not pointed field-aligned, at was directed at aspect angles up to 20°. The echoes are then found to be localized rather than extended in range, as in the observations reported from Millstone Hill.

Geophysical Conditions

Geophysically, the events occur in the presence of sharp fluctuations in the local magnetic field ($\sim$ 500 nT N-S), auroral particle precipitation evidenced by airglow, elevated electron temperatures (T_e up to 8000°K), and electron-to-ion temperature ratios greater than two, though not extremely high (typically, $2 \leq T_e/T_i \leq 3$). Several more ERB events have been discovered in EISCAT data since RD91; some of these cases were more closely correlated with elevated ion temperatures, strong perpendicular electric fields, and little, if any, auroral precipitation [*Wahlund et al.*, 1991]. Based on an evaluation of the sparse existing data, the physical mechanisms responsible for the observed enhancements are explored in Chapter 7. A recently conducted experiment to obtain better data is described in the next section.

6.1.3 Dedicated ERB Experiment Performed at EISCAT

In late November 1990, EISCAT radar time to acquire new data was provided by Dr. Kristian Schlegel of the Max Planck Institute for Aeronomy, and a single experiment designed to measure ERB with the highest possible resolution in time and space was conducted. The methods and results of the experiment are presented below.

Experimental Description

Experimental considerations for conclusively obtaining good quality enhanced echoes were determined by our understanding of the phenomenon. The experiment was designed to provide high resolution (in frequency and time) power spectra over a large altitude extent, primarily at field aligned and vertical look angles. The field-aligned position facilitates observing enhancements over a large altitude extent, while the vertical position constrains the possible line-of-sight satellite velocities to subsonic speeds in the ionosphere and shares common scattering volume with the VHF radar.

Experimental Description

SP-GE-SAT
[illegible] 29/90. 16:00 UT - [illegible] 30/90. 08:00 UT

Radar Parameters (Block 1)
- pulse length 500 μs
- sampling interval 10 μs
- gate separation 75 km
- number of scatter gates 13
- total range 225-1175 km

Scan Cycle
- field-aligned 15 min
- vertical 5 min

Channels 5 and 6 were used to monitor plasma lines. All other channels were used to record the ion line.

Radar Parameters (Block 2)
- Same as CP-3

Scan Cycle
- 20 min elev. scan. 11 points (abbreviated version of CP-3 elev. scan)
  = 28° elev.scan in north-south plane through Tromso and Kiruna

Block 2 run approximately every two hours for background diagnostics. The VHF antenna was pointed vertical throughout the experiment.

Figure 6-5: Radar operating parameters employed in experiment to investigate ERB at EISCAT on November 30. 1990.

Ideally we hoped to obtain simultaneous UHF and VHF measurements for radar cross section measurements at two frequencies.

A 20-minute elevation scan was performed approximately every two hours for diagnosis of background ionospheric parameters. Two plasma line receiver channels were also recorded to deduce ionospheric currents directly. A complete description of the radar parameters and scan cycles employed in the experiment is given in Figure 6-5.

To distinguish the enhanced echoes from actual hard targets we relied on the multi-static capability of the EISCAT UHF system to obtain full 3-D Doppler information. Coherent echoes detected within the common scattering volume which did not exhibit velocities consistent with hard targets could be attributed to geophysical effects. In addition to hard target discrimination, the tri-static system can provide

the aspect angle dependence of the enhanced radar cross section, an important clue to understanding the physics of this phenomenon. To better facilitate the task of acquiring coherent echoes in the common scattering volume, a "smart" real-time radar control program was employed.

This control program, named MONITOR, was written by Anthony van Eyken utilizing an "ERB detection" algorithm developed by Keith Groves and Mike Rietveld. The received ion line spectra were monitored in real-time to detect enhancements. When enhanced spectra were detected, the remote receiving antennas were automatically repositioned to observe the altitude of maximum enhancement along the transmitted radar beam, as depicted in Figure 6-6. This process was usually completed within 10 seconds, considerably less than the time scales over which the echoes can persist (a few tens of seconds). The program was tested by looking at satellites to simulate ERB. An additional valuable feature of MONITOR is the capability to automatically reduce the integration period when enhanced power levels are detected, acquiring high time resolution measurements with adequate signal-to-noise.

Initially, the 30-hour allotment of radar time was scheduled as a single time block beginning at 08:00 UT on November 29, 1990. Because the most promising periods for enhanced echo observations are believed to begin in the early evening and continue into the early morning hours, however, we chose to use only half the allotted time for the first experiment, beginning at 16:00 UT, and save the remaining time for additional observations on the evening of December 1.

From a technical standpoint, the experiment was executed smoothly; unfortunately, it appears that enhanced radar backscatter was not observed. This is undoubtedly due to the lack of appropriate geophysical conditions during the entire observational period. Magnetically, the ionosphere was very quiet: the magnetogram at the Tromsø site showed only weak, gradual variations, and the Ap index for the

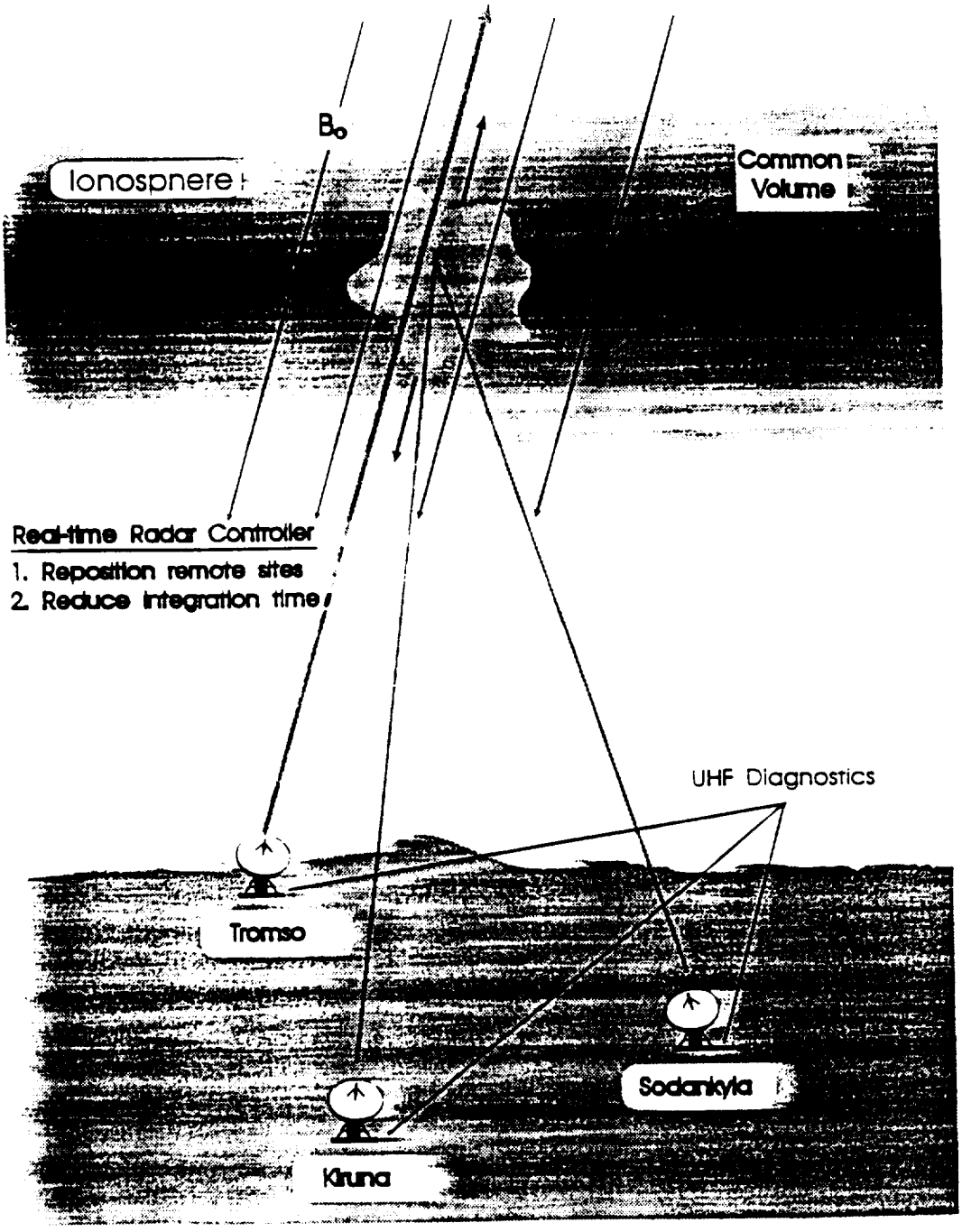

Figure 6-6: Conceptual drawing of the ERB experiment performed at EISCAT in November, 1990. A realtime monitor program was employed to detect and locate ERB; the remote receiving antennas were then repositioned to sample the same volume.

period was a meager five. Also, there was no evidence of particle precipitation, and electron temperatures remained below 3000°K. Additional observing periods were tentatively planned for the evenings of December 1 and 4. On the basis of the latest forecasts for very quiet conditions on both days, however, it was decided not to run dedicated coherent echoes experiments. A search through existing data was believed a more efficient means of locating additional ERB events.

6.1.4 UHF Common Program Data

The computer algorithm used to detect enhanced power spectra in real-time can also be used to analyze existing raw data tapes. Each spectra is checked, and those that exceed predetermined levels of asymmetry and/or overall power enhancement are recorded for later analysis. For these analyses, a 3 dB asymmetry threshold was used to reduce the large number of false detections due to low SNR, even though using the algorithm at this sensitivity level probably results in failure to detect some weak enhancements. I decided to look at CP-2 data initially, hoping to find enhanced UHF echoes in the vertical antenna position which could be compared with the VHF returns from the same scattering volume. CP-2 designates *Common Program 2*, a standard operation mode which includes both field-aligned and vertical radar look-angles. A total of 111 hours of Tromsø CP-2 data and 318 hours of data from the remote sites was reduced and analyzed for additional evidence of enhanced radar backscatter. The actual experiments analyzed are shown in Table 6.1.

Despite the relatively large amount of data analyzed, significant occurrences of ERB were not found. As with the experiment, the probable cause for the lack of enhanced echoes is the low level of magnetic activity present during the time periods analyzed. In addition, only a small volume of space is monitored by the stationary radar beam which requires that ERB processes occur in very specific locations. While

Table 6.1: Table of Analyzed Common Program Experiments. T, K, and S denote Tromsø, Kiruna, and Sodankylä.

STRT. DATE-UT	END DATE-UT	MODE	SITES
87/10/20-09:30	87/10/21-14:00	CP-2-D	K.S
87/10/21-14:00	87/10/22-23:30	CP-2-D	T.K.S
88/08/09-08:00	88/08/10-08:30	CP-2-D	K.S
88/08/16-08:00	88/08/18-23:00	CP-2-D	T.K.S
89/10/23-18:00	89/10/25-14:30	CP-2-D	K.S
89/10/24-17:00	89/10/25-07:30	CP-2-D	T
90/11/27-17:00	90/11/27-18:00	CP-2-D	T

not indicative of all localized auroral processes, the Ap index for magnetic activity does provide an estimate of the general level of magnetic disturbance globally. This index was less than 15 (quiet) on all but one of the nine days investigated, and less than 10 on all but two. These periods were chosen for analysis initially because they were available at the Tromsø site. Later, due to several reasons (primarily computer failure), it was possible to process only half the data originally slated for analysis at EISCAT Headquarters in Kiruna, Sweden. In addition, 24 hours of data processed from disturbed time periods was lost due to a faulty data transfer.

Tromsø Data

About 2.5% of the Tromsø spectra surveyed were determined to be asymmetrically enhanced; more than 95% of the selected spectra are not geophysically significant. Most result from satellites penetrating the radar beam; some are asymmetric because of random noise spikes in low SNR data from high altitudes. Only two cases of interest were found in the data examined thus far.

The first, shown in Figure 6-7, is comprised of enhanced spectra previously found by Mike Rietveld and proves the value of this method of analysis. The data quality for the October 24/25 experiment was quite good, and only 42 spectra were computer-selected from 14 hours of data. Of these 42, 16 are clearly enhanced by geophysical

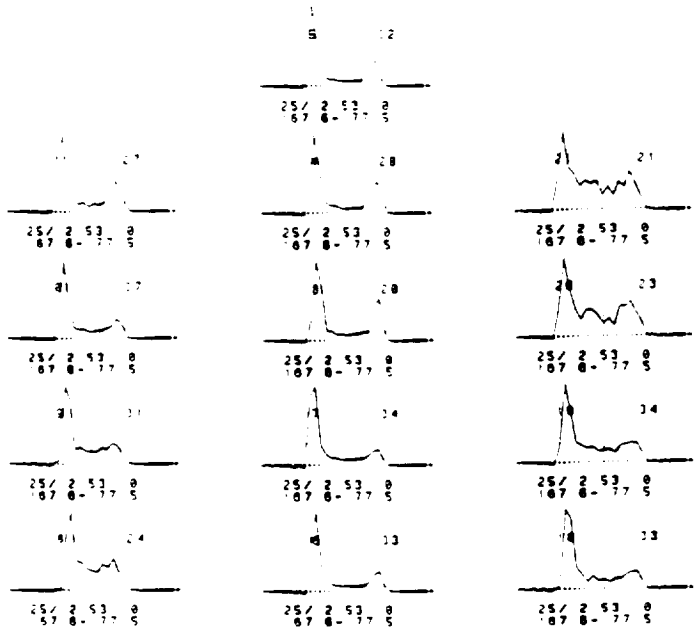

Figure 6-7: Asymmetric enhanced UHF spectra from October 1990 extended over 13 consecutive range gates. The range gate number is on the upper left of each plot; the number on the upper right is the asymmetry index assigned by the MONITOR detection algorithm.

mechanisms as evidenced by their sequential extent in range. This data set is the exception with regard to geomagnetic activity noted above. It was recorded three days after the peak of one of the largest magnetic storms on record. Actual conditions for the day and hour of the enhanced echoes occurrence are characterized by an Ap index of 23 and a 3-hr Kp of 5.

Data from August 18, 1988 form the second interesting case (see Figure 6-8), when weakly enhanced spectra were observed in the UHF radar beam continuously for more than 30 seconds at ranges varying from 520 - 600 km along the magnetic field. The localized nature of the enhancements does allow the possibility that the spectra may be a hard target signature in the beam. Figure 6-9, however, indicates that a satellite at 600 km range could remain in the stationary radar beam for no more than a few seconds, and direct measurements of satellites with the EISCAT system support this

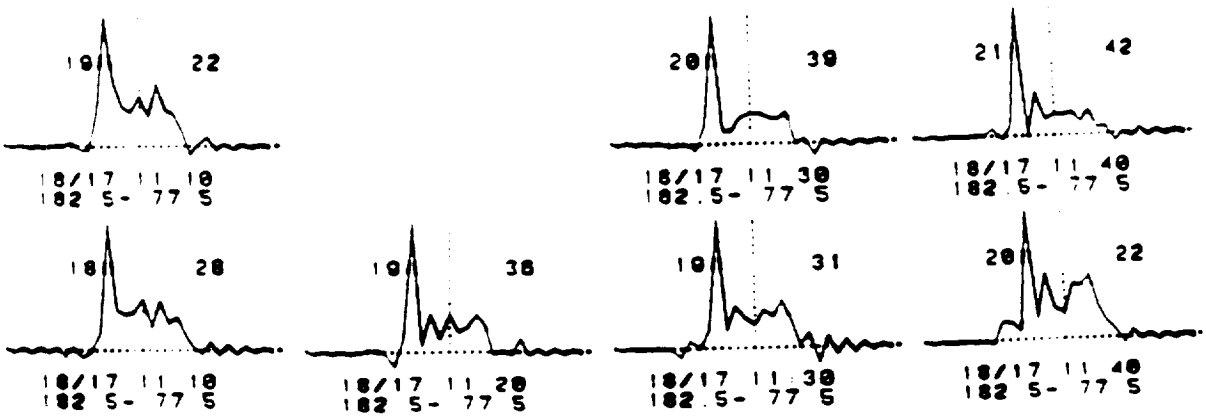

Figure 6-8: Weakly enhanced ion acoustic spectra seen in four consecutive 10-second integration periods. The range varies from 520 km to 600 km; a satellite at this range would pass through the radar beam in less than five seconds.

conclusion.

These spectra were selected by the MONITOR program and represent the interesting data I have from this time period. It is entirely possible that there are other spectra recorded during this time period which, while not detected by MONITOR (and therefore not recorded), contain meaningful levels of asymmetric enhancement.

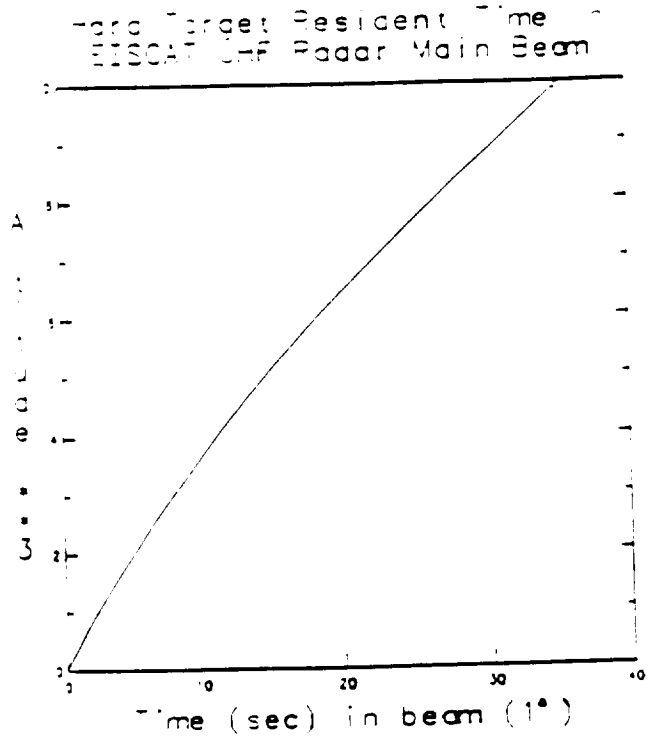

Figure 6-9: Approximate main beam satellite transit time as a function of altitude for the 1° EISCAT UHF radar beam. Targets below 1000 km remain in the beam for less than five seconds. Circular orbits are assumed.

Remote Sites Data

As pointed out previously, enhanced echoes observed by all sites can be conclusively attributed to geophysical sources if they do not exhibit a 3-dimensional Doppler velocity consistent with orbiting bodies. Motivated by the promise of unambiguous classification, a large amount of data from the remote receiving sites at Kiruna and Sodankylä was examined. However, not a single case of ERB was detected by MONITOR in more than 300 hours of remote site data.

The lack of detections is somewhat puzzling, particularly because during the October 24/25 experiment moderately enhanced spectra were observed at Tromsø from the common volume scattering height of 278 km. Unfortunately, the remote sites were not pointed at this altitude during the period of observed ERB: in fact, no coincident measurements of ERB have been discovered thus far. This can be partially explained by the fact that the remote sites monitor altitudes at 278 km or below, where very

few enhancements have been seen.

The aspect angle sensitivity of ERB processes may prove important, as well, because the remote sites are not able to view the F region common scattering volume at small aspect angles. Because the enhancement phenomenon is associated with field-aligned processes, it is possible that it produces a much weaker signature when diagnosed by the remote sites at large aspect angles. A final consideration is that the scattering volume available to the remote sites is determined by the intersection of their receiving antenna beam and the radar beam transmitted from Tromsø. The respective radar beams are only about five kilometers in diameter at the intersection altitude of 275 km. This provides a relatively small scattering volume, and the power received by the remote sites is considerably less than that received from direct backscatter at Tromsø. Nevertheless, the continuing effort to find more cases of ERB in the EISCAT data will probably uncover some events diagnosed simultaneously by both the Tromsø receiver and the remote sites, providing new insights into the physics of these events as discussed in Chapter 7.

6.1.5 EISCAT VHF Observations of ERB

Evidence of ERB events detected with the EISCAT VHF radar were recently reported by *Collis et al.*, [1991] (henceforth, COLL91). The enhanced spectra are similar in appearance to those recorded by the UHF radar discussed previously. A summary of their characteristics follows.

Summary of VHF Observations

VHF ERB was observed during experiments in January 1989 and February 1990 [COLL91]. Both cases were associated with unusually strong visible red aurora as indicated by all-sky imagers and scanning photometers. The auroral signatures are

believed to be caused by low energy ($E \leq 100$ eV) precipitating electrons. A sample of the VHF echoes is shown in Figure 6-10, where the altitude variation of the enhancements over a three minute period in the February experiment is evident.

The apparent downward motion of the ERB is interpreted by COLL91 to represent the equatorward motion of a field-aligned structure (*e.g.*, auroral arc) passing over the radar. The VHF echoes shown in Figure 6-10 are not extended in range because the antenna is pointed to the zenith, rather than field-aligned as in the case of the UHF enhancements. Further consideration of the data indicates other differences between the VHF and UHF enhancements. The VHF events are found at much higher altitudes (up to 1350 km) and persist for much longer, up to four minutes in the example shown here. In the February 1990 experiment VLF spectra were enhanced sporadically for more than one hour. By comparison, UHF events at EISCAT have not been found above 600 km, and 50 seconds represents the longest period of uninterrupted enhancement, while the duration of sporadic enhancement periods does not exceed about ten minutes. These facts indicate that the enhancements may be more easily excited at VHF frequencies [COLL91].

The frequency shift of the enhanced peak was seen to change from upshifted to downshifted during the course of about a minute in the January 1989 experiment. ERB data acquired during the February 1990 event, however, are characterized by a consistent dominant enhancement of the downshifted peak for up to four minutes, though at times both peaks were enhanced in the same integration period. This is in contrast to the UHF measurements where the asymmetry seems to fluctuate more rapidly in both time and space between downshifted and upshifted frequencies.

The total cross section enhancement for the VHF spectra ranges from factors of 4–5 during the January experiment to greater than 25 in the February events. Measurements of ERB by both the UHF and VHF radars have been recorded during

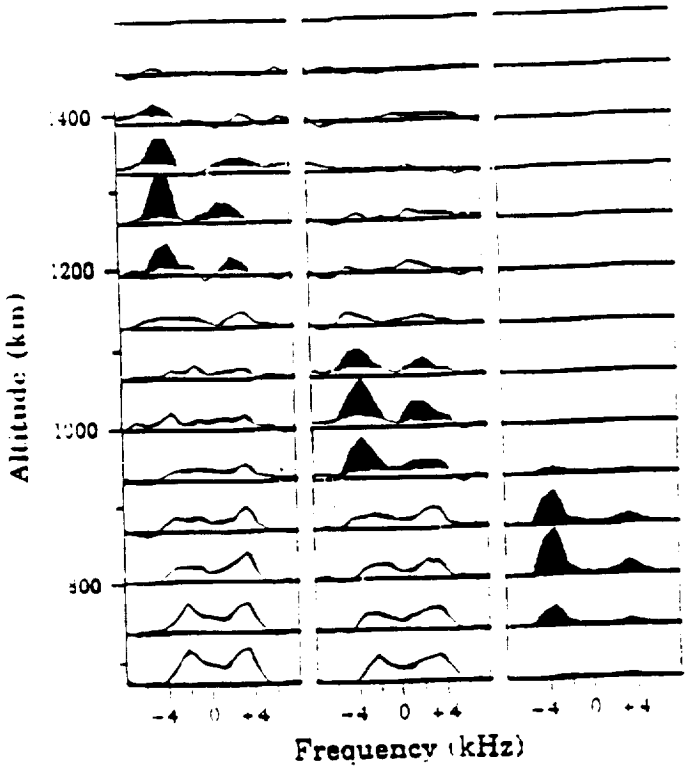

Figure 6-10: Enhanced zenith VHF spectra from 20 February, 1990. The three 10-second integrations shown were recorded 1 minute apart beginning at 18:03:00 UT; the altitude of the enhancement varies smoothly. Enhancements above normal incoherent scatter are shaded black [after COLL91].

the same time period, confirming that both are associated with elevated electron temperatures, large magnetic field fluctuations, and, when optical data is available, with red aurora. Unfortunately, comparisons of simultaneous UHF/VHF spectra from the same scattering volume have not been reported. This is because the VHF antenna is nearly always pointed vertical during experiments, while the UHF dish acquires data at other look-angles a majority of the observing time. The comparison of spectral characteristics at two frequencies would provide important information on the scale size dependence of the physical mechanism responsible for the ERB.

6.2 ERB Observations at Sondreström

The incoherent radar located at Sondreströmfjord, Greenland operates at 1290 MHz and offers an ideal location (≈74° Inv.lat.) for the excitation and detection of ERB at

a wavelength shorter than that of both the EISCAT and Millstone Hill systems. The data base available for such studies is, at present, much more limited than either of the latter sites. Frequent low energy electron precipitation occurring at this latitude increases the likelihood of backscatter enhancements locally.

6.2.1 Zenith Experiments at Sondrestöm

As explained previously, acquiring data with the radar antenna pointed to zenith effectively filters out hard target contamination by limiting the line-of-sight velocity to subsonic magnitudes. Accordingly, attempts to identify ERB events at Sondreström have employed this approach.

Analysis of four hours of zenith data taken in August, 1988 revealed that two of the 20 coherent echoes observed occurred at frequency shifts corresponding to ion acoustic waves; the remainder of the enhanced peaks had essentially no Doppler shift and are presumed to be caused by hard targets passing through the radar beam. The two events at the ion acoustic frequency showed backscattered power enhanced by factors of 2 and 5, respectively; smaller asymmetries were evident in several other spectra. The spectrum enhanced by a factor of 5 is shown in Figure 6-11. The range gates shown in the figure do not overlap, so that a localized target appears in only one gate. This is consistent with EISCAT and Millstone Hill observations of ERB for nonzero aspect angles.

Six more zenith experiments were run at Sondreström in May, September, and October, 1989 and October, 1990 providing 44 additional hours of observations. These data, however, show little evidence of ERB at ion acoustic frequencies; asymmetric enhancements are at most 1.5 times greater than the normal background spectra, not considered statistically significant. No extended periods of ERB occurrence have been found in Sondreström data yet. The lack of ion acoustic ERB in these ex-

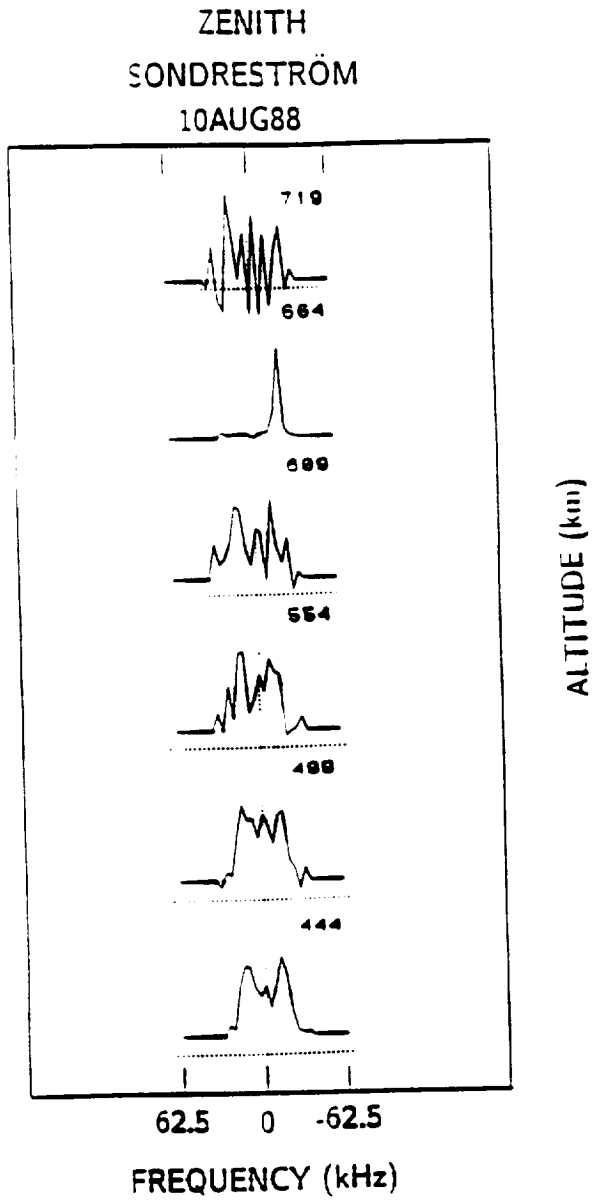

Figure 6-11: Sondreström zenith data showing factor of 5 enhancement in ion acoustic spectrum. Altitude scale is in kilometers.

periments suggests the absence of intense field-aligned currents. The magnitude of these currents is related to the level of geomagnetic activity, generally weak during these experiments. Another reason for the absence of geophysical ERB may be that higher electron drifts are required for enhancement at the short wavelength (12 cm) diagnosed by the Sondrestrom radar.

6.3 Summary of ERB from Other Sites

Important progress has been achieved towards identifying and understanding enhanced radar backscatter from the ionosphere. Such events are known to occur briefly and infrequently under special ionospheric conditions: enhancements below 250 km are especially rare. The most prominent observations reported by RD91 and COLL91 associate ERB events with red aurora (*viz.*, particle precipitation), large magnetic field variations locally, and elevated electron temperatures. These requirements are also reflected by global magnetic indices for the periods indicating very disturbed conditions. The EISCAT ERB observations have been seen when Kp$\geq$ 5, a level of disturbance occurring about five percent of the time during solar max [*Mayaud*, 1980]. Comparing the Millstone Hill, EISCAT and Sondrestrom observations suggests that ion acoustic spectra may be enhanced over a wide range of scale sizes; enhancement thresholds appear to decrease with increasing wavelength.

These findings are basically consistent with the current driven source mechanisms of Kindel and Kennel [1971] and Rosenbluth and Rostoker [1962] suggested by FOS88, RD91, and COLL91. These mechanisms show that a relative drift between the electrons and the ions (*i.e.*, a current) in the plasma will produce asymmetric enhancements in the observed ion acoustic spectrum. The frequency shift of the asymmetry depends on whether the electrons are drifting towards (upshift) the radar or away (downshift) from the radar. A puzzling inconsistency with the known mechanisms,

however, stems from the commonly observed simultaneous enhancement of both up-shifted and downshifted ion acoustic peaks. The magnitude of enhancements larger than 7 dB and the detection of ERB at nonzero aspect angles are also not described adequately by RR and KK. Possible explanations for these observations based on existing theories and an alternative mechanism for ion acoustic enhancements are presented in Chapter 7.

Chapter 7

Enhanced Radar Backscatter (ERB) Theory

This chapter describes the application and evaluation of theoretical models to explain the observations of ion acoustic ERB described in Chapters 5 and 6.

In section 7.1, the current driven processes first reported by Rosenbluth and Rostoker [1962] and Kindel and Kinnel [1971] are applied to the ERB observations. These theories can explain general features of the data, but require current densities much greater than have been previously measured on satellites (>1 amp/m^2). Furthermore, they are not able to adequately describe the magnitude of ion acoustic enhancements larger than about 7 dB ($\sim 5 \times 10^{-17} m^2/m^3$), the commonly observed symmetric enhancement of upshifted and downshifted wave modes, and the detection of ERB at nonzero aspect angles with respect to the geomagnetic field.

Section 7.2 describes the new application of a mechanism predicting the amplification of ion acoustic waves through the nonlinear coupling of intense Langmuir waves. This idea was originally proposed by Lee [1981] to explain the enhancement of ion lines in heating experiments at Arecibo Observatory, where the HF heater was the source on Langmuir wave turbulence near the heater wave reflection height. In my

investigation of this mechanism, the intense Langmuir waves are excited by the large suprathermal electron population associated with field-aligned currents and auroral arcs. The investigation of a new explanation is warranted because of the inadequacies of existing theories mentioned above, and the realization that the suprathermal electrons' wave-particle interaction with the background plasma represents an additional source of free energy for ion acoustic wave enhancement.

Section 7.3 contains a discussion of the various theories with regard to the observations of Chapters 5 and 6. The nonlinear coupling mechanism predicts both the magnitude and the shape of many of the observed enhancements. Furthermore, it can contribute to ion acoustic enhancements in conjunction with other current driven mechanisms.

7.1 Application of Existing Current Driven Theories

A limited number of theoretical investigations of ion acoustic wave enhancements have been conducted, but two prominent sources considering the topic exist in the literature. The processes investigated by Rosenbluth and Rostoker [1962] for marginally stable plasmas and Kindel and Kennel [1971] for plasma instabilities are potential mechanisms whereby ion acoustic waves are amplified by large electron drifts relative to the ions. The implications of these theories with regard to observed enhancements is discussed below.

7.1.1 Ion acoustic enhancements in a stable plasma

The spectral shape of high frequency ($\omega >> \omega_p$) radiation scattered from a plasma was discussed in Chapter 5 and the references therein; the effects of electron and ion

temperature, density, composition, and bulk drift velocity on the spectra were briefly described. This work was extended by Rosenbluth and Rostoker (henceforth, RR) and Lamb in 1962 to include the effects of a *relative* drift between the electrons and ions on the shape of the scattered wave spectrum. Such a drift, of course, corresponds to a current flowing in the plasma. The basic approach was to modify the linear dielectric function used previously by simply replacing the usual electron Maxwellian distribution function, $f_e(\mathrm{v})$ with a *drifting* Maxwellian distribution.

$$\begin{aligned} f_e(\mathrm{v}) &= \left(\frac{m_e}{2\pi E_{th}}\right)^{\frac{3}{2}} \exp\left[-\frac{m_e \mathrm{v}^2}{2E_{th}}\right] \\ &\Rightarrow \left(\frac{m_e}{2\pi E_{th}}\right)^{\frac{3}{2}} \exp\left[-\frac{m_e(\mathrm{v}+\hat{e}U)^2}{2E_{th}}\right] \end{aligned} \tag{7.1}$$

Here m_e, E_{th}, and $\hat{e}U$ correspond to the electron mass, electron thermal energy, and drift velocity, respectively. The assumed direction of the drift velocity relative to the incident (k_i) and reflected (k_r) radar waves is shown in Figure 7-1. The effects on the ion line spectrum are shown in Figures 7-2 and 7-3, where the power spectra for different drift velocities (normalized by the electron thermal velocity) and different electron-to-ion temperature ratios ($T_e/T_i \equiv T_r$) are plotted on a logarithmic scale.

The obvious asymmetries in the ion line enhancements depend directly on the magnitude of the electron drift, approaching infinity for increasing values of y. Mathematically, this means that a singularity in the cross section (zero in dielectric function, $\sigma(\omega) \propto |\epsilon|^{-2}$) exists for sufficiently large values of y; physically, the singularity corresponds to the onset of an instability, and the linear analysis is no longer applicable. The instability threshold drift velocity is very sensitive to T_r, decreasing by more than an order of magnitude as T_r varies from 1 to 5. Even though the spectral asymmetry may be more easily stimulated with increasing T_r, the overall cross section enhancement under these conditions decreases.

Physically the RR enhancements can be understood by recalling the ion line scattering mechanism in the no–drift case. The spectral shape is then determined by

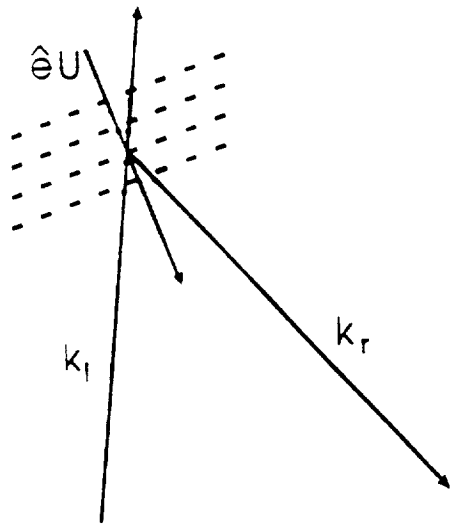

Figure 7-1: Assumed direction of electron drift, $\hat{e}U$, relative to incident and reflected radio waves in the RR mechanism. The drift is perpendicular to the planes of reflection indicated by the dashed lines.

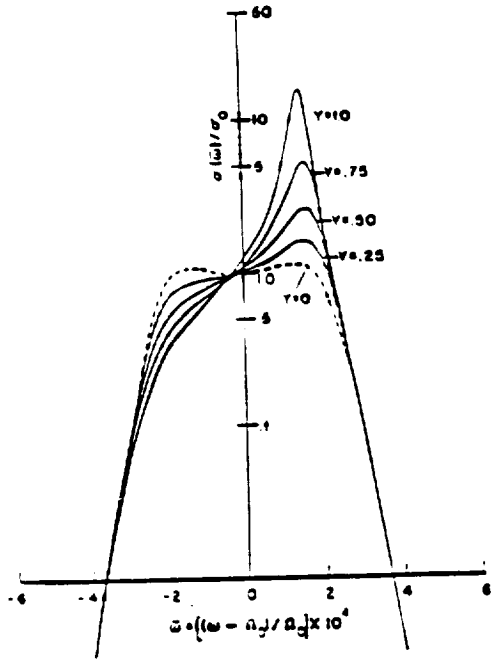

Figure 7-2: Differential scattering cross section for a plasma with electron drift, $y = U/v_{te}$; $T_e = T_i$ [after RR].

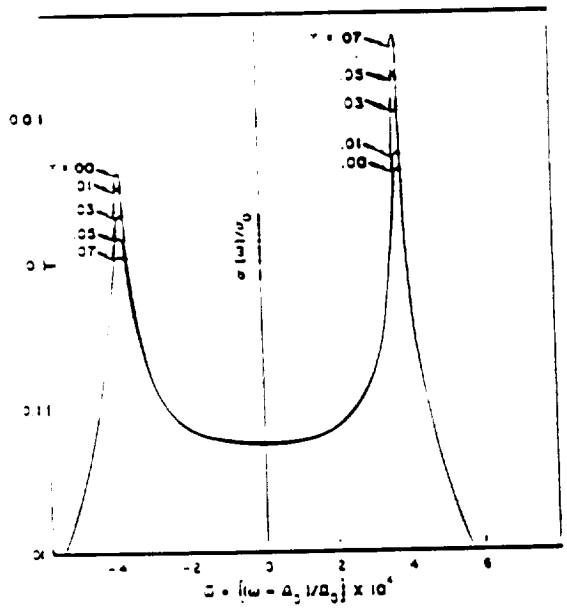

Figure 7-3: Differential scattering cross section for a plasma with electron drift, $y = U/v_{te}$; $T_e = 5T_i$ [after RR].

scattering from electrons shielding thermal density fluctuations propagated by the relatively massive ions in the form of electrostatic acoustic waves. When a drift is introduced by shifting the entire Gaussian electron distribution function in velocity space, there are more electrons available to shield density fluctuations travelling in the direction of the velocity shift and correspondingly fewer in the opposite direction. This explanation is also consistent with the observation that the enhancement of one side of the spectrum is accompanied by a reduction of power in the neighboring hump.

7.1.2 Ion acoustic enhancements via instability

Whereas the mechanism discussed in the previous section applies for a (marginally) stable plasma, Kindel and Kinnel [1971] (henceforth, KK) developed the theory of current driven instabilities in the topside ionosphere when the electron drift velocity exceeds the critical threshold velocity. The physical reason for the instability is that when the electron drift velocity exceeds the phase velocity of ion waves in the plasma, the waves are able to draw energy from the streaming electrons via a collisionless

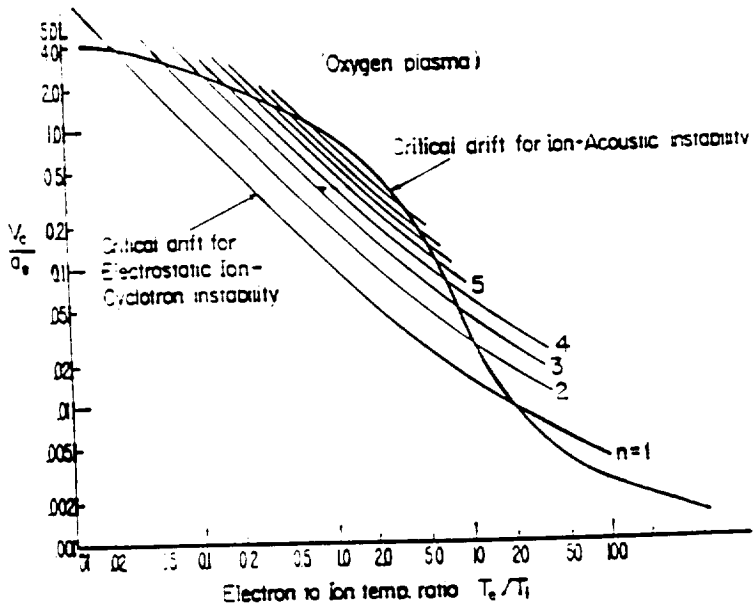

Figure 7-4: Critical drift velocity normalized by the electron thermal speed as a function of T_e/T_i for an O^+ plasma. The threshold is lower for ion cyclotron waves over a wide range of temperature ratios (after KK).

damping process known as Landau damping.

An important result of KK's calculations is that the ion cyclotron wave modes require a lower threshold drift velocity for instability than ion acoustic waves for values of $T_r < 20$, as shown in Figure 7-4. Typical values for T_r in the ionosphere are less than five. As was the case with the RR process, the critical velocity is very sensitive to T_r. This is because the growth of the ion acoustic wave is balanced by ion Landau damping. When $T_r \simeq 1$, the damping is heavy and the drift velocity must exceed the electron thermal speed to produce instability. As T_r increases, however, the phase velocity of the ion acoustic waves increases as well; when the phase velocity of the ion waves exceeds the ion thermal velocity, the Landau damping of those waves is much weaker, and the required drift speeds are correspondingly smaller.

Using typical ionospheric profiles for density and composition, and assuming bulk electron charge carriers, KK cast the critical drift velocity calculation into a critical "electron flux" (i.e., current) calculation for a range of altitudes, as shown in Figure 7-5. Modest values of T_r were assumed in the figure, and the flux required to excite

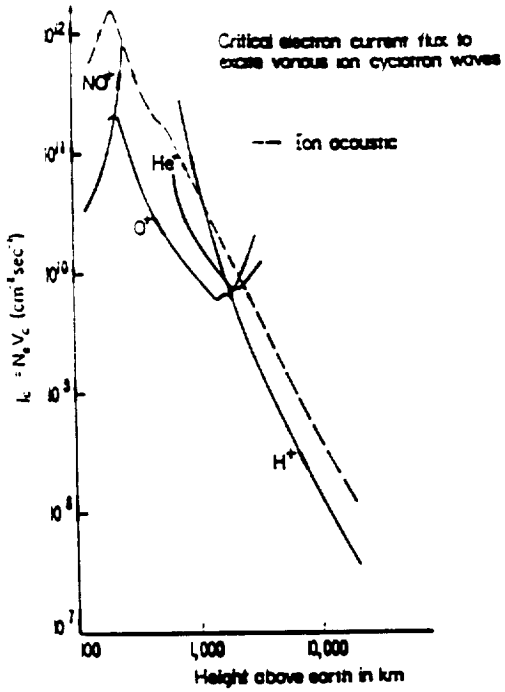

Figure 7-5: Critical electron current flux for instability as a function of altitude for $T_e/T_i \simeq 1$. At every altitude, the threshold for ion acoustic waves exceeds that of cyclotron modes [after KK].

ion acoustic waves is quite high; for reference, the typical background electron flux in the ionosphere is about $2 \times 10^8\ cm^{-2}sec^{-1}$, and the largest localized flux reported in the literature is $6 \times 10^{10}\ cm^{-2}sec^{-1}$ [*Bythrow, et al.*, 1984].

Comparing these numbers with Figure 7-5, the excitation of ion acoustic waves in the ionosphere does not appear likely. However, the curves plotted in the figure are for $T_r \simeq 1$ and an assumed typical density profile. Both parameters have a marked effect on the flux threshold: T_r for the reasons given above, and density because the parameter relevant to the instability is velocity, not flux. Lower densities require higher velocities to deliver the same flux. Applications of KK's results to the real ionosphere should consider these points carefully.

7.2 Nonlinear Mode Coupling Theory of ERB

Presented here is a theoretical investigation of a new mechanism which can enhance radar backscatter in conjunction with known current driven processes, thereby re-

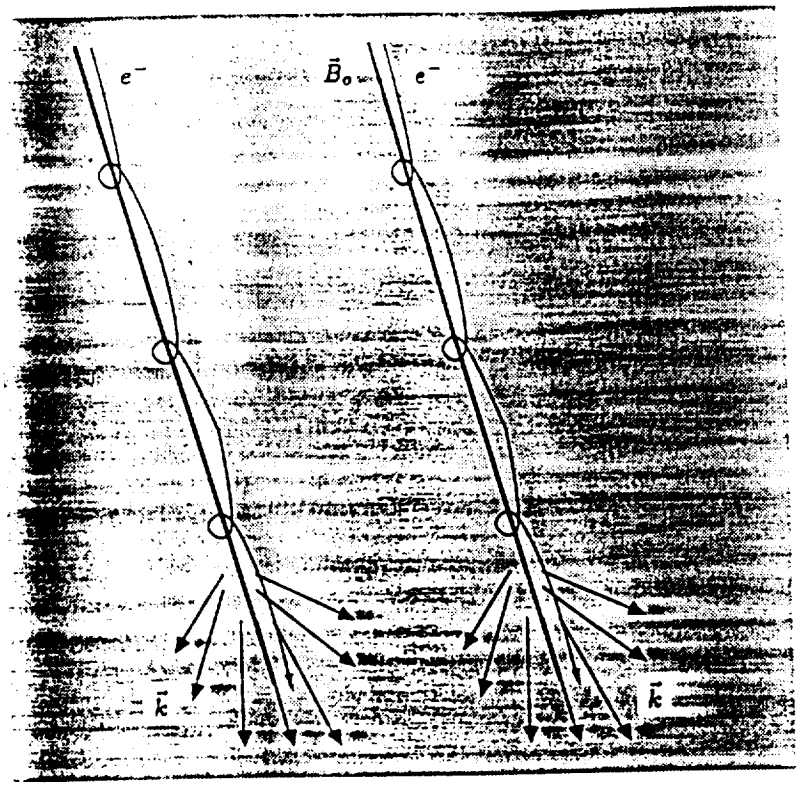

Figure 7-6: Electrons streaming down the magnetic field lines excite a spectrum of intense Langmuir waves. These high frequency waves then couple to drive low frequency ion acoustic waves in the plasma

ducing the threshold amplitudes of the current densities they require. The proposed scenario is as follows. Energetic electrons associated with intense current filaments in the ionosphere excite a suprathermal spectrum of Langmuir waves as they stream through the background plasma. Subsequently the Langmuir waves can become nonlinearly coupled via the ponderomotive force to induce low frequency density perturbations driving ion acoustic waves in the ionospheric plasmas, as described by Lee [1981]. The physics of the proposed mechanism is illustrated conceptually in Figure 7-6.

7.2.1 Intense Langmuir Wave Generation

Because of large Landau damping by bulk electrons, a plasma at or near thermal equilibrium exhibits only very weak electron plasma oscillations (Langmuir waves).

If the electron distribution function has a nonthermal, high energy tail, however, it is possible for the fast electrons to resonantly excite intense Langmuir waves with large phase velocities which are weakly damped [*Pines and Bohm*, 1952]. The intensity, I_p of radiation scattered by these plasma waves in a collisional plasma was first calculated by Perkins and Salpeter [1965], and can be expressed as [*Yngvesson and Perkins*, 1968],

$$I_p = \frac{2\pi K T_p(v_\phi)}{\lambda^2 n e^2} = \frac{T_p(v_\phi)}{2\alpha^2 T} \tag{7.2}$$

The second expression for I_p in equation (7.2) takes the form of an effective temperature of the plasma due to suprathermal electrons normalized by the background temperature. The spectrum of enhanced Langmuir waves in the presence of suprathermal electrons can be calculated by evaluating this normalized velocity dependent plasma temperature T_p,

$$\frac{T_p(v_\phi)}{T} = \frac{f_m(v_\phi) + f_p(v_\phi) + \chi}{f_m(v_\phi) - KT\frac{d}{dE_\phi} f_p(v_\phi) + \chi} \tag{7.3}$$

where f_m and f_p represent, respectively, the Maxwellian and photoelectron contributions to the one-dimensional velocity distribution. They are given by

$$f_m = n\left(\frac{m}{2\pi KT}\right)^{1/2} \sum_{n=-\infty}^{\infty} \frac{e^{-b\sin^2\theta}}{\cos\theta} I_n(b\sin^2\theta) e^{-\left[\frac{(y-n)^2}{2b\cos^2\theta}\right]} \tag{7.4}$$

$$f_p = \int_{E_\phi}^{\infty} \left(\frac{m}{8E}\right)^{1/2} \rho(E)\, dE \tag{7.5}$$

The quantity χ in (7.3) describes the excitation and damping of plasma waves by electron-ion collisions and has the following expression:

$$\chi = \frac{32\pi}{3\lambda^3}\left(\frac{m}{2\pi KT}\right)^{1/2} \ln[4\pi n D^3] \tag{7.6}$$

The parameters in (7.4)–(7.6) are defined by $y = \omega_p/\omega_c$, $b = k^2a^2/2$, and $a = \omega_c^{-1}\sqrt{2KT/m}$; n, T, k, θ, denote the electron density, electron temperature, wave number associated with the backscatter geometry, and the angle between the radar beam and the earth's magnetic field, respectively. I_n represents a Bessel function

of the first kind of imaginary argument. The Maxwellian contribution described by equation (7.4) is complicated by the presence of the magnetic field which introduces a strong aspect angle sensitivity in the collisionless damping rate [*Salpeter*, 1961]. Evaluation of four or five terms of the sum in (7.4) provides good accuracy.

The density of particles per unit volume-energy is given by $\rho(E)$; this parameter is derived from satellite data for the quantitative analysis presented in Section 7.2.3. When $\rho(E)$ is sufficiently large at high energies, a spectrum of enhanced Langmuir waves will be excited near the plasma frequency. Radar observations of these waves, the so-called *plasma line*, have been used to estimate the flux of nonthermal electrons generated by solar radiation [e.g., *Yngvesson and Perkins*, 1968; *Cicerone and Bowhill*, 1971; *Abreu and Carlson*, 1977].

7.2.2 Nonlinear Langmuir Wave Coupling

These Langmuir waves can become a potential source for generating ion acoustic waves through nonlinear coupling via the ponderomotive force according to theory [*Lee*, 1981]. The ponderomotive force induces low frequency ($\omega = \omega_1 - \omega_2$) density perturbations, δn, with the form

$$\delta_n = n_o \frac{\mathrm{F} \cdot (\mathrm{k}_1 - \mathrm{k}_2)\sigma_e\sigma_i}{e^2(\omega_1 - \omega_2)(\sigma_e + \sigma_i)} \tag{7.7}$$

where F represents the ponderomotive force, (ω_1, k_1) and (ω_2, k_2) represent two high frequency Langmuir waves, and σ_e and σ_i are the electrical conductivities for electrons and ions, respectively. The scattering cross-section of these low-frequency density perturbations can be expressed as

$$\sigma_s(\omega_o + \omega)d\omega = \frac{\sigma_T < |\delta_n(k,\omega)|^2 >}{2\pi V_L t_L} d\omega \tag{7.8}$$

where $<| \delta_n(k,\omega) |^2>$ is the power spectrum of the density perturbations, σ_T is the Thomson differential cross-section, V_L is a very large volume and t_L is a very long

time interval. If the enhanced Langmuir waves are characterized by a spectral density $W(\mathbf{k}_1)$, the expression (7.8) can be written as

$$\sigma_s(\omega_o + \omega) = \gamma k^{-1} \int \int W(\mathbf{k}_1) W(\mathbf{k}_1 - \mathbf{k}_2)\, d\mathbf{k}_1 \tag{7.9}$$

where γ is a parameter to be determined by the characteristics of ionospheric plasmas and the detailed nonlinear mode coupling process.

7.2.3 Analysis with Regard to ERB

The velocity dependent temperature, T_p, expressed by (7.3) represents the enhancement of the Langmuir wave power relative to the weak thermal level power as a function of phase velocity (v_ϕ) and aspect angle (θ); its value depends on three primary parameters, f_m, f_p and χ. Of these three, f_m and χ are determined by the background ionospheric parameters typically associated with observed geophysical ERB events, given by $T = 2000°$ K, $\omega_p/2\pi = 2.8$ MHz, and $\omega_c/2\pi = 1.1$ MHz. As previously stated, f_m represents the Maxwellian contribution to the one-dimensional electron distribution function and vanishes for velocities much larger than the electron thermal velocity ($v_\phi \gg v_{th}$).

At such large velocities, the ratio in (7.3) is usually dominated by the electron-ion collision term, χ, and T_p remains equal to the usual electron temperature, T. If, however, the photoelectron (suprathermal) contribution to the distribution function, f_p, is sufficiently large and its derivative sufficiently small at a given energy, T_p may be many times greater than T, indicating the resonant excitation of intense electron plasma waves. These plasma waves may then couple nonlinearly to drive ion acoustic waves as described in the previous section.

The quantities used to derive $f_p(E)$ in this calculation are from electron flux measurements made aboard the DMSP-F8 satellite (31 eV - 31 keV) and the DE-2 satellite (5 eV - 31 eV) (*W. Denig*, private communication, 1990; *J. D. Winningham*,

private communication, 1987); these data are shown in Figure 7-7a and 7-7b. The electron flux data used are representative of relatively intense auroral arc events observed at high latitudes. The ion flux data from DMSP shows no signature at the time period (see arrow) where the low energy electron flux intensity peaks, indicating that the electrons are carrying significant currents. The resulting values for $\rho(E)$ were then extrapolated linearly down to 1 eV and integrated to give the one-dimensional distribution function along the magnetic field, f_p. Figure 7-8 shows the derived f_m and f_p as a function of particle velocity used to calculate the spectrum of excited Langmuir waves via equation (7.3).

The results of the excited Langmuir wave spectrum are plotted in Figure 7-9. The composite electron distribution function used to calculate the spectrum has been assumed to be one-dimensional along the magnetic field line. As might be expected, for electron energies below about 10 eV, the excited Langmuir wave spectrum is highly field-aligned due to the strong magnetic field dependence of the Landau damping; at higher energies (corresponding to the smaller wavenumbers in Figure 7-9), however, wave phase speeds are sufficiently large to support propagation with relatively weak damping at all aspect angles. To estimate the magnitude of the relative radar cross section enhancement of the ion acoustic fluctuations, a quantity $T_p' \propto W(\mathbf{k}_1)W(\mathbf{k}_1 - \mathbf{k}_2)$, the integrand in (7.9), was calculated; the results are displayed in Figure 7-10. KZ and KY represent the ion acoustic wave vectors parallel and perpendicular to the magnetic field, respectively. The plot shows substantial ion acoustic wave enhancement over a wide range of wavenumbers, with the most intense amplification occurring for wavenumbers less than ten. This is not surprising because smaller wavenumbers correspond to higher energy particles which completely dominate the Maxwellian term in (7.3) at energies much greater than the thermal energy, KT. For the backscatter wave number at which Millstone's 440 MHz incoherent scat-

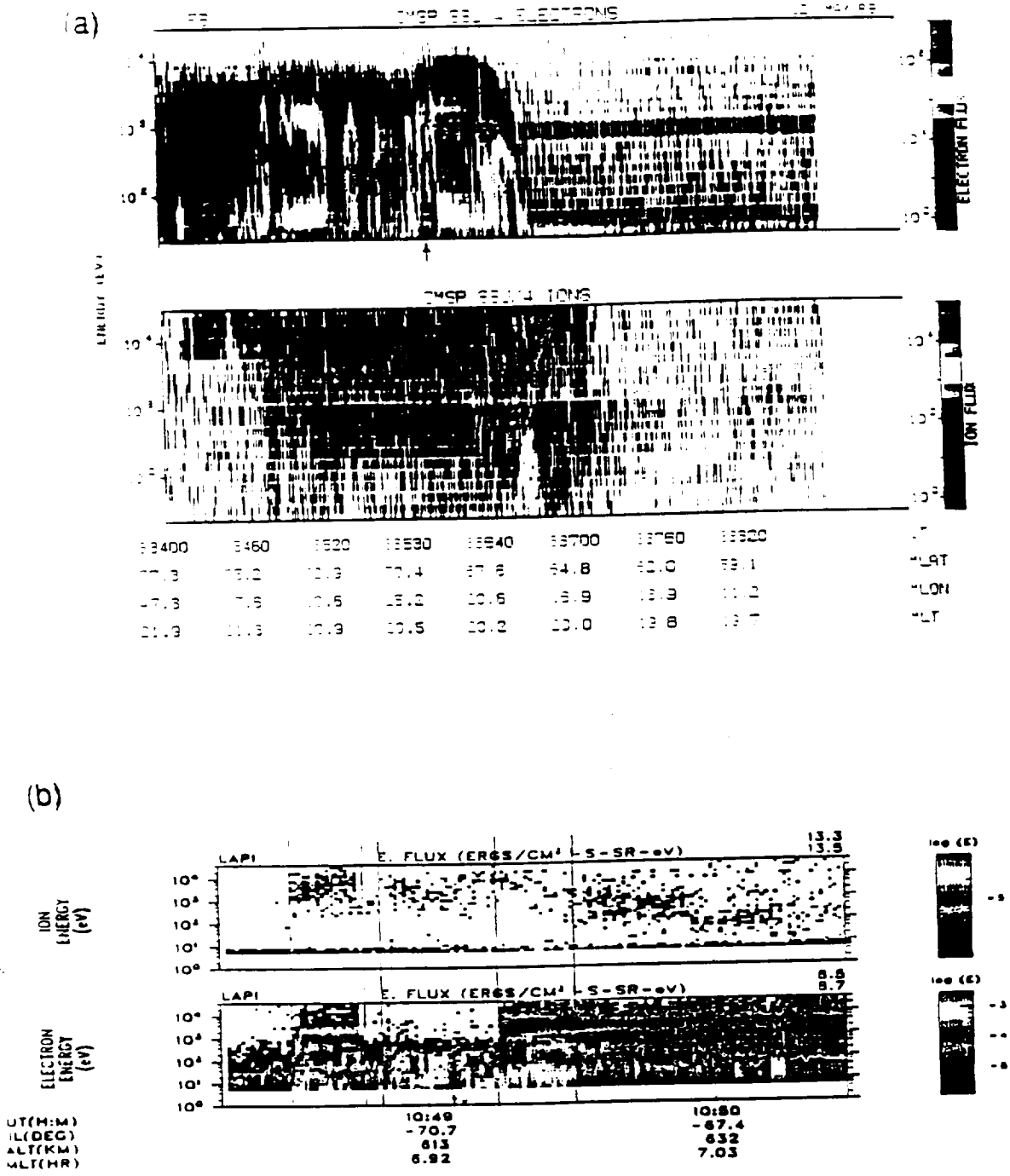

Figure 7-7: Electron spectrograms used to calculate Langmuir wave spectrum: a) electron energy spectrogram from DMSP–F8 and b) electron energy flux from DE–2. The small arrows indicate the time period used for the Langmuir wave spectrum.

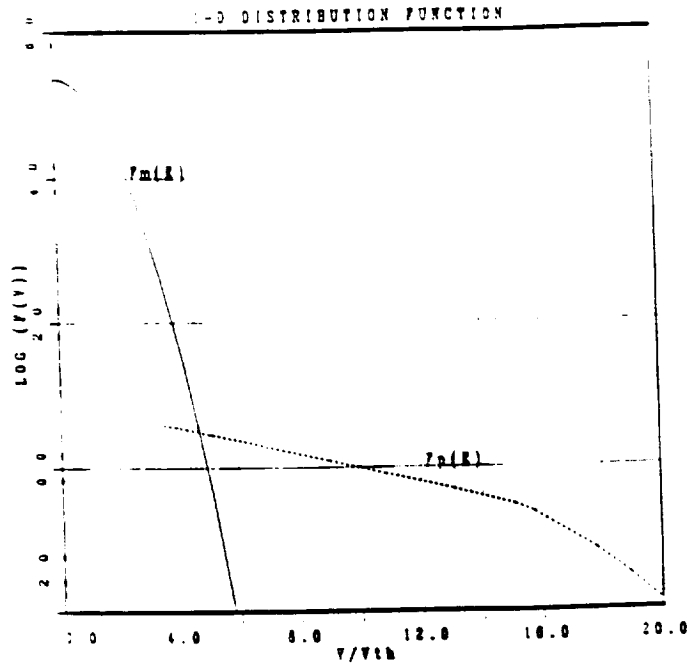

Figure 7-8: The 1-D electron distribution function used to calculate the enhanced Langmuir wave spectrum. The ordinate is in units of m^{-4}sec, while the abscissa is normalized by the electron thermal velocity, V_{te}.

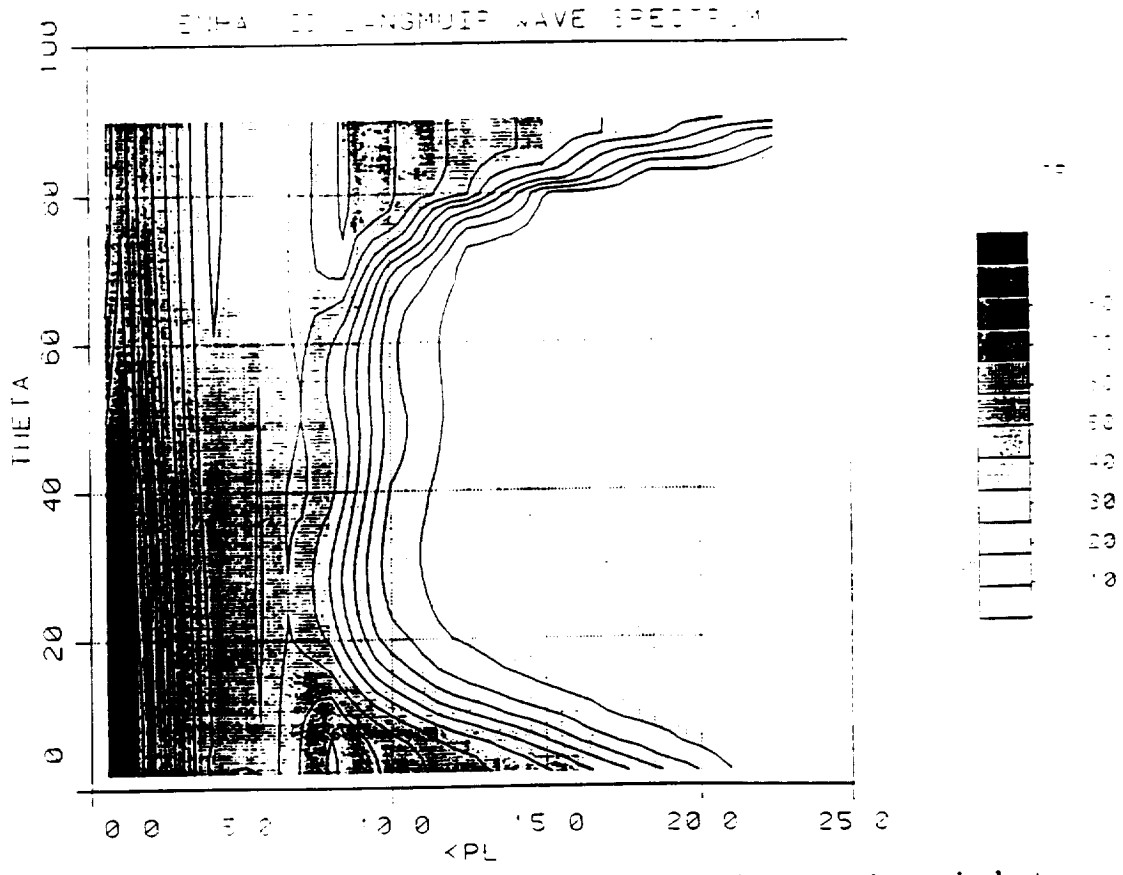

Figure 7-9: Spectrum of Langmuir waves excited by suprathermal electrons as a function of K, wavenumber, and θ, aspect angle with respect to the geomagnetic field.

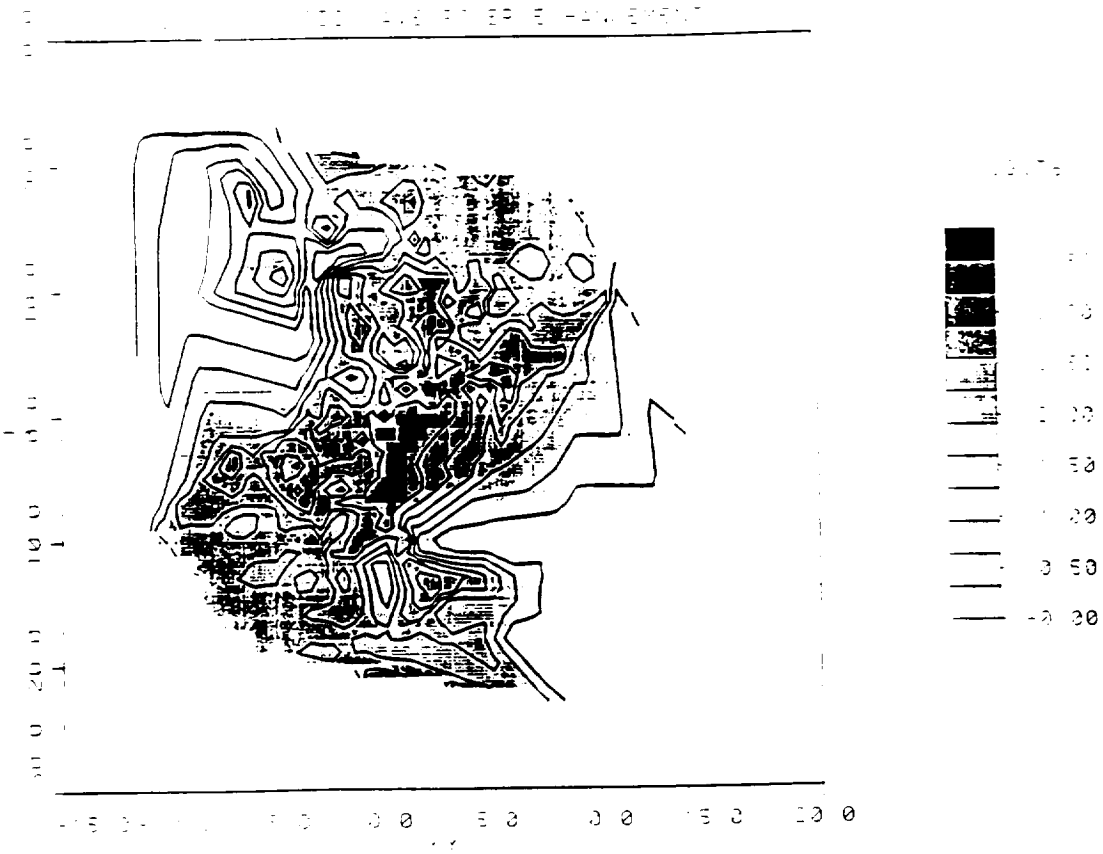

Figure 7-10: Enhancement of ion acoustic wave modes as a function of parallel (KZ) and perpendicular (KY) wavenumbers.

ter radar is sensitive, $k \sim 18.5$ m^{-1}, up to two orders of magnitude enhancement are predicted depending on the aspect angle of the wave mode ($\theta = \tan^{-1}$[KZ/KY]). Up to three orders of magnitude enhancement are possible for wave numbers of ~ 9 m^{-1}, corresponding to a radar frequency of 224 MHz. No enhancement is predicted at wavenumbers exceeding 20 m-1 in this calculation because the assumed flux of low energy electrons ($\leq$ 10 eV) was too small. The theory predicts increasing enhancements for longer wavelengths.

The predicted enhancement of wave modes with large aspect angles relative to the magnetic field was somewhat unexpected because the suprathermal electron distribution used in the calculation was assumed to be field-aligned. This is partly due to the fact that the highest energy electrons excite Langmuir waves at all aspect angles as mentioned previously, and partly because T_p' is derived from a product of two Langmuir wave modes whose difference frequency and wave vector match those

of ion acoustic modes. Considering all possible combinations of appropriate modes one finds it is possible for the field-aligned electrons to couple energy through the Langmuir waves into a broad spectrum of ion acoustic modes. In addition, the ion acoustic wave spectrum is simultaneously enhanced in both downward and upward directions along the field line.

The enhanced spectrum of Langmuir waves shown here may actually be conservative. Larger amplification of such waves has been measured on rockets in auroral arcs [*Ergun*, 1989; *McFadden, et al.*, 1986]. However, these measurements are made with fixed length booms, sampling a single scale size corresponding to the length of the boom, typically a few meters. These relatively long wavelengths are excited by very high energy particles and do not contribute significantly to the enhancement of ion acoustic modes detectable with radars. It is not clear that the enhanced intensities observed at long wavelengths can be extrapolated to the radar wavelength regime.

Suprathermal electron source

The suprathermal particles which act as the driving source for this mechanism are generally associated with field-aligned currents at auroral latitudes. Field-aligned currents in the ionosphere are usually driven by a significant electric potential drop parallel to the magnetic field in the magnetosphere, which accelerates electrons down the field lines into the ionosphere. Recent satellite observations, however, indicate that strong field-aligned currents are sometimes associated only with suprathermal electron bursts in the absence of a significant parallel potential drop [*Marshall, et al.*, 1991; *Johnstone and Winningham*, 1982]. Rocket measurements in auroral arcs have also detected intense, variable fluxes of low energy electrons [*Boehm, et al.*, 1990], apparently accelerated by large amplitude Alfvén waves as described by Goertz and Boswell [1979] and Temerin et al. [1986]. In each case, the currents are accompanied by a substantial suprathermal electron population capable of driving ion acoustic

waves through nonlinear Langmuir wave coupling.

7.3 Discussion of Results

The methods elucidated in RR have been employed recently to model ion acoustic wave power enhancements, but even the assumption of very large current densities ($\sim 1 - -10$ mamps/m^2) is inadequate to produce the magnitudes of the observed effects (~20 dB) [FOS88; RD91; COLL91] as will be shown in the next section.

7.3.1 Interpreting Observations with RR

Millstone Hill UHF Data

Figure 7-11 shows an observed spectrum enhanced by a factor of 5 (top, solid curve) and a theoretical spectrum modeled after RR which shows the same enhancement (bottom, solid curve). To model the observed spectrum it is necessary to construct a composite spectrum via the superposition of three separate spectra having assumed values of T_r of 1, 5, and 9, respectively [FOS88]. Varying T_r is not unreasonable since the data are integrated for 30 seconds and the enhancement process most probably evolves over this time period. In addition to the relatively high T_r values, the 25 km/sec drift velocity required to produce the enhancement is essentially equivalent to the instability threshold critical velocity and corresponds to a 400 $\mu amp/m^2$ current.

EISCAT UHF data

In Figure 7-12 RD91 provide the results of the RR model output of ion line spectra for several different bulk electron parallel drift velocities for the observed value of $T_r = 3$. Qualitatively, the asymmetric model spectra look similar to observed UHF radar backscatter enhancements: but, even for an assumed drift of 100 km/sec (current

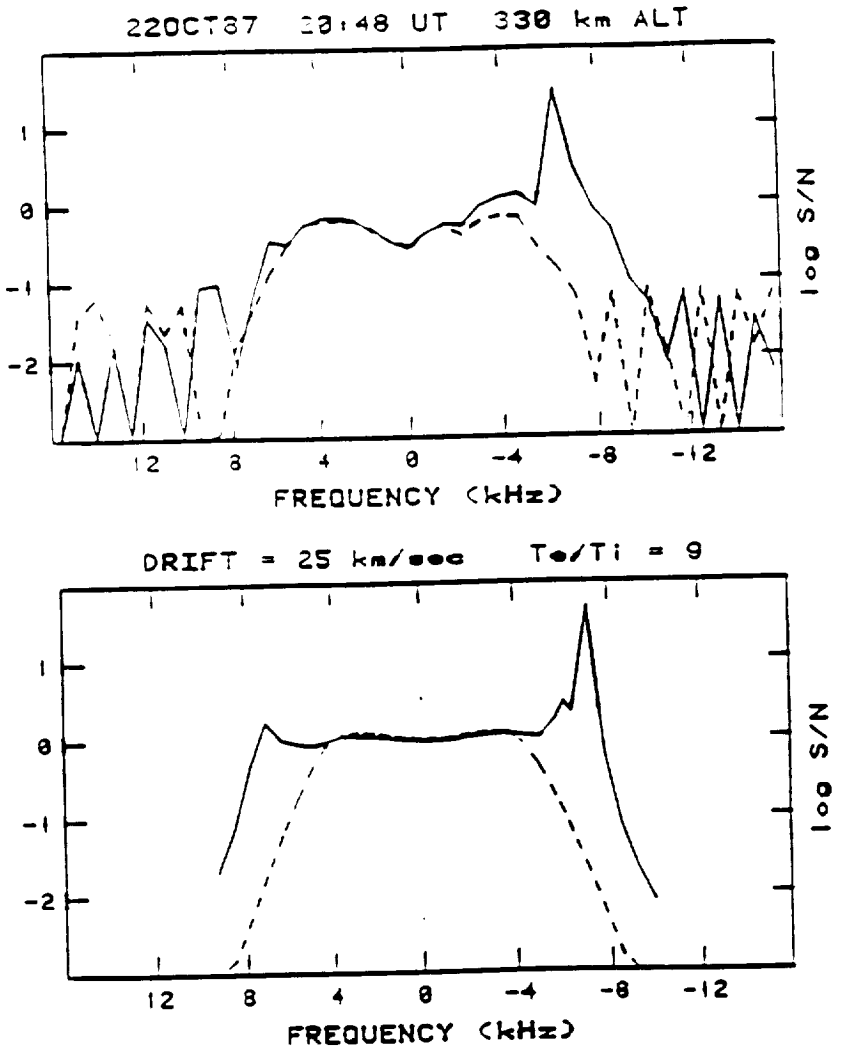

Figure 7-11: a) 7 dB acoustic enhancement observed with Millstone Hill UHF radar (solid line). b) Simulation of enhancement using RR model, assuming $T_r = 1$, 5, and 9 in ratios of 6:2:1, respectively, during a 30 second integration period [after FOS88].

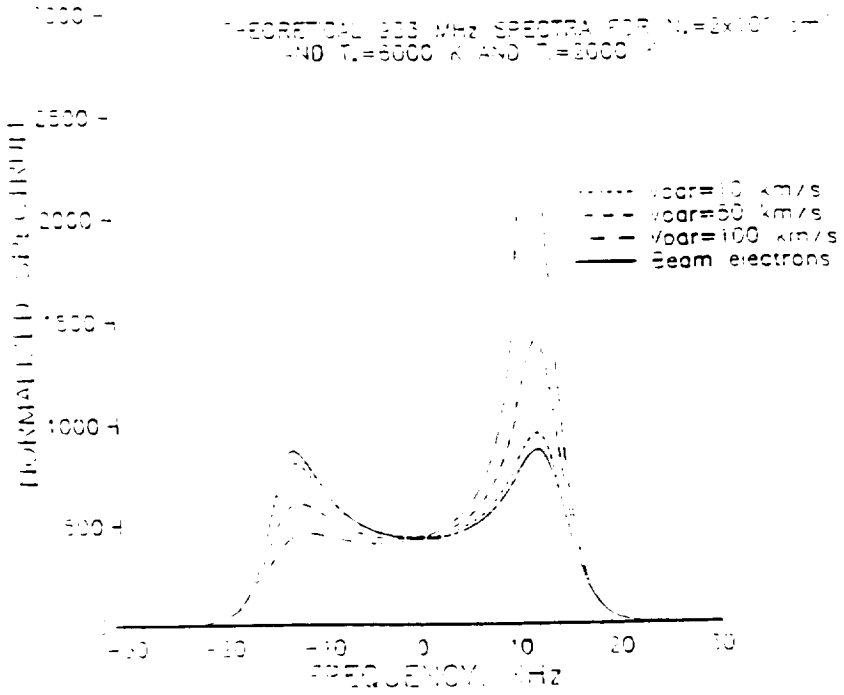

Figure 7-12: Theoretical ion line spectra for selected electron drift velocities for the EISCAT UHF radar. Although the asymmetry increases rapidly, the maximum enhancement in total cross section is only 25% [after RD91].

$\simeq 3$ $mamps/m^2$) equal to the critical velocity, the total cross section is enhanced by only 25%, less than 1 dB. By comparison, the observed cross sections were up to two orders of magnitude greater than normal incoherent scatter returns.

EISCAT VHF data

Figure 7-13 contains a pair of spectra observed with the 224 MHz radar and the corresponding theoretical fits (solid line) obtained by applying the RR model [COLL91]. The correlation between the two is quite good, giving reasonable estimates of the density and temperature ($T_r \simeq 3$) of the ionospheric plasma for the 6–7 dB enhancements. The model electron drift velocity required to achieve these results, however, was barely subthreshold implying a huge current density of a few milliamps per square meter. Furthermore, the fitting program failed entirely when applied to the larger, $\sim$ 15 dB enhancements reported in COLL91; instabilities of the type discussed by

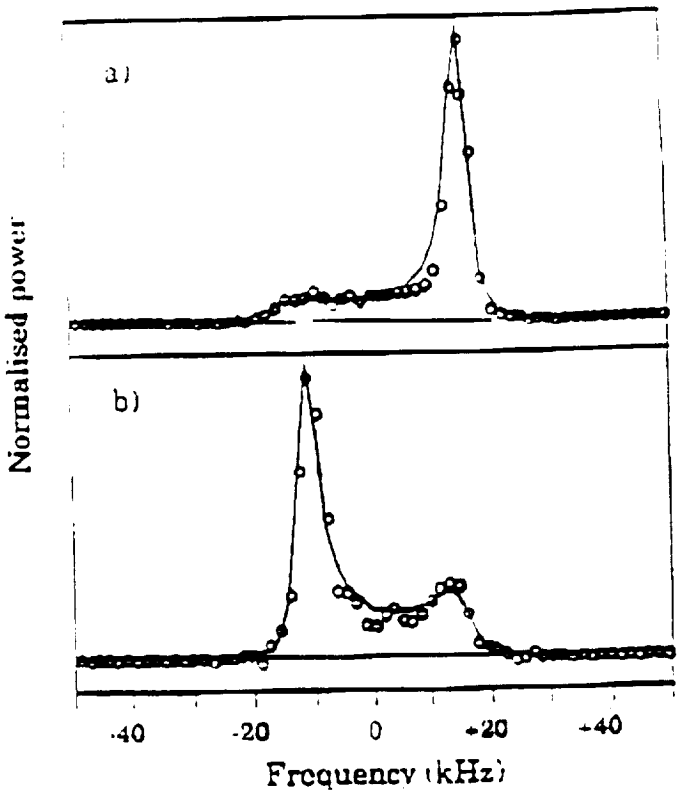

Figure 7-13: 6-7 dB Enhanced spectra observed with the EISCAT VHF radar and the corresponding theoretical fit applying the RR analysis (solid line). The fitting program failed to reproduce spectra exhibiting larger enhancements.

KK were assumed to be responsible for those.

Summary of RR Interpretation

The theory of RR applied to the observed enhancements of ion acoustic waves in the ionosphere produces mixed results. It correctly identifies the important role of soft (near thermal) electrons in the enhancement process, as confirmed by associated red airglow emissions, and the decreasing of the threshold drift velocity for increasing wavelength [COLL91]. The threshold velocity predicted by RR also decreases for elevated electron temperatures and temperature ratios, consistent with measurements reported by RD91 and COLL91, and the association drawn by FOS88 with topside density depletions in the ionospheric trough. However, the RR mechanism appears incapable of explaining other features of the observed data.

The most obvious feature is the magnitude of the enhanced radar backscatter

cross section. Pushing the theory to the limit of validity by assuming nearly critical electron drift velocities produces cross section enhancements of at most 10 dB; several observed enhancements approach 20 dB. Moreover, the large drift velocities required, attributed to bulk electrons, translate into current densities which are huge by ionospheric standards, $\sim$ 1-10 $mamps/m^2$. Currents of this intensity are 1–2 orders of magnitude greater than those that have been reported from in situ satellite measurements [*Bythrow et al.*, 1984; *J. D. Winningham*, private communication, 1988].

Qualitatively, the RR model describes the aesthetic features of some of the data, but important differences arise even at this level of application. Specifically, the theory predicts that an enhancement of one side of the spectrum be accompanied by a reduction in the other side. This is inevitable because of the underlying physics as explained in Section 7.1.1. More commonly the observations are characterized by an enhancement, albeit asymmetric, in both peaks of the spectrum. A possible explanation for this has been offered by RD91; namely, that the enhanced peaks are separated temporally on time scales not resolved by the 10 second integration period, or that opposing currents are flowing adjacent to one another on small spatial scales which cannot be resolved by the radar beam, some four kilometers in diameter at 400 km altitude.

These arguments may apply to some of the data. However, the persistence of some of the observed enhancements, particularly those detected with the EISCAT VHF radar (4 min. duration), and the large velocity gradients inherently implied by the small spatial scales suggested, raises doubts about the widespread adoption of these explanations for the large number of spectra exhibiting both upshifted and downshifted peak enhancements (nearly 40% of the more than 500 topside geophysical UHF ERB events found at EISCAT to date). An additional argument for simulta-

neous enhancements may be based on the distribution of the types of enhancements observed.

In Figure 7-14 the total number of ion acoustic ERB events recorded at EISCAT to date are categorized as being either upshifted, downshifted or symmetric enhancements and binned according to altitude. At higher altitudes, the distribution is dominated by symmetric enhancements. If this were due simply to inadequate measurement resolution in space or time (that is, the symmetric enhancements are simply superpositions of asymmetric enhancements of opposite peaks), one would also expect the number of downshifted and upshifted enhancements, relative to each other, to be roughly equal. Surprisingly, however, there are nearly twice as many downshifted peaks as upshifted at these altitudes, suggesting that the radar is not randomly smearing out the effects of a phenomenon which fluctuates between upshifts and downshifts on small spatial–temporal scales. One must either explain the proper mix of upshifted and downshifted enhancements at high altitudes in geophysical terms, or accept that the symmetric enhancements can be simultaneously stimulated and represent a limitation of the RR theory.

The application of the RR theory with regard to the detection of enhanced ion lines by a radar pointed at large aspect angle relative to the direction of the electron drift velocity produces mixed results. Enhancements occur only when the electron drift direction is perpendicular to the plane of reflection of the radar waves (see Figure 7-1). For backscatter geometry, this implies the drift must be parallel (or antiparallel) to the radar beam to observe enhancements. Backscatter observations of large enhancements extended along the magnetic field lines obtained with the radar pointed up the field lines are consistent with this interpretation. For remote sites diagnosing the same volume at large aspect angles, however, the field-aligned drift direction does not satisfy the geometry in Figure 7-1 with respect to the scattered waves and much weaker

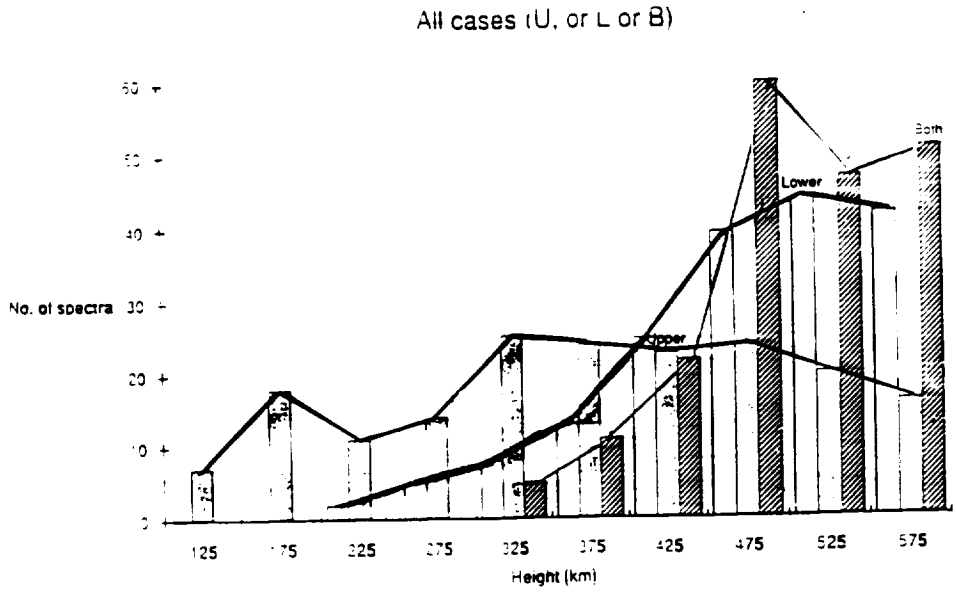

Figure 7-14: Histogram showing relative numbers of upshifted, downshifted and symmetric enhancements of the ion line recorded by the EISCAT UHF radar [after *M. Rietveld*, private communication, 1991].

enhancements would result. Thus, the theory seems consistent with the absence of EISCAT UHF remote site observations noted previously.

However, most of the ERB observations at Millstone Hill, Sondrestrom and several from EISCAT have been acquired at aspect angles of 20° or more with respect to the magnetic field. The well established zenith observations at all three sites also represent measurements at significant non-zero aspect angles. An interpretation of these observations with the RR mechanism would suggest that the assumed electron drifts are not always highly field-aligned. Some satellite measurements of intense currents have shown that the current-carrying electron fluxes were field-aligned by factors of about four to one [*J. D. Winningham*, private communication, 1988], which would not produce enhanced spectra at aspect angles greater than about 20° based on the RR mechanism. It is difficult to calculate the maximum aspect angle at which enhanced scattering can be detected because the exact nature of the currents inducing the enhancements is not well known. The conclusion that can be stated is that electron currents flowing obliquely at angles of up to 30° to the magnetic field are required by RR theory to explain the observations of ERB at large aspect angles.

7.3.2 Interpretations Based on KK Theory

The processes investigated by KK are valid in the drift velocity regime where RR's mechanism is no longer applicable. Their theory provides quantitative guidelines to which ion wave modes are least stable for given ionospheric conditions, and the growth rates of the various wave modes once the critical instability velocity is exceeded. Despite widespread recognition of its importance, detailed application of this theory to existing data has been limited for a couple of reasons.

One reason stems from the fact that the observations consist of enhancements of ion acoustic waves in the ionosphere. KK's work indicates that ion cyclotron wave

modes are destabilized at significantly lower drift velocity thresholds than acoustic waves, except for T_e values greater than about 20 in O^+ plasmas. Having no previous evidence that such large temperature ratios exist in the ionosphere, one must either accept this interpretation as first proof, or consider alternative explanations for the growth of the ion acoustic waves.

One such alternative is that the cyclotron waves do become unstable first, but the electric fields inducing the electron velocity drifts accelerate them beyond the acoustic wave threshold anyway. The cyclotron modes are strongly field-aligned and would probably be undetected by radar waves propagating at small aspect angles relative to the magnetic field, as is the case for the experiments considered here. That still leaves the problem of invoking an acceleration mechanism sufficiently robust to withstand unknown levels of energy loss due to the excitation of cyclotron waves, and proceed to destabilize ion acoustic waves. Sorting out such issues is nontrivial and requires significant additional theoretical investigation.

Another reason for lack of utilization of KK's results is simply the difficulty of comparing the theory's predictions with existing observations of enhanced spectra. The theory predicts which modes will be excited and at what rate, but it doesn't prescribe what the spectral shape will be and how large the waves will grow before saturating, characteristics generally determined by complicated nonlinear processes not treated by KK.

7.3.3 Implications of Nonlinear Langmuir Wave Coupling

As can be seen in Figure 7-10, the nonlinear wave coupling mechanism predicts significant enhancements in the cross section of ion acoustic modes observed by UHF radars. Furthermore, the enhancements are larger for longer wavelengths (smaller k), in agreement with the observations of COLL91 at VHF frequencies. These results are

also provided by the theories of KK and RR, though for different reasons.

A unique aspect of the wave coupling process is its prediction of enhancements for both upshifted and downshifted spectral peaks simultaneously. This can occur because the coupling mechanism excites the ion acoustic waves via the low frequency ponderomotive force due to the beating of intense Langmuir waves. Even though the Langmuir wave spectrum consists of waves moving primarily in the direction of the suprathermal electron flux responsible for their excitation, the various beating combinations of the waves can nonlinearly couple energy into a broad spectrum of ion waves. The symmetrically enhanced spectra are commonly observed (see Chapter 6), and previous explanations for their occurrence have been unsatisfactory.

With regard to the observations of ERB at large aspect angle relative to the magnetic field, the nonlinear coupling theory predicts enhancements of the ion acoustic waves over a broad spectrum of wave vectors. The result is that, even for the field-aligned distribution function assumed in the calculation of enhanced modes, ion acoustic waves are enhanced up to 10 dB at propagation angles up to 45° across the field-aligned direction (see Figure 7-10). Not surprisingly, the enhancement levels decrease as the aspect angle increases, though they are still significant. Thus, the nonlinear coupling theory provides an explanation for the observations of ERB at significant aspect angles.

A notable feature of the wave coupling mechanism is that the underlying physics are completely different from previous theories. In RR and KK, the wave modes grow because of a shift in the thermal electron distribution function; when the shift exceeds the phase velocity of ion wave modes, the *ion* waves grow at the expense of the electron kinetic energy in a wave–plasma interaction. In the nonlinear coupling process, on the other hand, streaming electrons stimulate *electron* waves initially. The energy is then transferred to ion wave modes via the nonlinear beating of the high frequency plasma

waves in a wave–wave interaction. The difference in the mechanisms is important to understand because both types of interactions may occur simultaneously, each contributing to the overall enhancement of ion acoustic waves in the ionosphere.

A Note on Distribution Functions

The intensity of the predicted enhancements of ion modes via nonlinear coupling is sensitive to the electron distribution function assumed in the calculation. In particular, the choice of the suprathermal component, f_p, affects the results significantly. In the calculation presented here and illustrated in Figures 7-9 and 7-10, actual satellite data was utilized in constructing the electron distribution function down to energies of 5 eV, about 20 times greater than the electron thermal energy. Nevertheless, the resulting f_p is based on a composite of three measurements and does not represent an "ensemble average" for auroral events; rather, it represents a *possible* distribution function for the ionosphere which may not be typical, but is by no means extraordinary, either.

A different f_p would produce a different enhancement spectrum than the one shown here. For example, if the low energy electron component ($\leq$ 50 eV) is omitted, a substantial reduction in the enhancement of short wavelength ion modes results. These modes are the very ones detected by UHF radars, indicating the importance of the the low energy particle population. Altering either the slope or the magnitude of f_p at any energy can cause significant changes in the final enhancement spectrum. Nevertheless, the general features of the enhancements shown here are preserved provided the assumed distribution function is characterized at low energies by a modest slope which steepens gradually with increasing electron energy and intersects the thermal electron population at about $5V_{th}$.

An intriguing possibility involves inverting the calculation to infer electron distribution functions from an observed ion line spectrum. Besides posing nontrivial math-

ematical obstacles, an attempt to perform this procedure faces an issue of uniqueness, since more than one distribution function can produce essentially identical enhancements. However, it may be possible with reasonable apriori assumptions and additional investigation to infer information about the suprathermal electron distribution function from enhanced incoherent scatter spectra.

7.4 Summary of ERB at Ion Acoustic Frequencies

Suprathermal electrons associated with field-aligned currents can excite a broad spectrum of Langmuir waves within the space plasma. Significant enhancement of ion acoustic waves through nonlinear Langmuir wave coupling is apparently possible when the local electron distribution function has a substantial nonthermal component, as in the presence of intense field-aligned currents. This mechanism may play an important role, acting in conjunction with other current driven processes, such as RR and KK, in amplifying the radar cross section of ion modes. It predicts important observed effects such as the simultaneous enhancement of upshifted and downshifted spectral peaks, increasing levels of enhancement for increasing wavelengths, and the enhancement of modes at large aspect angles. The RR mechanism explains only asymmetric enhancements. The most commonly observed ERB spectra exhibit enhancements of both peaks with moderate levels of asymmetry. These spectra may represent a superposition of effects described by the nonlinear coupling and RR theories, respectively, since they are based on different physical processes and can contribute to ERB independently. Calculations of current density which omit the contribution of the nonlinear wave coupling mechanism may seriously overestimate the intensity of the field-aligned currents associated with the observed ion line enhancements.

Bibliography

[1] Abreu, V. J., and H. C. Carlson, Photoelectron energy loss and spectral features deduced by the plasma line technique, *J. Geophys. Res.*, *82*, 1017–1023, 1977.

[2] Appleton, E. V., and M. A. F. Barnett, Local reflection of wireless waves from the upper atmosphere, *Nature*, *115*, 333-334, 1925.

[3] Bell, T. F., H. G. James, U. S. Inan, and J. P. Katsufrakis, The Apparent spectral broadening of VLF transmitter signals during transionospheric propagation, *J. Geophys Res.*, *88*, 4813–4840, 1983.

[4] Boehm, M. H., C. W. Carlson, J. P. McFadden, J. H. Clemmons, and F. S. Mozer, High–resolution sounding rocket observations of large–amplitude Alfvén waves, *J. Geophys. Res.*, *95*, 12157–12171, 1990.

[5] Breit, G., and M. A. Tuve, A radio method of estimating the height of the conducting layer, *Nature*, *116*, 357, 1925.

[6] Buonsanto, M. J., J. C. Foster, A. D. Galasso, D. P. Sipler, and J. M. Holt, Neutral winds and thermosphere/ionosphere coupling and energetics during the geomagnetic disturbances of March 6–10, 1989, *J. Geophys Res.*, *95*, 21033–21050, 1990.

[7] Bythrow, P. F., T. A. Potemra, W. B. Hanson, L. J. Zanetti, C.-I. Meng, R. Huffman, F. Rich, and D. Hardy, Earthward directed high-density Birkeland currents observed by HILAT, *J. Geophys. Res.*, *39*, 9114–9118, 1984.

[8] Chen, F., *Introduction to Plasma Physics and Controlled Fusion*, Plenum Press, 309–315, 1984.

[9] Cicerone, R. J., and S. A. Bowhill, Photoelectron fluxes measured at Millstone Hill, *Radio Sci.*, *6*, 957-966, 1971.

[10] Collis, P. N., L. Häggström, K. Kaila, and M. T. Rietveld, EISCAT radar observations of enhanced incoherent scatter spectra; their relation to red aurora and field-aligned currents, *Geophys. Res. Lett.*, *18*, 1031–1034, 1991.

[11] Dougherty, J. P., and D. T. Farley, A theory of incoherent scattering of radio waves by a plasma, *Proc. Roy. Soc. (London), A259*, 79–99, 1960.

[12] Ergun, Robert E., Linear and nonlinear wave processes in the auroral ionosphere, U. C. Berkeley, Ph. D. Dissertation, 1989.

[13] Evans, J. V., Theory and practice of ionosphere study by Thomson scatter radar, *Proceedings of the IEEE*, *57*, 496–530, 1969.

[14] Farley, D. T., A plasma instability resulting in field-aligned irregularities in the ionosphere, *J. Geophys. Res.*, *68*, 6083–6097, 1963.

[15] Fejer, J., Scattering of radiowaves by an ionized gas in thermal equilibrium, *Can. J. Phys.*, *38*, 1114–1133, 1960.

[16] Foster, J. C., C. del Pozo, K. Groves, and J.-P. St. Maurice, Radar observations of the onset of current driven instabilities in the topside ionosphere, *Geophys. Res. Lett.*, *15*, 160–163, 1988.

[17] Foster, J. C., J. R. Burrows, and P. M. Banks, High latitude ionospheric troughs associated with inward directed Birkeland currents, *EOS*, *57*, 1976.

[18] Goertz, C. F., and R. W. Boswell, Magnetosphere–ionosphere coupling, *J. Geophys. Res.*, *82*, 2235, 1977.

[19] Groves, K. M., M. C. Lee, and S. P. Kuo, Spectral broadening of VLF radio signals traversing the ionosphere, *J. Geophys. Res.*, *93*, 14683–14687, 1988.

[20] Gurnett, D. A., and L. A. Frank, VLF Hiss and Related Plasma Observations in the Polar Magnetosphere, *J. Geophys. Res.*, *77*, 172, 1972.

[21] Hagfors, T., Density fluctuations in a plasma in a magnetic field, with applications to the ionosphere, *J. Geophys. Res.*, *66*, 1699–1712, 1961.

[22] Helliwell, Robert A., *Whistlers and Related Ionospheric Phenomena*, Stanford University Press, 121-123, 1965.

[23] Inan, U. S., and T. F. Bell, Spectral broadening of VLF transmitter signals observed on DE 1: A quasi-electrostatic phenomenon?, *J. Geophys. Res.*, *90*, 1771–1775, 1985.

[24] Inan, U. S., T. F. Bell, and H. C. Chang, Particle precipitation induced by short-duration VLF waves in the magnetosphere, *J. Geophys. Res.*, *87*, 6243–6264, 1982.

[25] Johnson, N. L., History and consequences of on-orbit breakups, *Adv. Space Res.*, *5*, 11–19, 1985.

[26] Kessler, D. J., Orbital debris issues, *Adv. Space Res.*, *5*, 3–10, 1985.

[27] Kindel, J. M., and C. F. Kennel, Topside current instabilities, *J. Geophys. Res.*, *76*, 3055–3078, 1971.

[28] Koons, H. C., B. C. Edgar, and A. L. Vampola. Precipitation of inner zone electrons by whistler mode waves from VLF transmitters UMS and NWC, *J. Geophys. Res.*, *86*, 640–648, 1981.

[29] Kuo, S. P., and M. C. Lee. Stimulated scattering instability of lower hybrid waves. *Phys. Fluids*, *29*, 1024, 1986

[30] Lamb, George L., The scattering of electromagnetic waves by nonequilibrium plasmas. *Los Alamos Scientific Laboratory Internal Report*, LA–2715, 1962.

[31] Laaspere, T., W. C. Johnson, and L. C. Semprebon, Observations of auroral hiss, LHR noise and other phenomena in the frequency range 20 Hz–540 KHz on OGO 6, *J. Geophys. Res.*, *76*, 4477, 1971.

[32] Lee, M. C., Ion line enhancement in ionospheric heating experiments. *J. Phys. D: Appl. Phys.*, *14*, 851–860, 1981.

[33] Lee, M. C., and S. P. Kuo, Production of lower hybrid waves and field-aligned density striations by whistlers, *J. Geophys. Res.*, *89*, 10873–10880, 1984.

[34] Marshall, J. A., J. L. Burch, J. R. Kan, P. H. Reiff, and J. A. Slavin, Sources of field–aligned currents in the auroral plasma. *Geophys. Res. Lett.*, *18*, 45–48, 1991.

[35] Mayaud, P. N., *Derivation, Meaning and Use of Geomagnetic Indices*, AGU Geophysical Monograph 22, 1980.

[36] McEwen, D. J., and R. E. Barrington. Some characteristics of the lower hybrid resonance noise bands observed by the Alouette I satellite, *Can. J. Phys.*, *45*, 13, 1967.

[37] McFadden, J. P., C. W. Carlson, and M. H. Boehm, High–frequency waves generated by auroral electrons, *J. Geophys. Res.*, *91*, 12079–12088, 1986.

[38] Perkins, Francis, and E. E. Salpeter, Enhancement of plasma density fluctuations by nonthermal electrons, *Phys. Rev.*, *139*, A55–A62, 1965.

[39] Pines, David and David Bohm, A collective description of electron interactions: II. Collective vs individual particle aspects of the interaction, *Phys. Rev.*, *85*, 338–353, 1952.

[40] Providakes, J., D. T. Farley, W. E. Swartz, and D. Riggin, Plasma irregularities associated with a morning discrete auroral arc: Radar interferometer observations and theory, *J. Geophys. Res.*, *90*, 7513–7523, 1985.

[41] Rietveld, M. T., P. N. Collis, and J.–P. St. Maurice, Naturally enhanced ion acoustic waves in the auroral ionosphere observed with the EISCAT 933–MHz radar, *J. Geophys. Res.*, *in press*, 1991.

[42] Rishbeth, H., Basic physics of the ionosphere: A tutorial review, *J. IERE*, *58*, S207–S223, 1989.

[43] Rosenbluth, M. N., and N. Rostoker, Scattering of electromagnetic waves by a non-equilibrium plasma, *Phys. Fluids*, *5*, 776–788, 1962.

[44] Salpeter, E. E., Electron density fluctuations in a plasma, *Phys. Rev*, *120*, 1528–1535, 1960.

[45] Salpeter, E. E., Plasma density fluctuations in a magnetic field, *Phys. Rev*, *122*, 1663–1674, 1961.

[46] Schlegel, K., and D. R. Moorcroft, Unusual *F*-region echoes observed with EISCAT, *Max-Planck-Institut für Aeronomie internal report*, MPAE-W-05-89-13, 1989.

[47] *ACTIVE space plasma–wave laboratory* Acad. of Sci. of the USSR, Space Research Institute Report, 1987.

[48] Storey, L. R. O., An investigation of whistling atmospherics. *Phil. Trans. Roy. Soc. (London), A246*, 113-141, 1953.

[49] Swanson, D. G., *Plasma Waves*, Academic Press, 1989.

[50] Sudan, R. N., J. Akinrimisi, and D. T. Farley, Generation of small scale irregularities in the equatorial electrojet, *J. Geophys. Res.*, *78*, 240, 1973.

[51] Temerin, M., J. McFadden, M. Boehm, C. W. Carlson, and W. Lotko, Production of flickering aurora and field-aligned electron flux by electromagnetic ion cyclotron waves, *J. Geophys. Res.*, *91*, 5769, 1986.

[52] Thomson, J. J., *Conduction of Electricity Through Gases*, Cambridge University Press, London, 1906.

[53] Ungstrup, E., W. J. Heikkila, J. C. Foster, and W. O. Lennartsson, Compositional changes, time and density variations in the magnetosphere associated with Birkeland currents and particle acceleration, *Adv. Space Res.*, *6*, 113-116, 1986.

[54] Wahlund, J.-E., H. J. Opgenoorth, L. Häggström, K. J. Winser, and G. O. L. Jones, EISCAT observations of topside ionospheric ion outflows during auroral activity: Revisited, *J. Geophys. Res.*, *in press*, 1991.

[55] Yngvesson, K. O., and F. W. Perkins, Radar Thomson scatter studies of photoelectrons in the ionosphere and Landau damping, *J. Geophys. Res.*, *73*, 97–109, 1968.